Novel Effects in Field Accretion around Black Holes



James Marsden

St Cross College

University of Oxford

A thesis submitted for the degree of

Doctor of Philosophy

Trinity 2025

DECLARATION

I declare that no part of this thesis has been accepted, or is currently being submitted for any degree or diploma or any other qualification in this University or elsewhere.

James Marsden July 14, 2025

Statement of Originality

The work presented in this thesis was conducted as a DPhil student at the University of Oxford. Chapters 2 and 3 are based on published works (Marsden et al., 2024; Aurrekoetxea et al., 2024c), for which I am the first author or joint first author. These papers were published in collaboration with Josu Aurrekoetxea, Katy Clough, and Pedro Ferreira. Chapter 4 is based on unpublished work in which I have derived the mathematics for the rank-2 field with contributions from Josu Aurrekoetxea, Katy Clough, and Pedro Ferreria, and ran the simulations found in said chapter. The simulations in this thesis were performed using the open source software GRChombo (Clough et al., 2015; Andrade et al., 2021) and GRDzhadzha (Aurrekoetxea et al., 2024b). I thank the GRChombo collaboration (www.grchombo.org) for their support and code development work. I acknowledge funding from STFC. Part of this work was performed using the DiRAC@Durham facility managed by the Institute for Computational Cosmology on behalf of the STFC DiRAC HPC Facility (www.dirac.ac.uk) under DiRAC RAC13 Grant ACTP238 and DiRAC RAC15 Grant ACTP316. The equipment was funded by BEIS capital funding via STFC capital grants ST/P002293/1, ST/R002371/1 and ST/S002502/1, Durham University and STFC operations. This work also used the DiRAC Data Intensive service at Leicester, operated by the University of Leicester IT Services, which forms part of the STFC DiRAC HPC Facility (www.dirac.ac.uk). The equipment was funded by BEIS capital funding via STFC capital grants ST/K000373/1 and ST/R002363/1 and STFC DiRAC Operations Grant ST/R001014/1. DiRAC is part of the National e-Infrastructure.

The copyright of this thesis rests with the author. The author asserts his moral rights.

Acknowledgements

There are so many people who have assisted me in immeasurable ways over the course of my DPhil, so if I have unintentionally left out your name, this was not deliberate but an effect of having received so much kind help from all of you.

To those who have assisted me academically in during my doctorate, I am infinitely grateful. I particularly want to thank Josu Aurrekoetxea first, who has acted basically as a third supervisor to me (with none of the salary). All of your physics knowledge, deep curiosity and relentless enthusiasm have made me the (slightly) more wise astrophysicist I am today. Without even a single element of your help, I would not have been able to complete this thesis, and would still probably be stuck on my tensor field project from my first month in Oxford. You also taught me the vital lesson of how to properly drink patxaran, and how to 'shotpile' when code stubbornly refuses to work.

To Katy Clough, my second supervisor, I give thanks for your technical wizardry with GRChombo and GRDzhadzha, and all of your vast knowledge on numerical relativity. You have been a source of calm and consistent support during many tough times and difficult projects, and have especially taught me that when a simulation fails or looks weird, it's probably because I have mistyped a mass in the parameters file. Perhaps one day we can work on a warp drive paper together!

Lastly I thank Pedro Ferreira, my first supervisor. I have enjoyed many thought provoking and insightful conversations with you, and cherish many good memories discussing physics problems (and cult classic films) in your sunny office. I have had the exceedingly good fortune to have you as a very wise and supportive mentor, and you have given me a great enthusiasm and appreciation for gravitational physics which I will certainly take with me wherever I end up going next, whether that be in academia or elsewhere. I particularly thank you for choosing me to be your student in the first place!

I also want to thank all of the astrophysics sub department in Oxford for being such a kind and welcoming place, in particular, Ashling Gordon, for being a beacon of enthusiasm and positivity in the building yet also a brutally efficient administrator whenever something serious needed to be done.

Thank you as well to all of my American friends in Baltimore whom I met during my long term attachment there. Special thanks to Emanuele Berti for

kindly hosting me, and to Nick Speeney, Thomas Helfer, Andrea Antonelli, and Zipeng Wang for helping me feel welcomed, and of course for all the misadventures. Thanks especially to Ritika Khinvasara and Manasa Krishnan with whom I spent so many lovely evenings.

Next, I want to give gratitude to my loving parents and wonderful brother, who have seen my entire journey in Astrophysics from starting with trips to the London Science Museum to see the rockets, and now submitting my thesis on black holes (not rockets however). Specifically, I thank my mum Krystyna for always waiting with a loving hug whenever things got tough, my dad Jon (Jonty), for his witty banter and the lively debates we have on everything from geopolitics to mathematics over the dining table, and my brother Mark, for being a relentless source of activity and energy of which I am continually impressed, and especially in his ability to fit international trips into the space of a weekend. I have finished my 'little dissertation'!

I want to thank all of my wonderful cohort with whom I have suffered collectively over the course of our DPhils. Matthew Hopkins, you have been a great support for me in tough times, as well as a fellow enjoyer of cryptic crosswords in equal measure. I thank you for teaching me, a barbarous southerner, about the superiority of being from 'up North'. To Phil Holloway, for sharing a late night office on many occasions as well as being a wonderful source of quiet wisdom. To Fergus Donnan, for the excitement given by producing controversial opinions on minor topics, as well as teaching me how to make a perfect Negroni. To Rohan Varadaraj, for making me laugh more than anyone else in the office, and for our combined efforts in shooting Fergus with foam darts. To David Simon, Haochuan Yu, and Hanxi Wang - although we didn't share an office for the final push, it has been a great pleasure to know you all.

A section of these must acknowledgements must be dedicated to the Oxford Institute of Peace and Prosperity (OIPP). To all of these esteemed and enlightened members I show my gratitude. To the infamous Casey Cragg, (大哥), you have been my comrade-in-arms. We have shared many pints, both in happiness and sorrow, and yet have pulled through every single time. May we find auspicious beverages wherever we go. 不求同年同月同日生，但愿同年同月同日死[1]. To Alex Andersson, (二哥) for unmatched flag knowledge, cider appreciation, and an incredibly tasteful selection of Instagram reels. You have the unique pleasure of being my ideal choice for both a pub quiz team, and last minute high stakes cribbage tournament partner. To Madalina Tudorache, who shares my deep love for all things feline, and possesses terrifyingly accurate knowledge of the location of every single cat in Oxford. You have always been there to support my woes, and you remember my own schedule

[1]Though we sought not to be born on the same day, in the same month, in the same year, we humbly wish to die on the same day, in the same month, in the same year. *Romance of the Three Kingdoms*, Luo Guanzhong c. 14th century AD

better than I do. To Jaime Ruiz Zapatero, for wisdom ranging from the Napoleonic wars and the history of metallurgy to Neon Genesis Evangelion, and also for being an excellent flatmate. To Eric Liang, for the enthusiasm to engage with my various questions on Chinese culture, and for willingness to engage in a spontaneous trip to the pub. To Curro Rodríguez Montero for giving me a deep appreciation of the beautiful land of Andalusia and being a kindred enjoyer of Taylor Swift. To other people in Astrophysics - Andreea Veresteanu, thank you for all the lovely coffees we've had for being a ray of sunshine in the truest sense.

I thank all of my friends from London as well. In particular, Quinne, River, Iga Zacharewicz, Alex Smola, Omar Abbas, Nick Clark, Ryan Brady, and Torin Oades. Thanks also to Maggie Chen for being a good friend during the uncertain early days of our first coming to Oxford.

Particular thanks to the Oxford University Gilbert and Sullivan Society, without whom, I would have finished my DPhil at least a year ago. *"When darkly looms the day, and all is dull and grey, to chase the gloom away, on thee I'll call!"*. Hannah Capstick and Joe Pollacco, thank you for listening to all my complaints when a show was looking particularly sketchy right before the first night. Sarah Davies, you possess the proud honour of being both a fantastic welfare officer and much-needed light-hearted antagonist to all of my nonsense. To Andrew Raynes, thank you for the lovely 4 am chats in your room (sorry). To Macks O'Byrne and Madeleine Lay, thank you for being perhaps the greatest pub quiz team I have known, and for letting me tag along while contributing no actual answers. Lastly, I give thanks to all of my other friends in Oxford to whom I owe so many wonderful memories. Srinandini Mukherjee and Moumili Dutta, thank you for introducing me to the wonderful and cheesy world of 90's Bollywood films and for always being so incredibly cheerful and friendly. Jessica Wei and Ran Tao, we have had so many fun times together, often involving karaoke. James Galvin, you are my strongest adversary at any boardgame and have been a fantastic friend for so many years. Particular thanks to my wonderful flatmates - Fabian Helmrich, Loren Kell, and Ziwen Wang. You have made our humble flat a place of comfort and friendship, and thank you for tolerating all of the times I loudly returned to the house at perhaps slightly too late of an hour.

Lastly, to anyone still reading these acknowledgements, I want to thank you for your commitment and will subsequently reward you with the presumed joy which will come from reading the rest of my thesis.

Abstract

Black holes are some of the most mysterious and fascinating objects in the Universe. Due to the environments of extreme spacetime curvature they produce, for a theoretical physicist, they can serve as useful laboratories where interesting phenomena associated with various physical fields and functions can be manifest and therefore studied. In this thesis, I am particularly concerned with the effects which appear during the accretion of various beyond-standard model fields onto black holes, and how these effects vary depending on the microphysics of the particle in question.

Firstly, I consider two distinct models of scalar field. The first model involves an additional quartic term to the potential of the particle, coupled with a parameter λ. I study the accretion of clouds of these particles onto isolated Schwarzschild black holes, and how different values of λ affects the behaviour and growth of these fields as they accrete. I then consider the effects that these fields have on the merger of binary black holes, both on the cloud itself, and on the merger dynamics itself.

The second category of scalar fields I investigate are multi-minima models, in order to study the phenomena of symmetry restoration and vacuum decay. These are effects reliant on the field beginning at an energy scale where it oscillates around a single one of the potential minima. I am focused on how black hole accretion can increase the energy of the field, and so catalyse a phase transition in the field, undergoing a change from one state to another as it begins to explore regions of the potential outside of its initial minimum.

In my final chapter, I introduce formalism for simulating massive rank-2 tensor fields in 3+1 numerical relativity. I start from the general action, and then split up the field into a series of constituent sub-fields. By defining a new tensor related to the first derivative of the field, I substitute this in to the wave equation and undergo a series of derivations to find a set of evolution equations for the aforementioned sub-fields and their associated conjugate momenta. I then demonstrate some example simulations one can perform with these equations, including the scattering of gravitational waves around a black hole, before detailing ideas for future work on this project.

Contents

1 Introduction **1**

1.1 General Relativity . . . 1

1.1.1 Prelude . . . 1

1.1.2 Differential Geometry . . . 3

1.1.3 Einstein's Equations . . . 5

1.1.4 Geodesics . . . 7

1.1.5 Classical Field Theory . . . 8

1.2 Spacetimes . . . 12

1.2.1 Static Black Holes . . . 13

1.2.2 Rotating Black Holes . . . 16

1.3 Dark Matter in the Universe . . . 17

1.3.1 Motivation . . . 17

1.3.2 The Nature of Dark Matter . . . 19

1.3.3 Wave-like Dark Matter . . . 20

1.3.4 Multi-Minima Potentials . . . 24

1.4 Numerical Relativity . . . 28

1.4.1 Prelude . . . 28

1.4.2 The Foliation of Spacetime - 3+1 Physics . . . 29

1.5 GRChombo and GRDzhadzha . . . 42

1.5.1 GRChombo . . . 42

1.5.2 Fixed-background Evolution . . . 43

2 Self-Interacting Scalar Dark Matter around Binary Black Holes **46**

2.1 Motivation . . . 46

2.2 Introduction . . . 47

2.3 Scalar field dark matter model . . . 51

2.4 Dark matter around an isolated black hole . . . 53

2.5 Dark matter around an equal mass black hole merger . . . 60

2.6 Discussion . . . 66

3 Symmetry Restoration and Vacuum Decay around Black Holes 69
3.1 Motivation . . . 69
3.2 Introduction . . . 70
3.3 Multi-minima wave-like dark matter models . . . 72
3.4 Results . . . 75
3.4.1 Symmetry restoration . . . 75
3.4.2 Vacuum decay . . . 79
3.5 Discussion . . . 82

4 Rank-2 Tensor Fields in Numerical Relativity 84
4.1 Introduction . . . 84
4.2 Rank 0 - Scalar Field . . . 85
4.3 Rank 1 - Proca Field . . . 87
4.4 Primary and Secondary Constraints . . . 90
4.5 Rank 2 - Tensor Field . . . 93
4.5.1 3+1 Equations of Motion for a Tensor Field . . . 93
4.5.2 Gravitational Wave Solutions and Scattering . . . 101
4.5.3 Tensor Fields on Taub Spacetime . . . 106
4.5.4 Future Work . . . 110

5 Conclusion 111

Appendices

A Numerical Relativity 116
A.1 The BSSN System . . . 116
A.2 The CCZ4 System . . . 118
A.3 Alternative Derivation For Proca - Laplace Operator Form . . . 121

B Error Analysis - Convergence Testing 125

Bibliography 129

AWAKE! for Morning in the Bowl of Night
Has flung the Stone that puts the Stars to Flight:
And Lo! the Hunter of the East has caught
The Sultan's Turret in a Noose of Light.

— Omar Khayyam

The Rubaiyat of Omar Khayyam
Translated by Edward FitzGerald

1 Introduction

1.1 General Relativity

1.1.1 Prelude

The past few centuries have seen incredible advances in our understanding of gravity and our ability to use it as a predictive tool for the behaviours of the universe. For much of the past, and indeed still in the present, Isaac Newton's theory of gravity dominates the forefront as a successful and yet simple theory. In the June of 1846, Urban Le Verrier proposed the existence of a perturbation in the form of a new planet to account for the as-of-yet unexplained discrepancies in the orbit of Uranus which could not be produced by any of the known bodies in the solar system at the time. Indeed, this prediction turned out to be correct, and in September of the same year, a team lead by Johann Gottfried Galle discovered this new planet following Le Verrier's revised calculations and found it to be within a degree of where he had predicted it to be. This was the first planet in the solar system to have its existence correctly predicted solely with the principles of gravity. In a fitting quote from fellow astronomer François Arago, Le Verrier had discovered Neptune "with the point of his pen". Indeed, in modern astrophysics, Newtonian models of gravity remain incredibly relevant, and have been used to make many important predictions in a variety of fields.

History showed however, that with the gathering of more precise data, Newton's gravity became discrepant with our observations. Perhaps the most famous problem encountered was in the precession of the perihelion of Mercury (Le Verrier, 1859). New, more precise data revealed that the closest point of Mercury's orbit to the Sun precessed at a rate inconsistent with all conceivable Newtonian mechanisms. In previous decades, there was no such problem, as the most accurate measurements and most complete datasets of the planet agreed with all contemporary theories. This issue regarding Mercury was first noticed by Le Verrier, and each attempt to reconcile this observation with Newtonian physics ultimately proved unsuccessful; this amongst other things was a catalyst which led to a re-evaluation as to how we understand gravity. The key breakthrough was famously made by Albert Einstein in a series of landmark papers, culminating in his development of his theory of general relativity (Einstein, 1916), whilst also solving the problem of Mercury's precession in the process (Einstein, 1915). Einstein's great idea was in connecting the mathematics of curved space and the notion of gravity, and has given us the current most-accurate known model of gravity we have.

In the 21st century, we are experiencing a similar revolution in the limits to which we can test our understanding of gravity. The advent of gravitational wave astronomy (Abbott et al., 2016) has given us a new window with which we can explore the universe, and a precisely measurable phenomenon coming as a direct consequence of Einstein's gravity. In a way, this is a 'new Mercury' by which we can scrutinise our understanding of general relativity. As of writing, the data we receive from gravitational wave measurements from the principal three gravitational wave detectors LIGO, Virgo, and KAGRA (Aasi et al., 2015; Acernese et al., 2015; Akutsu et al., 2021) are fully consistent with general relativity, but with the continual improvement of data, this is at liberty to change. As the next generation of gravitational wave detectors begin their operations, we will be able to test fine-detail phenomena such as black hole ringdowns (Berti, Cardoso, and Will, 2006) and cosmological phase transitions (Caprini et al., 2020), as well as a host of other observables using future space-based gravitational wave detectors

such as probing inflation (Bartolo et al., 2016) and detecting extreme mass-ratio in-spirals (Babak et al., 2017). With these detectors, the limits of our theories can continue to be pushed.

1.1.2 Differential Geometry

Differential geometry is the foundation of general relativity, and so I will first cover its essential components in order to understand Einstein's theory and the work later in this thesis. I begin with a brief aside on the Einstein summation convention. This states that any dummy index - one which is repeated on the same side of an equation - is implicitly summed over all of its range, which is useful for saving space. For example, a total derivative can be written compactly as:

$$\mathrm{d}x'^{a} = \frac{\mathrm{d}x'^{a}}{\mathrm{d}x^{b}}\mathrm{d}x^{b} \tag{1.1}$$

With this notation we can define tensors[1]. These are objects consisting of a set of values at a given event in spacetime that obey the following transformation law.

$$X'^{a}{}_{b} = \frac{\partial x'^{a}}{\partial x^{c}}\frac{\partial x^{d}}{\partial x'^{b}}X^{c}{}_{d} \tag{1.2}$$

This ensures that if a tensorial equation holds in one set of coordinates, it holds in all sets of coordinates. Hence, by describing physical laws using tensors, we can ensure they hold universally. A particularly important example of a tensor is the metric tensor. Metrics are used to measure distances upon manifolds and so can calculate the spacetime interval between two events

$$\mathrm{d}s^{2} = g_{ab}\mathrm{d}x^{a}\mathrm{d}x^{b}. \tag{1.3}$$

The sign of this interval indicates the type of separation between events. This is dependent on sign convention - in this thesis I use the (-,+,+,+) convention. $\mathrm{d}s^2 > 0$ indicates a greater spatial separation than temporal, and so the interval is spacelike. The inverse is true for $\mathrm{d}s^2 < 0$, which we call a timelike interval, and $\mathrm{d}s^2 = 0$ implies a null, or lightlike interval. Null intervals are used to describe the

[1] A frustratingly accurate definition repeated to many undergraduates learning general relativity for the first time, once including myself, is that *"tensors are objects which transform like tensors"*.

boundaries of causality. Two events which are on either side of a null world-line are causally disconnected and so no communication between them is possible.

We now want to define a set of operations that have the same transformation properties of tensors. Partial derivatives when applied to a tensor are not tensorial, and so we define the covariant derivative, denoted by the symbol ∇ which results in a tensor quantity when applied to a tensor

$$\nabla_c X^a{}_b = \partial_c X^a{}_b + \Gamma^a{}_{dc} X^d{}_b - \Gamma^d{}_{bc} X^a{}_d. \tag{1.4}$$

$\Gamma^a{}_{bc}$ is the Christoffel symbol and is an object symmetric in its lower indices. For tensors with arbitrary numbers of indices, the above pattern repeats with the sign of the Christoffel symbol term changing depending on whether it was an upper or lower index. The Christoffel symbol is defined as

$$\Gamma^i{}_{jk} = \frac{1}{2} g^{il} \left(\partial_j g_{lk} + \partial_k g_{jl} - \partial_l g_{jk} \right). \tag{1.5}$$

Another useful operation is the Lie derivative. It is defined as

$$\mathcal{L}_Y X^a{}_b = Y^c \partial_c X^a{}_b + X^a{}_c \partial_b Y^c - X^c{}_b \partial_c Y^a. \tag{1.6}$$

This describes the rate of change of $X^a{}_b$ along the flow of a vector field Y^a.

Using the framework of Lie derivatives, we can also define an important example of a vector field when examining specific spacetimes. A Killing vector field satisfies

$$\mathcal{L}_X g_{ab} = 0, \tag{1.7}$$

such that Killing vectors possess symmetries along their flow - i.e. the metric is preserved when 'dragged' along a Killing vector field.

The last key geometric object we need to understand is the Riemann curvature tensor. In terms of Christoffel symbols, it can be defined as:

$$R^a{}_{bcd} = \partial_c \Gamma^a{}_{bd} - \partial_d \Gamma^a{}_{bc} + \Gamma^a{}_{ce} \Gamma^e{}_{bd} - \Gamma^a{}_{de} \Gamma^e{}_{bc} \tag{1.8}$$

There are many different interpretations of the Riemann tensor, but one of them is that it measures the amount of deviation between a vector at a point, and the

same vector when parallel transported in a loop along a closed path back to the start. It measures the non-commutability of second-order covariant derivatives when applied to a vector field:

$$R^{a}{}_{bcd}X^{b} = \nabla_{c}\nabla_{d}X^{a} - \nabla_{d}\nabla_{c}X^{a}. \tag{1.9}$$

With either of the definitions presented, the Riemann tensor vanishes when in flat space, as a vector when parallel transported around a closed loop in flat space experiences no change in direction, and in flat space, covariant derivatives become partial derivatives. The Riemann tensor has some associated contractions which are the Ricci tensor and Ricci scalar which are defined as

$$R_{ab} = R^{c}{}_{acb} \tag{1.10}$$

and

$$R = R^{a}{}_{a}. \tag{1.11}$$

The Ricci tensor in particular has the interesting property that it vanishes in a vacuum, i.e. when no matter is present. Due to it being a contraction of the Riemann curvature tensor, a vanishing Ricci tensor does not necessarily imply a vanishing Riemann tensor. Therefore, this property can be used to define a class of vacuum spacetimes with non-zero curvature, for example, black holes, which I will discuss later.

1.1.3 Einstein's Equations

Perhaps the simplest summary of the Einstein field equations is captured in a quote from John Wheeler: *"Matter tells spacetime how to curve, and curved spacetime tells matter how to move"*. The left hand side of the field equations is often referred to as the curvature part, and the right hand side as the matter part. The curvature part is composed of the Einstein tensor

$$G_{ab} = R_{ab} - \frac{1}{2}g_{ab}R, \tag{1.12}$$

and the matter half of the field equations is composed of the stress-energy tensor or energy-momentum tensor T_{ab} whose form varies depending on the specific matter considered - see Section 1.1.5. The principle of minimal gravitational coupling, and the vanishing of the Einstein tensor via the contracted Bianchi identities suggest that these two tensors are proportional to one another; this produces the Einstein field equations:

$$G_{ab} = 8\pi T_{ab} \tag{1.13}$$

In this thesis, I use the geometric units convention unless otherwise specified This means we choose the speed of light c, and the gravitational constant G to both equal one, i.e. $c = G = 1$. Importantly, this makes the dimensions of mass, length, and time all have the same unit. This has the consequence of introducing an overall mass scale to any scenario that we consider. When running simulations, this is useful as all the results are freely scalable by the mass of the black hole.

Equation (1.13) is essentially an equation of motion for the components of the metric. The Einstein tensor contains the Ricci tensor which in turn contains second derivatives of the metric tensor. We also find first derivatives of the metric and products of derivatives, making this a non-linear wave equation. We can also frame this in terms of the Cauchy problem. This can be cast as an initial value problem, which tasks us with finding the solution to a set of partial differential equations given the initial values and derivatives of the field at each point on the manifold. In this particular case, we are considering the metric tensor as our field. We can find the second time derivative of the metric from the field equations and then integrate this to find the first time derivatives and values of the field at all later times. Critically, the solution to the Cauchy problem is unique (Choquet-Bruhat, Chrusciel, and Martin-Garcia, 2011), meaning that a unique set of initial values and derivatives will produce a unique solution, which is part of the demands for a classical theory of gravity.

An interesting thing to consider next is the number of degrees of freedom present in Einstein's equations. We start by looking at the left hand side of Equation (1.13).

G_{ab} is a 4×4 symmetric tensor, meaning that it has 10 components or degrees of freedom. This does not take into account the gauge choices and constraints however. Consider taking the covariant derivative of the Einstein tensor:

$$\nabla^b G_{ab} = 0 \tag{1.14}$$

Equation (1.14) is known as the twice-contracted Bianchi identity. By expanding the terms, we find that this contains no second time derivatives of the metric tensor. This is therefore not an evolution equation, and instead is a constraint equation. It is not a solution to the Cauchy problem as it does not specify the second time derivatives of the metric, containing only first time derivatives instead. Instead, the four independent components in this equation act as constraints on the system, limiting the number of physical degrees of freedom and enforcing a subset from the full unconstrained space. The concept of constraint equations will become very important in Section 1.4 and in the work in Chapters 2, 3, and 4 as it becomes apparent that these constraints are not always easy to enforce in a simulation of spacetime, as numerical errors arise.

Overall, the number of degrees of freedom drops from 10 to 6. There are also 4 coordinate degrees of freedom which cut the number of physical degrees of freedom to 2. For gravity in the linear regime, these correspond to the plus and cross modes of gravitational waves.

1.1.4 Geodesics

An important concept in general relativity is the geodesic. A geodesic is a curve which is the shortest path between two points on a manifold. On a flat plane, geodesics take the form of straight lines but in curved space, the answer becomes more complex. Consider a curve $x^a(\lambda)$ in some arbitrary spacetime characterised by a single affine parameter λ. This curve is a geodesic if its tangent is parallel transported along its length.

The formal definition for parallel transport is that for a tensor $X^a{}_b$, it is parallel transported along $x^a(\lambda)$ if each of the tensor components are unchanged:

$$\frac{\mathrm{d}x^a}{\mathrm{d}\lambda}\nabla_a X^b{}_c \equiv \frac{\mathrm{D}}{\mathrm{d}\lambda}X^b{}_c = 0 \tag{1.15}$$

Then, if we have a curve $x^a(\lambda)$, the condition for it being a geodesic in terms of parallel transport is:

$$\frac{\mathrm{D}}{\mathrm{d}\lambda}\frac{\mathrm{d}x^a}{\mathrm{d}\lambda} = 0 \tag{1.16}$$

Expanding this, we find the geodesic equation:

$$\begin{aligned}\frac{\mathrm{d}x^b}{\mathrm{d}\lambda}\nabla_b\frac{\mathrm{d}x^a}{\mathrm{d}\lambda} &= \frac{\mathrm{d}x^b}{\mathrm{d}\lambda}\left(\frac{\partial}{\partial x^b}\frac{\mathrm{d}x^b}{\mathrm{d}\lambda} + \Gamma^a{}_{bc}\frac{\mathrm{d}x^c}{\mathrm{d}\lambda}\right)\\ &= \frac{\mathrm{d}^2x^a}{\mathrm{d}\lambda^2} + \Gamma^a{}_{bc}\frac{\mathrm{d}x^b}{\mathrm{d}\lambda}\frac{\mathrm{d}x^c}{\mathrm{d}\lambda}\\ &= 0\end{aligned} \tag{1.17}$$

The concept of null geodesics are important for many reasons, especially in that of defining the structure of spacetime itself. To identify a null geodesic, we enforce Equation (1.17) and make the demand that $\left(\frac{\mathrm{d}s}{\mathrm{d}\lambda}\right)^2 \equiv g_{ab}\frac{\mathrm{d}x^a}{\mathrm{d}\lambda}\frac{\mathrm{d}x^b}{\mathrm{d}\lambda} = 0$, which is the condition for a null spacetime interval.

1.1.5 Classical Field Theory

Another important mathematical topic in this thesis is classical field theory, which is concerned with the behaviour of fields in a classical, deterministic limit. Fields are mappings of physical quantities onto each event in spacetime. The goal of this theory is to then seek systems of equations which describe the evolution of these fields. One of the first stages in constructing a field theory is to identify the fields themselves. In relativistic electromagnetism, we consider a scalar potential and a three-dimensional vector potential, which then relate back to the electric and magnetic fields. General relativity, and so gravity, are also field theories. In Newtonian gravity, we devise equations for a vector gravitational field, or the force per unit mass experienced by a test particle at a point. In Einstein's gravity, we

generalise the concept of space and time into spacetime, introducing the metric tensor $g_{\mu\nu}$ which allows us to measure intervals on the spacetime manifold.

The action of classical field theory encompasses the potential and kinetic energies of the system in to a single scalar, and through the variation of this quantity, we find the evolution equations for a given system. We define the action $\mathcal{S}$ as the integral of the Lagrangian over the whole time domain:

$$\mathcal{S} = \int_{t_1}^{t_2} L(\vec{x}, \dot{\vec{x}}) \mathrm{d}t \tag{1.18}$$

Where $L = E_{\mathrm{KE}} - E_V$, and then E_{KE} and E_V are the kinetic and potential energies associated with the system respectively. We are concerned with the position vector $\vec{x}$ and its derivative with respect to time, $\dot{\vec{x}}$. The action is a scalar value assigned to the trajectory of the system from beginning to end across a phase space constructed by this pair of variables. Nature, in her classical form, demands a unique evolution for a system if given uniquely defined initial conditions, but one can imagine many possible paths from point A in phase space to point B. Imagine throwing a ball - we know that it will always follow the same trajectory if given the same initial push; the Euler-Lagrange equations are used to calculate this path. The action is a way of measuring the 'efficiency' of any given path. We fix the start and end points of the trajectory, and then integrate along every possible connecting path as in Equation (1.18) to find the respective action for each. The correct path follows the principle of least action; the path the particle takes is the one that produces a stationary value for the action under small variations in the path. In other words, the path for a particle is one which satisfies

$$\delta\mathcal{S} = 0. \tag{1.19}$$

This is all valid for simple classical systems, but now we need to generalise this to fields. We can think about fields in the sense of limits. Imagine assigning a value to every point in a discrete grid. Each of these points can be treated as above, with each having a value and derivative[2]. These values are each a degree of freedom.

[2]As an analogy only, we can think about the value and derivative of each point being like a position and a momentum.

We can now take the limit of vanishing separation between grid spaces so that it becomes a continuum and the values of the points become a distribution. This is now a field, where now we consider the evolution of the distribution of values and derivatives as opposed to singular degrees of freedom. In classical field theory, the evolution of these distributions is completely deterministic as with the simple classical system. In a quantum field theory, this continuum becomes a probability distribution and ceases being deterministic.

For a spacetime field of arbitrary rank and dimension $\Psi(x^a)$ and co-ordinates x^a, The action S is defined as the integral of the Lagrangian density over the region of interest

$$S = \int \mathcal{L}(\Psi, \partial_a \Psi) \mathrm{d}^4 x. \tag{1.20}$$

The Lagrangian density $\mathcal{L}$ is often defined in analogy to the Lagrangian L but integrates over the spatial coordinates as well as time. Here, one can derive the equations of motion for the field from the Lagrangian density. The Euler-Lagrange equations in terms of the Lagrangian density and the fields is

$$\frac{\delta S}{\delta \Psi^a} = \frac{\partial \mathcal{L}}{\partial \Psi^a} - \partial_b \left(\frac{\partial \mathcal{L}}{\partial \left(\partial_b \Psi^a \right)} \right) = 0. \tag{1.21}$$

Equation (1.21) can be applied to any field theory we want. We can substitute fields of any arbitrary rank, symmetry, and construction in for Ψ^a and find how those fields evolve. Consider a scalar field ϕ. In flat space, the action is

$$\mathcal{S} = \int \left[-\frac{1}{2} \partial^a \phi \partial_a \phi - V\left(\phi\right) \right] \mathrm{d}^4 x. \tag{1.22}$$

In analogy with the point particle system described earlier, we can associate the first term with a kinetic energy $\sim \dot{\phi}^2$ and the second term with the potential. Using Equation (1.21), we end up with the equations of motion for a scalar field in flat space:

$$\partial^a \partial_a \phi - \frac{\mathrm{d}V(\phi)}{\mathrm{d}\phi} = 0 \tag{1.23}$$

The form of the potential is dependent on the physics that we are considering. The simplest approximation for any symmetric minimum is a quadratic, with

the prefactor being interpreted as the squared mass of the particle. This is true regardless of the field theory we consider - any complicated potential can always be approximated in this way, provided that the energy scales of the problem do not cause the field to deviate far from the minimum and out of the quadratic regime. Different models of particles can be more fully expressed by adding terms to the action, or by updating the potential. In Chapters 2 and 3 I study the phenomena which arise from particles with self-interactions in their actions.

The generalisation from flat space to curved space is usually fairly simple, where we simply replace each occurrence of a partial derivative with a covariant one. There are some other more nuanced considerations however, involving the concept of tensor densities. One of the problems with moving from flat space to curved space is that certain key objects do not transform exactly as tensors and pick up additional factors of the Jacobian J when we change coordinate systems. For a tensor density of weight W, a factor of J^W appears in the transformation, and for the product of two tensor densities, the overall weighting is the sum of the individual weights, i.e., the density of the product of tensors with weights W_1 and W_2 is $W_1 + W_2$. This is often troublesome when performing tasks such as integration, for we want the integrand to be a scalar such that the sum of the each integrated element is the same regardless of the frame we consider. If the integrand is a tensor density instead, this does not hold. It transpires that $\sqrt{-g}$ is a tensor density of weight -1, and so we can multiply any tensor density by factors of $\sqrt{-g}$ to create a tensor density of weight 0, which is a 'normal' tensor.[3] The volume element $\mathrm{d}^n x$ is itself a tensor density of weight $+1$.

Therefore, the action integral in curved spacetime is written as

$$\mathcal{S} = \int \mathcal{L}\, \mathrm{d}^4 x. \tag{1.24}$$

Where the scalar Lagrangian L, is related to the Lagrangian density $\mathcal{L}$ via $\mathcal{L} = \sqrt{-g}L$. Equation (1.21) in curved spacetime becomes:

$$\frac{\partial L}{\partial \Psi} - \nabla_a \left(\frac{\partial L}{\partial \left(\nabla_a \Psi \right)} \right) = 0 \tag{1.25}$$

[3]One needs to be careful as different conventions can flip the signs of tensor densities and different pieces of literature can seem at odds with one another.

Then, the scalar field action in Equation (1.22) is written as:

$$\mathcal{S} = \int \left[-\frac{1}{2} \nabla^a \phi \nabla_a \phi - V(\phi) \right] \sqrt{-g} \, \mathrm{d}^4 x \tag{1.26}$$

The power of the action is that it allows us to express the physical properties and couplings between terms of a theory. General relativity is in itself a field theory, with the Lagrangian being the Ricci scalar. The Einstein-Hilbert action is the simplest field theory involving the metric tensor, and so the action for general relativity is

$$\mathcal{S} = \int \sqrt{-g} \, R \, \mathrm{d}^4 x. \tag{1.27}$$

The Einstein field equations can be derived directly from this action with the same principles as was used in scalar field example. The principle of least action for curved spacetimes supposes that the equations of motion for a field theory are those which leave the action unchanged under small variations of the field itself. The field in general relativity is the metric, so we recover the field equations from $\delta\mathcal{S}/\delta g^{ab}$. We can therefore equate this with the energy-momentum tensor including some extra prefactors, forming the right hand side of the Einstein field equation. The full definition is

$$T_{ab} = -\frac{2}{\sqrt{-g}} \frac{\delta \mathcal{S}}{\delta g^{ab}}. \tag{1.28}$$

From Equation (1.28), we can then recover the Einstein field equations. This definition of the energy-momentum tensor additionally holds for any other field theory.

1.2 Spacetimes

One of the simplest spacetimes to consider is flat space. The associated metric is the Minkowski metric η_{ab}, whose line element is given in Cartesian coordinates $\{t, x_1, x_2, x_3\}$ by:

$$\mathrm{d}s^2 = -\mathrm{d}t^2 + \mathrm{d}x_1^2 + \mathrm{d}x_2^2 + \mathrm{d}x_3^2 \tag{1.29}$$

In matrix form, this is:

$$\eta_{ab} = \mathrm{diag}\,(-1, 1, 1, 1) \tag{1.30}$$

The minus sign prefactor to the time coordinate specifies it as a time-like co-ordinate rather than a space-like one. This spacetime is a vacuum, and so the Ricci tensor vanishes. It also has no curvature, so the Riemann tensor vanishes too. These statements are not equivalent however. There are many examples of spacetimes which are vacuum solutions but also have curvature, such as the various types of black holes.

1.2.1 Static Black Holes

A black hole is a region of space interior to which light cannot escape. The the curvature of space inside a black hole is sufficiently strong that any outwardly directed ray of light will at some point return inside, and so cannot reach an external viewer. The radius at which this escape becomes prevented is known as the event horizon, which delineates the two regions which are causally disconnected from one another. The 'no-hair' theorem states that black holes may only have the externally-observable properties of mass, charge, and angular momentum. The Schwarzschild black hole is a static black hole with no properties apart from mass. It is a symmetric spacetime, described by the following metric in spherical coordinates $\{t, r, \theta, \phi\}$

$$\mathrm{d}s^2 = -\left(1 - \frac{2M}{r}\right)\mathrm{d}t^2 + \left(1 - \frac{2M}{r}\right)^{-1}\mathrm{d}r^2 + r^2\mathrm{d}\Omega^2. \tag{1.31}$$

$\mathrm{d}\Omega^2 = \mathrm{d}\theta^2 + \sin^2\theta\mathrm{d}\phi^2$ and is the metric on the surface of a three-dimensional sphere, and M is the gravitating mass. According to Birkhoff's Theorem, this is the unique spherically symmetric, static solution for vacuum spacetime. We need to be careful now and make a distinction between different types of singularity. Naively looking at Equation (1.31), we might deduce that there are two singularities present in this metric - one at the Schwarzschild radius $r = 2M$ and a second at $r = 0$. The singularity at $r = 2M$ is not a 'true' singularity in the sense that it is only an artefact of the specific co-ordinate system we have chosen - the curvature does not become infinite here. This metric is just insufficient for describing space at this point. A simpler example would be for a polar-coordinate $\{\rho, \theta\}$ system

on a two-dimensional plane whose line element is

$$\mathrm{d}s^2 = \mathrm{d}\rho^2 + \rho^2 \mathrm{d}\theta^2. \tag{1.32}$$

At $\rho = 0$, we have an infinite number of coordinates mapped to a single point of the manifold for $0 \leq \theta < 2\pi$. There is no singularity as such - the coordinate system has just broken down at this point. One can even forcefully introduce a co-ordinate singularity here by making a co-ordinate transformation $\rho \to 1/\rho'$. The interval becomes

$$\mathrm{d}s^2 = \frac{1}{\rho'^4}\left(\mathrm{d}\rho'^2 + \rho'^2 \mathrm{d}\theta^2\right). \tag{1.33}$$

Now, it's explicit that at $\rho' = 0$ there is a singularity and so the coordinate system breaks down. As this is equivalent to Equation (1.32), however, it proves that this singularity is artificial. We can therefore make a coordinate transformation to treat the pathologies in the Schwarzschild metric in Equation (1.31). Different coordinate systems have different drawbacks. The Schwarzschild metric has this singularity at the horizon which makes it unsuitable for use in numerical relativity. When running simulations, we desire coordinate systems which are continuous across the horizon so that the field evolves smoothly. These are known as horizon-penetrating coordinates.

The first step is to introduce a different radial coordinate. We 'push' the horizon to infinity by introducing a sufficiently slowly advancing radial coordinate known as the tortoise coordinate r^*. It is defined as

$$r^* = r + 2M \ln\left(\frac{r}{2M} - 1\right). \tag{1.34}$$

Here, r is the Schwarzschild radial coordinate. The metric becomes

$$\mathrm{d}s^2 = \left(1 - \frac{2M}{r}\right)\left(-\mathrm{d}t^2 + \mathrm{d}r^{*2}\right) + r^2 \mathrm{d}\Omega^2, \tag{1.35}$$

and is known as the tortoise metric. We notice that the $r = 2M$ singularity has been pushed to $r^* = -\infty$ and so cannot be reached. We now face a different problem however. We cannot represent infinity in a finite-size computational domain, and so we lose the ability to explore the spacetime near the black hole horizon. As such, we

seek a way to make a further modification so that the horizon of the black hole is at a finite coordinate, but is not a singularity. In Eddington-Finkelstein coordinates, the choice for the coordinates is informed by ingoing (or outgoing) rays of light

$$v = t + r^*, \tag{1.36}$$

$$u = t - r^*. \tag{1.37}$$

For ingoing and outgoing rays of light, v and u are constant respectively. We can check this by first considering a null geodesic ($\mathrm{d}s^2 = 0$), then for Schwarzschild coordinates

$$\frac{\mathrm{d}r}{\mathrm{d}t} = \pm\left(1 - \frac{2M}{r}\right). \tag{1.38}$$

With the definition of the tortoise coordinate, we find: $\mathrm{d}r^*/\mathrm{d}t = (\mathrm{d}r/\mathrm{d}t)\,(\mathrm{d}r^*/\mathrm{d}r) = \pm 1$. Overall therefore for null geodesics, we observe

$$t \pm r^* = \text{const.} \tag{1.39}$$

These two permutations are precisely the new coordinates we introduce. We can choose to follow an ingoing null geodesic and replace t with v, and then swap back to the traditional Schwarzschild r to find the Eddington-Finkelstein metric:

$$\mathrm{d}s^2 = -\left(1 - \frac{2M}{r}\right)\mathrm{d}v^2 + 2\mathrm{d}v\mathrm{d}r + r^2\mathrm{d}\Omega^2 \tag{1.40}$$

Note that we have now a new null coordinate v, and have picked up a $\mathrm{d}v\mathrm{d}r$ cross term, but overall the line element looks similar to Equation (1.31). This is an example of horizon penetrating coordinates; we no longer encounter a singularity at $r = 2M$ and the rest of the space-like coordinates are continuously defined up until the true singularity at $r = 0$. We cannot yet use these coordinates to simulate spacetime however - the coordinate v is null and so not suitable for use as a spatial coordinate. Therefore, we must devise a coordinate system with this horizon-penetrating property but clearly defined space and time coordinates.

1.2.2 Rotating Black Holes

Beyond mass, we have two other independent parameters we can use to describe black holes without violating the no-hair theorem - angular momentum and charge. For the purposes of this thesis, I do not study charged black holes (Reissner-Nordström and Kerr-Newman black holes depending on if they have angular momentum or not) as they are expected to only be minute fractions of all black holes, if any, as opposed to Kerr black holes, which we know to be the overwhelming majority of the population. A Kerr black hole is one with the properties of mass and angular momentum. One of the most common representations of Kerr spacetime is with Boyer-Lindquist coordinates $\{t, r, \theta, \phi\}$

$$\begin{aligned} \mathrm{d}s^2 = &-\left(1-\frac{2Mr}{\rho^2}\right)\mathrm{d}t^2 - \frac{4Mar\sin^2\theta}{\rho^2}\mathrm{d}t\mathrm{d}\phi + \\ &+\frac{\rho^2}{\Delta}\mathrm{d}r^2 + \rho^2\mathrm{d}\theta^2 + \frac{\sin^2\theta}{\rho^2}\left(\left(r^2+a^2\right)^2 - a^2\Delta\sin^2\theta\right)\mathrm{d}\phi^2. \end{aligned} \tag{1.41}$$

There are two functions ρ and Δ defined for convenience, which are

$$\rho^2 = r^2 + a^2\cos^2\theta, \tag{1.42}$$

$$\Delta = r^2 - 2Mr + a^2. \tag{1.43}$$

The unique feature of the Kerr metric is the spin parameter a, defined as the angular momentum J per unit mass of the black hole, $a = J/M$. These are horizon-penetrating coordinates with a clear distinction in the coordinates between space-like and time-like. We can simplify the Kerr metric further by considering Kerr-Schild coordinates, which introduce a conformal-Cartesian element to the spatial components

$$\begin{aligned} \mathrm{d}s^2 = &-\mathrm{d}t^2 + \mathrm{d}x^2 + \mathrm{d}y^2 + \mathrm{d}z^2 + \frac{2Mr^3}{r^4+a^2z^2}\Big(\mathrm{d}t + \frac{z}{r}\mathrm{d}z + \\ &+\frac{r}{r^2+a^2}\left(x\mathrm{d}x + y\mathrm{d}y\right) - \frac{a}{r^2+a^2}\left(x\mathrm{d}y - y\mathrm{d}x\right)\Big)^2. \end{aligned} \tag{1.44}$$

Where $r^2 = x^2 + y^2 + z^2$. With all of this discussed, the basic tool-kit of general relativity is in place and several relevant spacetimes have been introduced. We now proceed to cover the right hand side of the Einstein field equations - matter.

1.3 Dark Matter in the Universe

1.3.1 Motivation

The constitution of the Universe has been of continuous study and fascination since the earliest times in human history. We have always had the ambitious objective of trying to sort the components of the Heavens into definable categories, and often when encountering new thoughts and observations which contradict these models, new discoveries in physics have been made. In the tradition of classical Greek philosophy, the world was thought to be subdivided into the four terrestrial elements of air, earth, water, and fire, then an elusive fifth element known as the aether which made up the heavens (Aristotle, 350 BCE). In modern astrophysics, we have a similar fascination in learning the composition of the Universe around us. It is one mysterious equivalent of the Aristotelian aether which is the primary object of concern for the rest of this thesis: dark matter.[4]

We currently only know the constitution of $\approx 5\%$ of the Universe (Aghanim et al., 2020). This is ordinary, visible matter as we know it, and makes up the particles, planets, stars, and galaxies which we can observe. What consists the rest of the Universe is currently unknown. It is commonly split into two discrete subcomponents - dark matter and dark energy. 'Dark' means that we cannot directly observe these components as they either do not, or have incredibly weak interactions with the electromagnetic sector and so are not visible in an optical sense. There are many different proposed models for dark energy, such as the cosmological constant (Carroll, 2001; Peebles and Ratra, 2003), and scalar field models such as quintessence (Ratra and Peebles, 1988; Wetterich, 1988; Ferreira and Joyce, 1998; Copeland, Liddle, and Wands, 1998). These have measurable effects such as causing the accelerated expansion of the Universe on the large scales. In this work, I am instead concerned with the nature of dark matter. Like with dark energy, we cannot directly observe dark matter, but instead can infer the effects it has on ordinary matter and on light.

[4]Dark energy constitutes the vast majority of energy in the Universe and is a fascinating area of study, but is not relevant for this thesis.

In the past hundred years, astronomers and theoreticians have been making observations which seemingly contradict our current understanding of gravity by assuming that the total mass of matter in space is accounted for purely by what is visible. The detection of anomalous gravitational effects in clusters by Zwicky led him to hypothesise the existence of *'dunkle Materie'* to account for the missing mass (Zwicky, 1933). Many similar observations have also been drawn. For a long time, rotation curves have been the source of many conclusions concerning dark matter. In particular, the observation of the unusual rotation curve of M31 lead to speculation that its incompatibility with the conventional understanding of galaxy dynamics could be resolved by it having a flatter mass distribution, going beyond the visible edge of the galaxy (van de Hulst, Raimond, and van Woerden, 1957; Schmidt, 1957). Observations by Vera Rubin of numerous galaxies built upon this, suggesting that either Newtonian physics was insufficient for describing the properties of these galaxies, or that a large fraction of the galaxies' mass must reside in the relatively dark halo (Rubin, Ford, and Thonnard, 1980).

There have also been other probes into the existence of dark matter. Gravitational lensing is an effect where the distortion of spacetime by matter causes the path of light to bend (Einstein, 1916). This effect can be used to weigh objects such as galaxy clusters, and therefore calculate the amount of 'missing mass' not accounted for by the total luminosity of the object (for example, see Bartelmann, 2010). Another piece of evidence for dark matter comes from the Bullet Cluster (1E 0657-56). This consists of a pair of galaxies post-collision, with one having passed through the other. As with the lensing technique, the on-sky visible mass of the cluster is offset from the gravitational mass, implying there is an additional mass component (Clowe, Gonzalez, and Markevitch, 2004; Markevitch et al., 2004). The Bullet Cluster is also cited as a counter-argument to Modified Newtonian Dynamics, or MOND (Milgrom, 1983). This is theory which proposes that the effects attributed to dark matter can instead be explained by modifying gravity on low energy scales. The counter-argument from the Bullet Cluster against MOND is that the additional force terms present with MOND do not accurately resolve

the discrepancy between visible mass and gravitational mass in the cluster, and so cannot be an explanation to this discrepancy.

1.3.2 The Nature of Dark Matter

Given the compelling evidence suggesting the existence of dark matter, the question is now of its nature (for some reviews, see Bertone, Hooper, and Silk, 2005; Feng, 2010; Ferreira, 2021. There are two broad categories of dark matter - macroscopic objects and particles. This first category consists of Macroscopic Compact Halo Objects (MaCHOs) (Paczynski, 1986; Tisserand et al., 2007; Jacobs, Starkman, and Lynn, 2015) and primordial black holes. (Carr et al., 2010; Capela, Pshirkov, and Tinyakov, 2013b; Capela, Pshirkov, and Tinyakov, 2013a; Belotsky et al., 2014). These objects either emit no light, or are too dim to be seen from Earth, and so qualify as dark matter due to our lack of ability to detect them. The other main class of dark matter candidates is particle dark matter (Bertone and Merritt, 2005; Feng, 2010). Particle dark matter can be further subdivided based on mass, which is inversely proportional to Compton wavelength. The longer wavelength, lower mass candidates generally exhibit wave-like behaviour while the short wavelength, higher mass candidates exhibit particle-like behaviour. Crucially, the nature of a dark matter candidate being wave-like or particle-like depends on the length scales in which we are interested. If the Compton wavelength of a candidate is approximately equal to or greater than the scale we are investigating (for example a Schwarzschild radius) then the candidate exhibits wave-like behaviours, with the inverse holding for Compton wavelengths smaller than the scale of interest. It is therefore important to distinguish what the scale of interest is. For example, dark matter which exhibits particle-like properties on scales of galaxies may exhibit wave-like behaviour on scales of a solar mass black-hole Schwarzschild radius. Particle dark matter consists of beyond-standard model particles and fields and span many orders of magnitude in energy scale. They have very weak couplings with the standard sector and so do not interact strongly with photons, but still interfere gravitationally with other bodies and can account for the 'missing mass' in the various tests for dark matter. Another

attribute of dark matter of all forms is its 'temperature', or dispersion velocity. It can be cold, hot, or other classifications. Cold dark matter itself forms a central component of the most popular contemporary cosmological model, the ΛCDM model (Carroll, 2001; Peebles and Ratra, 2003; Aghanim et al., 2020). In this thesis, I focus on the lighter dark matter candidates which comprise wave-dark matter.

1.3.3 Wave-like Dark Matter

Ultra-Light Dark Matter (ULDM) (Hui, 2021; Hu, Barkana, and Gruzinov, 2000) comprises a class of beyond-standard model bosons whose masses range approximately from 10^{-24} – 1 eV. Many models are contained within this definition, but the uniting properties are that on galactic scales, they behave as cold dark matter, and so agree with the ΛCDM model, but on smaller scales inside galaxies below the Compton wavelength of the matter, it becomes wave-like. On these scales, the specific nature of dark matter is less well-understood, and so is an interesting area for exploration. The behaviour of a field of wave-like dark matter is primarily governed by its mass and its potential, which inevitably arise in any field theory as the lowest-order approximation of any minimum. The finer behaviours of these different models is dictated by the action of the field as mentioned in Section 1.1.5.

Wave dark matter models are compelling to consider due to their ability to potentially resolve a number of issues surrounding ΛCDM. First is the core-cusp problem (Moore, 1994; Oh et al., 2015). The formation of galaxies is studied using N-body simulations with collisionless, or cold dark matter. The density profiles of the dark matter resulting from these simulations are 'cuspy', which spike in density at low radii. The problem arises as observations of dark mater distributions in galaxies show a 'cored' distribution instead - a profile which flattens out at low radii. Different solutions have been posed, including supernova feedback causing fluctuations in the central regions of galaxy potentials leading to more cored dark matter profiles (Pontzen and Governato, 2012), and supernova-driven outflows ejecting dark matter from the central halo (Navarro, Eke, and Frenk, 1996). Other solutions have been posed which involve changing the model of dark matter. One

observation is that using self-interacting dark matter models makes simulations agree with observations. This repulsive self-interacting dark matter has a larger interaction cross-section than the case with no self-interactions, so produces a core which has a larger central velocity dispersion, i.e. is 'hotter', and so disperses matter and lowers the central density (Elbert et al., 2015). Others find that warm dark matter haloes form later than CDM (cold dark matter) haloes, so have less time to build up a cusp and so agree with the cored results in nature (Lovell et al., 2012). In addition to this, there is the dwarf galaxy problem, or missing satellites problem. Observations of galaxies within the local group (Mateo, 1998) reveal that that there is an order of magnitude fewer galaxies and dark matter haloes than analytics (Press and Schechter, 1974; Kauffmann, White, and Guiderdoni, 1993) and numerics (Moore et al., 1999; Klypin et al., 1999) predict. Again, a solution which has been posed to this is to consider alternative models of dark matter to resolve these discrepancies (Tulin and Yu, 2018). Wave dark matter with masses in the range of 10^{-22} – 10^{-20} eV, also known as fuzzy dark matter (Hu, Barkana, and Gruzinov, 2000), also solves the above core-cusp and missing satellites problem. In essence, the greater free-streaming length of fuzzy dark matter causes structure to dissipate out of its own gravitational potentials (Hogan and Dalcanton, 2000), suppressing the growth of structure and flattening the central density profile of dark matter haloes, therefore reducing the number which form in total. One can also explore dark matter candidates with more degrees of freedom. Various models include scalar, vector, and tensor particles (See Graham, Mardon, and Rajendran, 2016; Farzan and Akbarieh, 2012; Kolb and Long, 2021; Aoki and Mukohyama, 2016). One motivation for looking at these models is simply that they are possible candidates, and so there is no reason to artificially limit the number of options investigated. Additionally, due to the ongoing non-detection of WIMPs (Weakly-Interacting Massive Particles) (Jungman, Kamionkowski, and Griest, 1996; Aprile et al., 2018; Akerib et al., 2017; Feng, 2010), it becomes more compelling to search for alternative models. Certain physical mechanisms are enhanced with these higher-rank fields such as the phenomenon of superradiance (Zel'Dovich, 1971a;

Brito, Cardoso, and Pani, 2015). This is an effect where a field extracts angular momentum from a rotating black hole and converts it into energy for itself. It has been found that vector (Pani et al., 2012b; Pani et al., 2012a; Witek et al., 2013) and tensor fields (Brito, Cardoso, and Pani, 2013; East and Siemonsen, 2023) have potentially orders of magnitude shorter excitation scales than scalars and so makes them interesting to study. Tensor dark matter will be discussed further in Chapter 4.

In addition to investigating different spins of dark matter, one can study models with various potentials. For many massive scalar particles, the potential is quadratic $V(\phi) \approx m^2\phi^2$ (where ϕ is the field and m is the mass). This is the lowest order approximation of a minimum, and so any higher-order field theory will appear as a quadratic when sufficiently close to the minimum. Models with different potentials include self-interactions (Carlson, Machacek, and Hall, 1992). These have additional quartic $\mathcal{O}(\phi^4)$ terms in potential, coupled by some hyper parameter known as the interaction strength. Depending on the sign of this parameter, one has families of potentials with different properties and as will be discussed in Chapters 2 and 3, this can result in vastly different behaviour for the wave dark matter field. When studying particles with these higher-order terms, the energy scale of the field becomes more important. The average energy of the field may be such that the quadratic parts of the potential play no role in the field's behaviour, or completely dominate it instead, and now has the opportunity to transition from one regime to another. These regimes scale as $\sim \phi^2$ and $\sim \phi^4$. As a result, we could consider a certain class of ULDM where the self-interaction coupling strength of the field means that the quartic regime only becomes important at high energies, for example in the early Universe, or even not at all in different astrophysical contexts. Similarly, there are situations where the quartic part is dominant and so the mass of the particle has little to no effect on its behaviour. We can explore further by considering models of dark matter with multiple minima. These self-interactions so far broadly represent the addition of repulsive or attractive forces to purely massive models of dark matter. The addition of terms which are asymmetric about the central minimum or ones which add additional minima introduce a rich new phenomenology

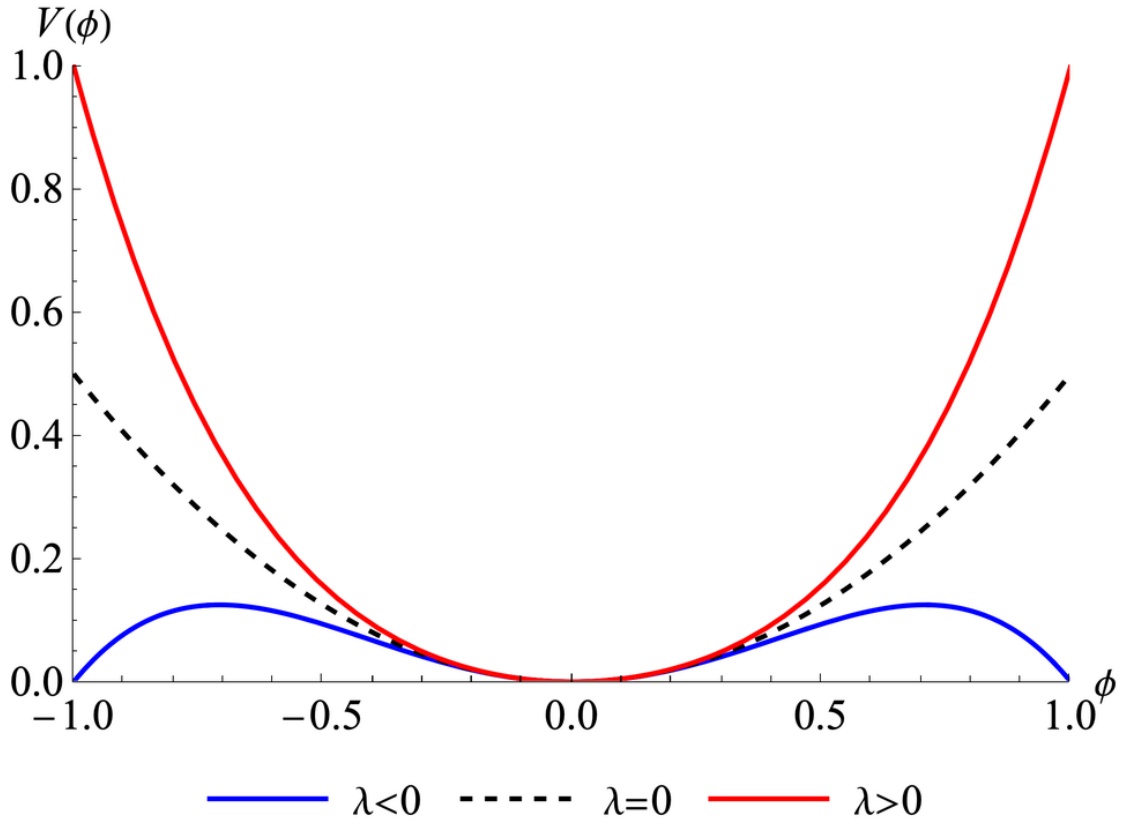


Figure 1.1: Examples of self-interacting potentials of the form $\approx m^2\phi^2 + \lambda\phi^4$ with different values for λ. Potentials with $\lambda > 0$ have a positive quartic term which makes the gradient of the potential steeper. Potentials with $\lambda < 0$ have a negative quartic term instead. At some value of therefore ϕ, a pair of maxima are introduced and the potential turns over and starts decreasing. A quadratic potential ($\lambda = 0$) has been plot as well for reference.

which can be explored. A classic example of such a dark matter candidate is the axion (Weinberg, 1978; Wilczek, 1978). Axions are motivated from particle physics by the 'strong charge-parity' problem, or strong CP problem, which is one of the significant challenges of modern particle physics. (see Peccei, 2008 for example). CP symmetry is the expectation that the laws of physics remain the same under the exchange of a particle with it's antiparticle (charge symmetry) and under the inversion of its position (parity symmetry). This was considered to be a fundamental law, but was proven to be false in the electroweak case. The first demonstrated violation of this theory was found in the decay of kaons (Christenson et al., 1964)[5]. Since then, there have been numerous other experiments and observations which

[5]This was so significant that it led to the group's winning of the 1980 Nobel Prize

demonstrate violations of CP symmetry in the electroweak force (Kobayashi and Maskawa, 1973; Covi, Roulet, and Vissani, 1996; Alavi-Harati et al., 1999; Fanti et al., 1999; Aubert et al., 2001; Abe et al., 2001). There has been no such evidence for CP violation in the strong force however, Nature seemingly conserves it. This is known as the 'strong-CP problem'. Axions were initially motivated as a consequence of Peccei-Quinn theory (Peccei and Quinn, 1977a; Peccei and Quinn, 1977b) which poses a new symmetry and complex scalar field in the standard model which spontaneously breaks this symmetry at low energies. The axion then arises due to this broken symmetry and helps to suppress it, therefore 'solving' the strong CP problem. Whilst the original form of Peccei-Quinn theory has been since ruled out by experiments (for example, Asano et al., 1981), there have been developments leading to ultra-light or 'invisible' axions. These light axions fit the definition of wave dark matter and as such are themselves compelling candidates of study (for example, Choi, Im, and Sub Shin, 2021; Chadha-Day, Ellis, and Marsh, 2022). Axions (just considering the real component) have periodic potentials and so the energy or 'temperature' of the field plays an intriguing role in its dynamics. An axion field in the early Universe might have sufficient temperature such that the field oscillates freely between multiple minima, then as it cools down, settles in one of minima, becoming confined and so unable to visit the others. This case with axions is just one example of phenomena which can occur when considering wave dark matter fields with multiple minima. This is explored further in Chapter 3.

1.3.4 Multi-Minima Potentials

In this thesis, I focus on two particular models and mechanisms associated with multi-minima potentials for scalar fields. The first case is symmetry restoration, which involves a double-well potential with minima of equal depth, and the second is vacuum decay, which involves a double-well potential with minima of unequal depth. In symmetry restoration, we initially consider a homogeneous scalar field with a value such that it is confined in one of the two equal-depth wells. Assuming that the potential is symmetric around zero, this gives the field a non-zero expectation

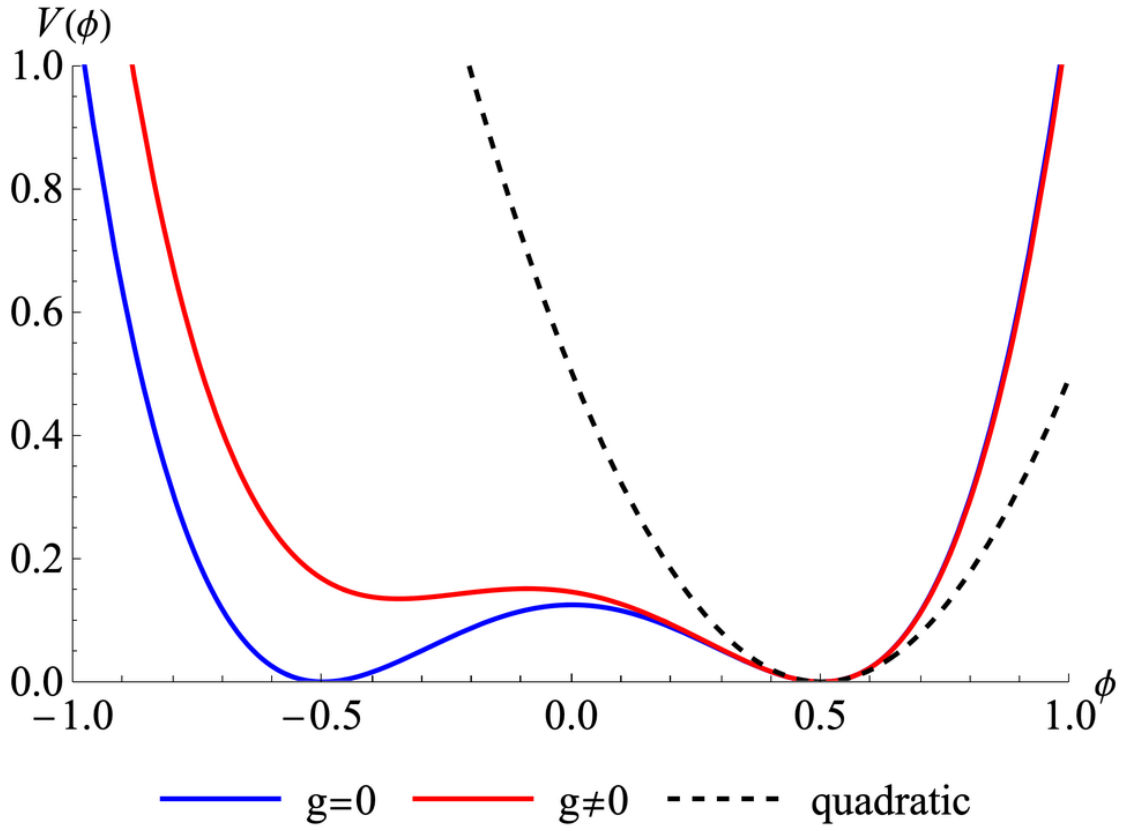


Figure 1.2: Examples of multi-minima self-interacting potentials with asymmetry parameter g - see Chapter 3 for the exact form. Potentials with $g = 0$ are symmetric about $\phi = 0$, while a non-zero g introduces asymmetry through raising (or lowering) one of the minima. In the locality of each minimum, the potential is approximately quadratic then deviates as ϕ increases or decreases. The $g = 0$ potential is associated with the phenomenon of symmetry breaking and restoration while the $g \neq 0$ potential is associated with vacuum decay.

value as it oscillates in either the positive or negative well. If we then mirror the oscillations field around the central axis, the expectation value changes sign, meaning the field is in an asymmetric state. If we increase the energy scale of the field through some mechanism so it exceeds that of the central barrier, the field oscillates equally between the two minima and so enters a symmetric state - the expectation value is invariant under the inversion of the field around the central axis. In effect, the smaller details of the potential are 'washed out', leaving only the overall shape as having any effect on evolution.

The concept of symmetry restoration is intrinsically linked to the energy scales of the problem; the mechanism relies on the initial trapping of the field in one half

of the well, and then gaining enough energy to exceed the central barrier and so oscillate between both wells. If the field is on an energy scale larger than the size of the central barrier, it will be in a symmetric state from the start. Therefore, there must be a way for symmetry to initially be broken. Imagining a field in the very hot and energetic pre-inflationary early Universe, the field will be of a high temperature and so likely in a symmetric phase where the central barrier is on a much lower energy scale and so irrelevant. During inflation, the rapid cooling and expansion of the Universe can lower the energy of the field and taking into account quantum fluctuations, cause a series of patches existing in different symmetry-broken stages to appear. This inhomogeneous field can then undergo symmetry restoration through some catalyst to then bring the field back into a homogenous, symmetric state. This is the topic of interest in Chapter 2, specifically, the mechanism which can increase the energy of the field so that it can overcome the central barrier.

The other scenario we are interested in here is the vacuum decay case. As mentioned before, we examine a potential with two minima but of unequal depths, breaking symmetry about the central axis. Due to the asymmetry of the potential, there are now two separate possibilities for initial conditions where the field is confined to a single well - either the field begins in the higher well or in the lower well. We first look at the field beginning in the higher well. The field starts by oscillating around this minimum, having no knowledge of the other potential well. As with symmetry restoration, the field can eventually surpass the central barrier through a mechanism which gradually increases the energy of the field. Due to the unequal depths however, there is new quantum mechanism by which the field can cross the barrier known as quantum tunnelling. In brief, quantum tunnelling gives a finite probability that the particle will 'tunnel' from the shallower potential well and into the deeper one through the principles of uncertainty. The greater the energy of the field or of particle relative to the barrier, then the higher this probability is. Regardless of which mechanism causes this to occur, if the field reaches the other side, it cascades down into the deeper well and becomes trapped in it. Gradient forces 'drag' the rest of the field into this state too, and

the excess energy is fuelled into a bubble of this 'true vacuum' which expands radially outwards from the initial seed collapse.

The field can also begin in the deeper well. In this case, quantum tunnelling is disfavoured as it is energetically unfavourable for the field to cross the barrier into a state with greater vacuum energy. If the field is excited and so oscillates with enough amplitude to surpass this barrier, then we would see the field oscillate between the two minima like with the symmetry restoration scenario. Instead of the field having an expectation value of zero however, we would see the field spend a comparatively greater amount of time in the deeper well which skews the expectation value towards being non-zero, and so the state, like the potential, remains asymmetric. Given a large enough amplitude of oscillation, we approach the limit of the symmetry restoration scenario with the details of the barrier being washed out, and the field oscillating as if the potential was single-welled. This is investigated further in Chapter 3.

I am interested in a classical mechanism for the field to gain energy and increase the amplitude of oscillations, which is black hole accretion. The principle is that the geometry of spacetime around a black hole is such that a cloud of wave dark matter will infall and accrete onto the horizon of the black hole. This is a novel mechanism, and is discussed in more detail in both Chapters 2 and 3. This process is by nature completely classical, and so offers a different avenue of study for self-interacting dark matter models instead of quantum methods. In this sense, we can use black holes as a particle detector - throughout their lives, if the black holes are immersed in a cloud of wave dark matter, the accretion of this matter onto the black hole potentially produces observational signatures. If we are able to detect clouds of wave dark matter around black holes and measure their density profiles, then by matching the measured density profiles with different theoretical models corresponding with specific models of particles, then we may be able to gain an insight into the specific nature of dark matter. This scenario is limited by the nature of the environment and the dark matter itself however. If the density of the cloud is too low, or the mass of the black hole too small, then there will

be insufficient time from the formation of the black hole to the present day for any detectable amount of accretion to have occurred.

1.4 Numerical Relativity

1.4.1 Prelude

General relativity is an incredibly powerful theory, but there are limits to where purely analytical methods can take us. Analytics are well adapted to scenarios which are perturbative, and either have high degrees of symmetry or behave in ways which have a separation of timescales, so that rapid changes in geometry or the distribution of matter can be set aside and compared differently to larger scale changes happening on longer timescales. There are many dynamical, strong field scenarios where we cannot apply standard analytical techniques. Either the distribution of matter or curvature of spacetime becomes too complex to model and is not possible to simplify with various techniques, or that it would be possible to do so but only at great effort and in a narrow scope. As discussed in Section 1.1, there has been a recent boom in the amount of precision to which we can observe our universe, and especially in strong field regimes. For theory to keep pace with the ever-increasing detail we find in experiments, so too must our ability to model and explore these scenarios. The first attempt to simulate spacetime was done by Hahn and Lindquist, 1964, where they modelled the gravitational interaction between two masses by solving Einstein's equations. There was then a development of interest in simulating the collision of two black holes using various symmetries and simplifications (Cadez, 1971; Smarr, 1975; Eppley, 1975). The first 'full' 3+1 numerical solution was then done by Anninos et al., 1995 , but it would take until the new millennium with Pretorius, 2005; Campanelli et al., 2006; Baker et al., 2006 to simulate full binary black hole inspirals, mergers, and ringdowns with enough accuracy in these difficult dynamical scenarios. Since then, there has been a renaissance in numerical relativity, with it being applied to a huge variety of different scientific scenarios - see Alcubierre, 2008; Bona, Palenzuela-Luque, and Bona-Casas, 2009; Baumgarte and Shapiro, 2010 for a series of textbooks.

1.4.2 The Foliation of Spacetime - 3+1 Physics

The key idea which numerical relativity employs to turn the Einstein field equations into a series of evolution equations is that of foliation. By looking at Equation (1.28), we do not have sufficient information to run a simulation. Crucially, we have not made any key distinction between space and time - we could conceive of some coordinate transformation to 'rotate' the space and time coordinates in to each other for example. To resolve this, we need to choose a privileged time coordinate, and then separate the rest into spatial ones. This is known as the foliation of spacetime, or '3+1' casting of general relativity. By choosing this unique time coordinate, the rest of space can be 'sliced' into a series of three-dimensional snapshots which can then be progressed through by the advancement of the time coordinate.

This foliation is known as the Cauchy problem. To solve it for a set of differential equations, we must prescribe a series of initial field values and derivatives which produces a unique evolution dependent solely on these initial conditions. In other words, if we have a set of unique initial conditions, can we guarantee a unique evolution? In terms of numerical relativity, this involves specifying some initial conditions for the spacetime - the metric and its first derivatives - and the values and momenta of any matter fields present. From these, we can then integrate everything forward and so obtain the evolution of our system. Another crucial aspect is whether the system we devise is well-posed or not. This demands that the partial differential equations we find from our foliation depend continuously on the initial data, meaning that a small change in the initial conditions induce only small changes in the evolution and solution of the system. More formally, well-posedness can be expressed by:

$$||u(t,x)|| \leq ke^{At}||u(0,x)|| \tag{1.45}$$

Here, k and A are arbitrary constants. Essentially, Equation (1.45) means that the norm of the solution $||u(t,x)||$ is bounded within some independent exponential prefactor of the initial data $||u(0,x)||$. Next, some additional notation will be defined - it will be important to distinguish between four-dimensional objects and

three-dimensional objects in the next section, we need to introduce spacetime and spatial indices. Spacetime indices behave as normal, and run from 0 to 3 over the four spacetime dimensions and are denoted with Greek letters. Spatial indices run solely from 1 to 3 and are denoted with Latin letters.[6] The task now is to find a way to divide our four-dimensional spacetime $\mathcal{M}$ into a series of three-dimensional slices Σ_i, parameterised by some universal time coordinate t_i, which is constant across each individual slice. Suppressing a spatial dimension for readability, this situation is illustrated in Figure 1.3. This foliation is the essence of the Cauchy

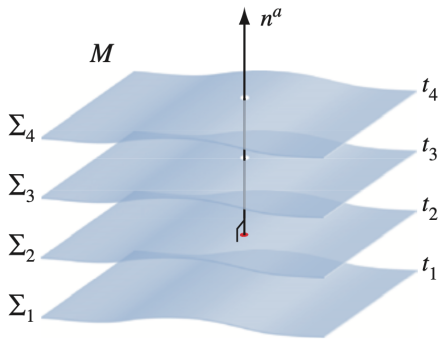


Figure 1.3: An example on the foliations of the spacetime M. The different hypersurfaces Σ_i are characterised by the times t_i and have the associated normal vector n^a. Figure from Baumgarte and Shapiro, 2010

problem. Recalling the 3+1 splitting we mentioned previously, we can now imagine how to solve this problem. We want to construct a series of purely spatial tensors and functions which exist solely on each spatial slice Σ_i. We then define a normal vector n^a which then informs us how these different spatial tensors evolve with increasing time coordinate t as we move from slice to slice. How do we relate n^a to t however? We can begin by considering the one form $\nabla_a t$. We can then define a scalar quantity pertaining specifically to the time interval between each slice (the equivalent of $\mathrm{d}t^2$) by taking the norm of $\nabla_a t$:

$$g^{ab}\nabla_a t \nabla_b t = -\frac{1}{\alpha^2} \tag{1.46}$$

[6]This notation can be flexible depending on context. For example, an object which is purely spatial is agnostic to the whether the indices are spatial or not so can be written with either. This is important mostly for non-spatial objects where this distinction is key, and for general readability.

The scalar α is called the lapse function and relates to the passage of time between each hypersurface for normal observers. We can then define a normalised one-form

$$\omega_a = \alpha \nabla_a t. \tag{1.47}$$

And so, the vector dual to this one form found by raising an index is:

$$n^a = -g^{ab}\omega_b \tag{1.48}$$

The minus sign is chosen so that $\|n^a\| = -1$, denoting it as a timelike vector. We now want to find the spatial equivalent for the metric $g_{\mu\nu}$. We first define a key object known as the projection operator

$$\begin{aligned} \gamma^{\mu}{}_{\nu} &= g^{\mu}{}_{\nu} + n^{\mu} n_{\nu} \\ &= \delta^{\mu}{}_{\nu} + n^{\mu} n_{\nu}. \end{aligned} \tag{1.49}$$

The function of this is to project any spacetime tensor purely into the spatial hypersurface by eliminating any time components. Therefore, for a general tensor $X^a{}_b$, the spatial version $\mathcal{X}^i{}_j$, is found by projecting each index of the full spacetime tensor with the projection operator

$$\gamma^i{}_a \gamma^b{}_j X^a{}_b = \mathcal{X}^i{}_j \,. \tag{1.50}$$

The projection operator, when applied to the normal vector, returns zero as it has no components which lie in on the surface of the spatial slice

$$\gamma_{\mu}{}^{a} n^{\mu} = 0. \tag{1.51}$$

It also obeys

$$\gamma^a{}_c \gamma^c{}_b = \gamma^a{}_b. \tag{1.52}$$

This projection operator also acts on covariant derivatives, turning them from their spacetime equivalents into purely spatial versions. Consider a covariant derivative acting on a spatial tensor $\mathcal{X}^i{}_j$. The spatial covariant derivative is found as follows:

$$\gamma^a{}_i \gamma^j{}_b \gamma^c{}_k \nabla_a \mathcal{X}^b{}_c = D_i \mathcal{X}^j{}_k \,. \tag{1.53}$$

Note how all of the indices of both the covariant derivative and the tensor itself have to be projected over. Using these rules of projection, we can write a general decomposition of any tensor X_{ab} into a sum consisting of its individual spatial contributions and the normal vector. We can decompose X_{ab} into

$$X_{ab} = \mathcal{X}_{ab} + n_a \bar{\mathcal{X}}_b + n_b \bar{\mathcal{X}}_a + n_a n_b \hat{\mathcal{X}}. \tag{1.54}$$

Here $\mathcal{X}_{ab}$,$\bar{\mathcal{X}}_a$, and $\hat{\mathcal{X}}$ are the spatial decomposition of the four-dimensional tensor into its three-dimensional fields. These individual components can be recovered with applying the appropriate combination of projection operators or normal vectors as for any spatial field $\bar{\mathcal{X}}_a$, $n^a \bar{\mathcal{X}}_a = 0$.

We can now consider what the metric looks like on a single slice. We find it by applying the same procedure as we would to any other tensor - by projecting its indices with the projection operator. We find

$$\begin{aligned} \gamma^a{}_i \gamma^b{}_j g_{ab} &= \gamma_{ib} \gamma^b{}_j \\ &= \gamma_{ij} \end{aligned} \tag{1.55}$$

Therefore, the spatial metric is simply the projection operator with one of its indices lowered. Following from Equation (1.49) we can express the spatial metric as

$$\gamma_{ab} = g_{ab} + n_a n_b. \tag{1.56}$$

As was the case with the spacetime metric, the spatial metric is used to measure distances on each individual hypersurface.

There is one more key geometric quantity which we need to define, which is the extrinsic curvature K_{ab}. The measures the difference in the normal vector as it moves from point to point along a hypersurface. It is defined as

$$K_{ab} = -\gamma_a{}^c \gamma_b{}^d \nabla_c n_d. \tag{1.57}$$

As can be seen, it is symmetric. Expanding this, we see that

$$\begin{aligned} K_{ab} &= -\gamma_a{}^c \gamma_b{}^d \nabla_c n_d \\ &= -\left(\delta_a{}^c + n_a n^c\right)\left(\delta_b{}^d + n_b n^d\right)\nabla_c n_d \\ &= -\left(\delta_a{}^c + n_a n^c\right)\delta^d{}_b \nabla_c n_d \\ &= -\nabla_a n_b - n_a D_b \ln\alpha, \end{aligned} \tag{1.58}$$

where we have used the identities $n^d \nabla_c n_d = 0$ and $D_a \ln\alpha = n^b \nabla_b n_a$. We can also define the extrinsic curvature in terms of Lie derivatives. We first examine the Lie derivative of the spatial metric along n^a

$$\mathcal{L}_n \gamma_{ab} = n^c \nabla_c \gamma_{ab} + \gamma_{cb} \nabla_a n^c + \gamma_{ac} \nabla_b n^c \tag{1.59}$$

We can rearrange Equation (1.58) to find that $\nabla_a n_b = -K_{ab} - n_a n^c \nabla_c n_b$. Substituting this in, as well as using Equation (1.56)

$$\begin{aligned} \mathcal{L}_n \gamma_{ab} &= n^c \nabla_c \gamma_{ab} - 2K_{ab} - n_a n^c \nabla_c n_b - n_b n^c \nabla_c n_a \\ &= n^c \left(n_a \nabla_b + n_b \nabla_a\right) - 2K_{ab} - n_a n^c \nabla_c n_b - n_b n^c \nabla_c n_a \\ &= -2K_{ab}. \end{aligned} \tag{1.60}$$

Therefore, we find

$$K_{ij} = -\frac{1}{2}\mathcal{L}_n \gamma_{ij}, \tag{1.61}$$

which measures the rate of deformation of the spatial metric along the flow of the normal vector, and is fully equivalent to Equation (1.58).

1.4.2.1 The Gauss, Codazzi, and Ricci Equations

This foliation of spacetime is fundamentally an embedding of three-dimensional space into four-dimensional space. As a result, there are certain relations between the two spaces which hold in order to ensure that this embedding correct. We then expect there to be three-dimensional counterparts to things such as the Riemann curvature tensor and all of its associated contractions, and all other geometric objects. We denote the three-dimensional Riemann tensor with ${}^{(3)}R$. As with

Equation (1.54), we find these three-dimensional versions by applying on the four-dimensional version all the different combinations of the projection operator and normal vector. The first projection of the Riemann tensor is Gauss' equation

$$\gamma_a{}^p\gamma_b{}^q\gamma_c{}^r\gamma_d{}^s R_{pqrs} = {}^{(3)}R_{abcd} + K_{ac}K_{bd} - K_{ad}K_{bc}. \tag{1.62}$$

The next one is the Codazzi equation, which relates the Riemann tensor to the spatial covariant derivatives of the extrinsic curvature:

$$\gamma_a{}^p\gamma_b{}^q\gamma_c{}^r n^s R_{pqrs} = D_b K_{ac} - D_a K_{bc} \tag{1.63}$$

The last one is Ricci's equation, which relates the Riemann tensor to the Lie derivative of the extrinsic curvature along the normal vector, which is semi-equivalent to its time derivative:

$$n^d n^c \gamma_a{}^q\gamma_b{}^r R_{drcq} = \mathcal{L}_n K_{ab} + \frac{1}{\alpha} D_a D_b \alpha + K^c{}_b K_{ac} \tag{1.64}$$

The final key component that we need is the spatial version of the stress energy tensor which appears on the right hand side of Equation (1.13). Using the general decomposition of a tensor as in Equation (1.54), we write the stress energy tensor as:

$$T_{ab} = S_{ab} + n_a S_b + n_b S_a + n_a n_b \rho \tag{1.65}$$

Where we define S_{ab} to be the spatial stress, S_a to be the momentum density, and ρ to be the total energy density. With these definitions, we can now substitute Equations (1.62, 1.63, 1.64) into Equation (1.13) to find a series of constraints, and the evolution equation for the extrinsic curvature.

We need now to distinguish constraint equations from evolution equations. An equation of motion is characterised by second order time derivatives of the field variable - constraint equations therefore contain at most first order time derivatives of the field. For the above, we have the dynamical variables of the field γ_{ab} and the extrinsic curvature K_{ab} which is related to the first time derivative of the spatial metric through Equation (1.64). Performing the above substitutions with Equations (1.62, 1.63, 1.64) and (1.13), we find the Hamiltonian constraint

$$16\pi\rho = {}^{(3)}R + K^2 - K_{ab}K^{ab}, \tag{1.66}$$

and the Momentum constraint

$$8\pi S_a = D_b K^b{}_a - D_a K. \tag{1.67}$$

Collectively, Equations (1.66, 1.67) relate the spatial components of the Riemann tensor to the matter source directly. A necessary condition for embedding our hypersurfaces into four-dimensional space along with the field data is to obey these two equations. Firstly, we write the time vector, or coordinate lines as

$$t^a = \alpha n^a + \beta^a. \tag{1.68}$$

β^a is known as the shift vector, and is related to our freedom to relabel coordinates from slice to slice. We can now rewrite Equation (1.61)

$$\mathcal{L}_t \gamma_{ab} = \mathcal{L}_\beta \gamma_{ab} - 2\alpha K_{ab}, \tag{1.69}$$

where we use $\alpha \mathcal{L}_n K_{ab} = \mathcal{L}_t K_{ab} - \mathcal{L}_\beta K_{ab}$ which follows from the definition of the Lie derivative. From Equation (1.64), one can find the evolution for the extrinsic curvature

$$\begin{aligned} \mathcal{L}_t K_{ab} = \mathcal{L}_\beta K_{ab} - D_a D_b \alpha + \alpha \left({}^{(3)}R_{ab} - 2K_{ac}K^c{}_b + K K_{ab} \right) \\ -8\pi\alpha \left(S_{ab} - \tfrac{1}{2}\gamma_{ab}\left(S - \rho\right) \right). \end{aligned} \tag{1.70}$$

Together, Equations (1.69) and (1.70) are the covariant foliated equations of motion for the spatial metric.

1.4.2.2 Basis Equations

We can now examine in more detail how to map coordinates on to the spatial hypersurfaces by relating the equations of motion we have found to the time vector t^a. As with general relativity, in numerical relativity we have the freedom to choose whichever coordinate system we want. In general relativity, this is related through the four degrees of freedom we have in coordinate transformations. In this particular foliation, we can do the same thing with the lapse function α and shift vector β^i. We saw the lapse function appear before in Equation (1.46) as the

normalisation of the time increment equivalent one form ω_a. If we consider these functions as coordinate transformations, then the lapse embodies our freedom to choose the rate of progression of the local time coordinate on each slice, and the shift vector to transform and relabel the spatial coordinates. n^a is inappropriate for a choice of time coordinate as it has the incorrect normalisation. This is why we instead have the time vector as defined in Equation (1.68) that contains the lapse and shift. The scalar product of t^a with $\nabla_a t$ is unity, which makes it a suitable vector along which we can take derivatives of the spatial metric. To make more geometric sense of the lapse and shift, consider Figure 1.4. Figure 1.4 shows two

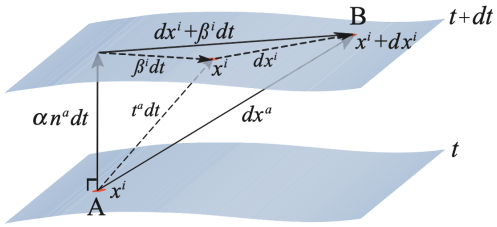


Figure 1.4: The spacetime interval $\mathrm{d}x^a$ between two events A and B. Each event is on separate time slices $\mathrm{d}t$ apart. The interval is expressed by first the time-like interval $t^a \mathrm{d}t$ which is then corrected by $\mathrm{d}x^i$. Written fully, the interval is $\mathrm{d}x^a = (\alpha n^a + \beta^i)\,\mathrm{d}t + \mathrm{d}x^i$. Figure from Baumgarte and Shapiro, 2010.

adjacent hypersurfaces with the events A and B. Here, we can more clearly see how the vector t^a maps the coordinate x^i on Σ_t to the same coordinate x^i on $\Sigma_{t+\mathrm{d}t}$. However, the presence of the shift vector β^i has relabelled this coordinate to $x^i + \mathrm{d}x^i$. Therefore, the full increment $\mathrm{d}x^a = (\alpha n^a + \beta^i)\,\mathrm{d}t$

Using the lapse and shift, and the properties of spatial tensors, we can rewrite the Hamiltonian and Momentum constraints, the Lie derivative of the metric γ_{ij} along n^a, and Ricci's equation to find the evolution equations for spacetime in a 3+1 decomposed form. They are referred to as the 'ADM' equations after Arnowitt, Deser, and Misner (Arnowitt, Deser, and Misner, 1962). The first time derivative of the spatial metric in these specific, time vector adapted coordinates is

$$\partial_t \gamma_{ij} = -2\alpha K_{ij} + D_i \beta_j + D_j \beta_i. \tag{1.71}$$

The first time derivative for the extrinsic curvature found from Ricci's equation is:

$$\partial_t K_{ij} = -D_i D_j \alpha + \alpha \left({}^{(3)}R_{ij} - 2K_{ik}K^k{}_j + K K_{ij} \right) - 8\pi\alpha \left(S_{ij} - \tfrac{1}{2}\gamma_{ij} \left(S - \rho \right) \right) + \beta^k D_k K_{ij} + K_{ik} D_j \beta^k + K_{kj} D_i \beta^k. \tag{1.72}$$

Then lastly, the two constraint equations are:

$$16\pi\rho = {}^{(3)}R + K^2 + K_{ij}K^{ij}, \tag{1.73}$$

and

$$8\pi S^i = D_j \left(K^{ij} - \gamma^{ij} K \right). \tag{1.74}$$

In all, Equations (1.71, 1.72, 1.73, 1.74) represent the system of ADM equations dictating the evolution of the spatial metric, and are fully equivalent to the Einstein field equations in Equation (1.13). An important aspect to notice here is that through the introduction of the extrinsic curvature, we have split Equation (1.13) into two first-order in time equations from a single second order in time equation. In this way, we can identify the extrinsic curvature as a canonical momentum for the spatial metric. In theory, we can take these equations, construct initial data which obeys the constraints, and then numerically integrate this system to run a numerical relativity simulation. Unfortunately, the ADM equations are insufficient for this purpose and instead are unstable, so when being integrated, would lead to a large accumulation of numerical error which would likely crash the simulation.

To understand this, we return to the idea of well-posedness and the related concept of hyperbolicity. Hyperbolic differential equations are written in the form

$$\partial_t \mathbf{u} + \mathbf{A}^i \cdot \partial_i \mathbf{u} = S, \tag{1.75}$$

Where $\mathbf{u}(t, x^i)$ is the solution vector, A^i is the 'velocity matrix', or matrix of prefactors for the spatial derivatives, and $\mathbf{S}(u)$ is the source vector. Recall the condition for well-posedness from Equation (1.45) which stated

$$||\mathbf{u}(t, x^i)|| \leq k e^{\alpha t} ||\mathbf{u}(0, x^i)||, \tag{1.76}$$

therefore demanding that the solution cannot have modes which grow faster than exponentially in time. This is the condition which the ADM system fails and so makes it an unsuitable set of equations. To guarantee Equation (1.76), the solution to Equation (1.75) needs to be either symmetric hyperbolic or strongly hyperbolic, as opposed to weakly hyperbolic. Consider an arbitrary unit vector v^i and then the following matrix

$$\mathbf{P} = \mathbf{A}^i v_i. \tag{1.77}$$

$\mathbf{P}$ is known as the principal symbol, and depending on its properties, the system has varying types of hyperbolicity. If $\mathbf{P}$ can be symmetrised independently of v^i, then there is symmetric hyperbolicity. If for all v^i , $\mathbf{P}$ has real eigenvalues and a complete set of eigenvectors then there is strong hyperbolicity else for an incomplete set of eigenvectors there is only weak hyperbolicity. Equation (1.76) does not hold for weakly hyperbolic systems, and therefore they are not well-posed. Evidently, we seek systems of equations to evolve spacetime which are either symmetric or strongly hyperbolic.

1.4.2.3 The BSSN System

To address this fundamental issue of being well-posed, a series of works in the 1990s lead to the development of the BSSN system, named after the initials of the authors (Shibata and Nakamura, 1995; Baumgarte and Shapiro, 1998). Part of the issue with the ADM system is the mixed spatial derivatives of the metric, which means the system is only weakly hyperbolic and so not well-posed. These mixed derivatives of the form $\partial^k \partial_l \gamma_{ij}$ 'hide' in the spatial Ricci tensor. This can be seen if we expand the Ricci tensor out in terms of the spatial metric and Christoffel symbols

$${}^{(3)}R_{ij} = \frac{1}{2}\gamma^{kl}\left(\partial_l\partial_i\gamma_{kj} + \partial_j\partial_k\gamma_{il} - \partial_j\partial_i\gamma_{kl} - \partial_l\partial_k\gamma_{ij}\right) + \gamma^{kl}\left(\Gamma^m{}_{il}\Gamma_{mkj} - \Gamma^m{}_{ij}\Gamma_{mkl}\right). \tag{1.78}$$

Here, all the Christoffel connections are their three-dimensional spatial counterparts. Therefore, we must try and seek a way to eliminate these problematic terms. Part

of the idea of the BSSN formulation is to promote the contraction of the Christoffel symbol with the spatial metric to a new auxiliary variable. This is defined as[7]

$$\Gamma^i \equiv \gamma^{jk}\Gamma^i{}_{jk} = -\partial_j \gamma^{ij}. \tag{1.79}$$

By substituting this in to the definition of the Ricci tensor in Equation (1.78), one finds

$${}^{(3)}\tilde{R}_{ij} = -\frac{1}{2}\gamma^{lm}\partial_m\partial_l\gamma_{ij} + \gamma_{k(i}\partial_{j)}\Gamma^k\Gamma_{(ij)k} + \gamma^{lm}\left(2\Gamma^k{}_{l(i}\Gamma_{j)km} + \Gamma^k{}_{im}\Gamma_{klj}\right), \tag{1.80}$$

where the brackets in the indices denote symmetrised indices, for example, $T_{(ij)} = (1/2)\left(T_{ij} + T_{ji}\right)$. Observe how in Equation (1.80) there are now no explicit second order derivatives of the spatial metric apart from the first term which is simply the Laplacian and so is not a mixed second order derivative. As Γ^i has been promoted to an auxiliary variable, it has its own evolution equation in the BSSN system. The full system of equations is given in Appendix A.1.

1.4.2.4 Beyond BSSN - Z4 and CCZ4

There are many different schemes in numerical relativity, each with different advantages and disadvantages. The one I discuss in this section is the system which is used in the numerical relativity codes that I use - GRChombo and GRDzhadzha - covered in Section 1.5.

As mentioned, the ADM system of equations are only weakly hyperbolic which leads to ill-posedness and so the introduction of numerical errors which prevent simulation. An additional problem with ADM is that the ill-posedness allows any variety of mode to grow faster than exponentially, not just errors. While there may be physical phenomena occurring in a simulation which match this behaviour, this will ultimately cause the simulation to be short lived. ADM can be improved upon however by making some informed choices. Simulations run using the ADM system from Equations (1.71, 1.72, 1.73, 1.74) are known as 'unconstrained evolution'. The physical correctness of a simulation is dependent on the constraint equations being

[7] In the BSSN formalism, these are all conformally related objects to their originals but for the sake of consistency in notation for this argument, I have omitted this.

satisfied, but any violations of the constraints themselves are not fed back into the evolution to inform it of a path to take which reduces the amount of violations. If we had access to some hypothetical perfect simulation, then this would be true at all times and we could use the ADM system. However, due to innate inaccuracy with solving systems of differential equations using finite differencing methods, no matter however small, numerical errors which violate these constraints accumulate. When the constraints become violated, then we can no longer be guaranteed that the evolution of the system represents a physically possible worldline. We can approach this problem by considering coordinate transformations and covariance. In full four-dimensional general relativity, we have the freedom of general covariance, meaning the physics we simulate is invariant under a smooth coordinate transformation with any of the space and time coordinates. When we decompose the system into Equations (1.71, 1.72, 1.73, 1.74), we inadvertently now run the risk of breaking this covariance. As Bona et al., 2003 discusses, when we consider unconstrained evolution, we only use Equations (1.71, and 1.72), equivalent to the spatial components of the Einstein field equations in Equation (1.13). Therefore, as we only consider the spatial components, we are limited in the freedom we have to transform the coordinates. We can only make transformations which preserve the foliations in time, as these are no longer evolving with respect to the changes in spatial geometry. This means general covariance has been broken and so need a way to incorporate the two constraint equations into the evolution equations in order to restore it.

The method proposed by Bona et al., 2003 is by upgrading the constraint equations into full evolution equations for a new dynamical variable Z_a. This is decomposed into spatial components as follows:

$$Z_a = Z_i + n_a \hat{Z} \tag{1.81}$$

The components of this four-vector represents the violations in the Hamiltonian and momentum constraints respectively. For a system which is perfectly obeying the constraint equations and therefore which solves the Einstein field equations

has $Z_a = 0$. The Einstein field equations become:

$$R_{ab} + \nabla_a Z_b + \nabla_b Z_a = 8\pi \left(T_{ab} - \frac{1}{2} T g_{ab} \right) \tag{1.82}$$

This kind of formulation is known as constraint damping. The motivation behind promoting the constraints into dynamical variables is that they can help to correct the evolution of the system and control any sources of error as they emerge. The Einstein field equations are solved when the constraint four-vector is zero. Therefore, as errors arise, the four-vector obtains non-zero components. The evolution equations for the spatial metric and extrinsic curvature receive modifications with different permutations of Z_a and so effectively receive corrections from the constraint vector with the aim of reducing the components of Z_a back to zero. The modified evolution equations are

$$\left(\partial_t - \mathcal{L}_\beta \right) \gamma_{ij} = -2\alpha K_{ij} \,, \tag{1.83}$$

and

$$\left(\partial_t - \mathcal{L}_\beta \right) K_{ij} = -\nabla_i \alpha_j + \alpha \left({}^{(3)}R_{ij} + \nabla_i Z_j + \nabla_j Z_i - 2K_{ij} K^{ij} + \left(K - 2\hat{Z} \right) K_{ij} \right) . \tag{1.84}$$

The evolution equations for the components of the four vectors themselves are

$$\left(\partial_t - \mathcal{L}_\beta \right) Z_i = \alpha \left(\nabla_k \left(K^k{}_i - \delta^k{}_i K \right) + \partial_i \hat{Z} - \frac{\hat{Z}}{\alpha} \alpha_i - 2K^k{}_i Z_k \right) , \tag{1.85}$$

and

$$\left(\partial_t - \mathcal{L}_\beta \right) \hat{Z} = \frac{\alpha}{2} \left({}^{(3)}R + \left(K - 2\hat{Z} \right) K - K^2 + 2\nabla_k Z^k - \frac{2}{\alpha} \alpha_k Z^k \right) , \tag{1.86}$$

where $\alpha_i \equiv \nabla_i \alpha$. Together, Equations (1.83, 1.84, 1.85, 1.86) represent a Z4 recast form of numerical relativity and are equivalent to the evolution equations found before for the ADM formalism. There are additional multiples of Z_a which can be added, multiplied by factors of constraint damping coefficients - see (Alic et al., 2012) for a full version. Forms of the constraint equations from ADM can be found in Equations (1.85, 1.86) and are fully dynamical, restoring this general covariance. Critically, it is also a strongly hyperbolic system and so is well-posed. There is

a further set of improvements which can be made to Z4. This is the notion of conformality and in tandem with the constraint damping of the Z4 system, becomes known as the CCZ4 system (Alic et al., 2012). This is the system for evolution which I use in my simulations inside of GRChombo. There are various advantages of using a fundamentally conformal system, such as the ability to avoid certain singularities in the metric, and being able to handle imperfect boundary conditions by incurring fewer numerical errors. The full set of CCZ4 equations is found in Appendix A.2.

1.5 GRChombo and GRDzhadzha

1.5.1 GRChombo

GRChombo and GRDzhadzha are the two codes that I use to run the various simulations in this thesis. In Chapters 2, 3 and 4 I use them to investigate a variety of problems, with the unifying factor being that of matter of various types accreting around black holes. These codes are appropriate for the scenarios I wish to investigate, as they allow me to easily implement different models of matter in both fixed-background and dynamic background situations. Firstly, I model the scenario of wave-like scalar field matter accreting around black holes, and the various phenomenology which arises with the introduction of different scalar potentials. As I investigate this ultra-light dark matter, GRDzhadzha is an excellent tool for this case due to the aforementioned ability to decouple diffuse matter from the vacuum background. I then also use GRChombo itself to investigate the same models of dark matter but in the case of BBH mergers. In Chapter 4, I present my work on developing a new formalism for the simulation of spin-2 tensor field dark matter using numerical relativity. Further work has to be done before the full, general version is complete, but tests of this formalism in simplified cases is done using GRDzhadzha.

GRChombo (Andrade et al., 2021) is an open-source numerical relativity code with adaptive mesh refinement features, using fourth-order Runge-Kutta methods to solve partial differential equations. It simulates spacetime in full numerical relativity, using the CCZ4 system as above. It has a focus on flexibility and as such is suitable for simulating a wide range of physical scenarios with the ability

to define custom matter classes. For examples using this code, see Joana and Clesse, 2021 for how inflation is affected by inhomogeneous initial conditions, Aurrekoetxea et al., 2020, which examines how inhomogeneous inflation is affected by different choices of potential for the inflaton field, Andrade, Figueras, and Sperhake, 2022, which investigates how cosmic censorship principles can be violated by collisions of black holes in higher dimensions, Evstafyeva et al., 2023, for studies of general initial conditions and the dynamics for boson star binary mergers of arbitrary mass ratio, and Traykova et al., 2021 for the dynamical friction of scalar dark matter around black holes.

To run a simulation, one must first consider the initial state of spacetime, and then if any matter is present and if so, what class. Then, initial conditions for the spacetime and matter are set such that the constraint equations are satisfied. This is difficult due to the coupled nature of matter and curvature, as changing the shape of spacetime changes the distribution of matter and so on, which makes solving the constraints a challenge. Thankfully, various methods can be used to make this possible. The initial conditions are solved with dedicated multigrid solvers such as in Aurrekoetxea, Clough, and Lim, 2023 and Aurrekoetxea et al., 2025.

1.5.2 Fixed-background Evolution

Whilst powerful, it is often computationally expensive and time-consuming to run these dynamic simulations with sufficient detail and an acceptable amount of numerical error. As such, it is useful to find ways to make the simulation more efficient without compromising on the scientific results. Consider the evolution equations for the spacetime background directly. The spatial metric, its momentum, and the various components into which they are split (Alic et al., 2012) all contribute to the computing time of each timestep. If it was not necessary to simulate the evolution of all these background elements, the simulation would speed up greatly. This can be done by studying a narrower set of physical scenarios where the local curvature scale of matter is much longer than the unperturbed initial spacetime.

As an example, imagine a Schwarzschild black hole in vacuum. When we introduce matter, this contributes additional curvature. As this system evolves, these two initial contributions to curvature become mixed and so inseparable. Before the simulation begins however, one can make a clear separation between the background and the matter. By making the total density of the matter small enough such that its initial contribution to curvature compared to the background is negligible, we can simply neglect this contribution. Now, the background spacetime is fixed and non-evolving and as such we can discard all of the computationally expensive evolution equations associated with it. There will be small errors on the order of the initial background density involved with this method as in nature, any matter does contribute to the curvature of space. The method relies on the fact that these errors are small enough to be neglected, and do not accumulate significantly on the timescales of interest of the problem. For simulating cases such as the accretion of matter onto black holes, the density of matter around the horizon inevitably increases, so checks have to be made that this density does not induce noticeable curvature. We also restrict ourselves to stationary spacetimes with this method, and so cannot simulate scenarios such as binary black hole mergers with highly dynamic spacetimes.

GRDzhadzha (Aurrekoetxea et al., 2024b) is an open-source fixed-background code based on GRChombo (Andrade et al., 2021) which focuses on these scenarios where the matter can be decoupled from the background metric. The power in this lies with the ability to simply set the metric to be some fixed spacetime and then let matter freely evolve on top of this background. This is not numerical relativity, as we abandon the idea of evolving spacetime, and instead is a way to simulate the behaviour of matter in relativistic scenarios. As a result, it is more computationally efficient than numerical relativity. One chooses the vacuum spacetime of interest, then finds the initial conditions for the matter on the initial hypersurface by solving the constraint equations for the matter - see Chapter 4 for a discussion on this. The evolution of the matter is then fully described and avoids the difficulties which arise when considering a dynamic background. There have been many different

applications of this software so far including: the accretion of scalar hair around black holes (Clough, Ferreira, and Lagos, 2019, Bamber et al., 2021), the dynamical friction of ULDM around black holes (Traykova et al., 2021), and superradiance in massive vector fields (Clough et al., 2022, Wang et al., 2022).

"No, I don't like work. I had rather laze about and think of all the fine things that can be done. I don't like work—no man does—but I like what is in the work—the chance to find yourself. Your own reality—for yourself, not for others—what no other man can ever know. They can only see the mere show, and never can tell what it really means."

— Joseph Conrad
Heart of Darkness

2

Self-Interacting Scalar Dark Matter around Binary Black Holes

2.1 Motivation

In this chapter, I will cover the work I have done as part of a team of collaborators on ultra-light self-interacting scalar fields and different phenomena which occur during accretion processes around black holes. This is published work, as in Aurrekoetxea et al., 2024c. In this project, I helped to develop our understanding of the behaviour of the scalar field, and ran the various simulations used to produce the results. Additionally, I produced many of the plots which were used in discussions to understand the results we had seen.

As per Section 1.3, there is a great motivation to study different ULDM models, and in this case, wave-like dark matter candidates, such that we can test their properties and investigate the various effects and behaviours we observe when these matter candidates are subjected to different environments. One of the ultimate goals of this field is to assess the validity of these models, and so their possibility of existing in the universe. Black holes can act as an excellent laboratory for this type of study, through accretion being an effective way to increase the density of these candidates from their initial, very sparse cosmological densities to very high values.

As the dark matter reaches larger energy scales, then the different phenomena which arise due to their different physical properties become more pronounced.

In this specific case, we are interested in self-interacting ultra-light dark matter models, which modifies the 'usual' quadratic $\sim m^2\phi^2$ potential with an additional quartic term, coupled by an interaction strength parameter. At low, cosmological densities, the overall matter field is not very energetic, and so only explores regions of its potential which are close to the initial minimum. As the density increases, the field becomes more energetic however, and can explore further reaches of the potential. To visualise this, imagine a plot of potential versus value of the field, with the minimum of the potential centred at zero. As the field increases its value, it shifts away from zero, and so reaches further and further parts of the potential. In the specific case of a quadratic potential with additional quartic terms, for low values of the field, the quadratic terms dominate and so the overall shape of the potential is quadratic. Further away from the minimum, and therefore at higher energies, the quartic terms become more significant and eventually dominate.

The premise for using black holes to study self-interacting dark matter models is that accretion is a useful pathway to increasing the density of dark matter from its initial diffuse state to energies where the non-quadratic sections of the potential begin to affect the behaviour and phenomenology we observe. In this chapter, I explain how we use numerical methods to simulate clouds of self-interacting dark matter undergoing accretion in order to investigate the behaviours of the field when it reaches these interesting regions of the potential.

2.2 Introduction

In the absence of observations of weakly interacting massive particles (WIMPs) (Aalbers et al., 2023), light scalar fields like axions have undergone a resurgence as potential candidates for the dark matter (DM) of the Universe (Schive, Chiueh, and Broadhurst, 2014) (see Hui, 2021; Ureña-López, 2019; Niemeyer, 2019 for reviews). Such light candidates exhibit distinctive signatures on astrophysical scales, potentially influencing the growth of cosmic structure, the cores of galaxies and the

environments of compact objects like neutron stars and black holes (BHs). In the last case, which is the focus of this chapter, detecting the effects of the environment on the gravitational wave signal from merging sources offers one observational possibility (Barack et al., 2019; Barausse et al., 2020; Afshordi et al., 2023; Caneva Santoro et al., 2024; Cardoso and Maselli, 2020; Barausse, Cardoso, and Pani, 2014; Yunes et al., 2011; Kocsis, Yunes, and Loeb, 2011; Macedo et al., 2013; Cardoso and Macedo, 2020; Bertone and Tait, 2018; Alves Batista et al., 2021; Zwick et al., 2022; Cardoso and Duque, 2020; Maselli et al., 2022; Amaro-Seoane, 2018; Cardoso et al., 2022; Cole et al., 2023a; Krolak and Schutz, 1987; Koo et al., 2024; Bošković, Koschnitzke, and Porto, 2024; Karydas, Kavanagh, and Bertone, 2024; Tomaselli, Spieksma, and Bertone, 2024b; Tomaselli, Spieksma, and Bertone, 2024a).

Around spinning BHs, the density of scalar fields can grow through the superradiant instability – extracting energy and angular momentum from the BH (Zel'Dovich, 1971b; Press and Teukolsky, 1972; Zouros and Eardley, 1979; Detweiler, 1980; Cardoso et al., 2004; East and Pretorius, 2017) (see Brito, Cardoso, and Pani, 2015 for a review). However, in the non spinning Schwarzschild case these fields can also undergo more mundane processes like accretion, where scalar fields are drawn into the deep gravitational wells of the BH (Clough, Ferreira, and Lagos, 2019; Hui et al., 2019; Bamber et al., 2021; Bucciotti and Trincherini, 2023; de Cesare and Oliveri, 2023; Sanchis-Gual et al., 2016). For a minimally coupled field obeying the Klein-Gordon equation, accretion leads to the accumulation of a density profile around the BH, with overdensities akin to the "spikes" of heavy particle DM candidates (Gondolo and Silk, 1999; De Luca and Khoury, 2023; Berezhiani et al., 2024; Sadeghian, Ferrer, and Will, 2013; Gnedin and Primack, 2004; Merritt, Harfst, and Bertone, 2007; Merritt, 2004; Shapiro and Heggie, 2022). Unlike in the particle case, if the Compton wavelength of the scalar field is close to the horizon radius of the BH, the wave-like nature of the scalar field manifests. In the case of solar mass or supermassive BHs, this corresponds to scalar field masses $m \approx 10^{-11}\,\mathrm{eV}$ and $m \approx 10^{-17}\,\mathrm{eV}$, respectively.

These differences change the impact of wave-like and particle-like candidates on gravitational waves emitted from binary black holes (BBHs). In the case of equal-mass mergers, previous work has indicated that the motion of the binary disrupts particle DM spikes, and thus has little or no effect on the gravitational wave signal near merger (Merritt and Milosavljevic, 2002; Bertone and Merritt, 2005; Kavanagh, Gaggero, and Bertone, 2018; Cole et al., 2023b). Hence, the focus is on extreme/intermediate mass ratio inspirals (EMRIs/IMRIs), where the smaller secondary object does not disrupt the spike of the more massive primary BH. For scalar DM, on the other hand, it is shown in Aurrekoetxea et al., 2024a; Bamber et al., 2023 (see also Ficarra, 2021; Zhang et al., 2023; Choudhary et al., 2021; Yang et al., 2018) that scalar accretion onto equal-mass BHs creates an overdensity between them, which persists during the binary merger. This leads to a faster orbital decay (and hence dephasing of the gravitational-wave signal), is maximized when the Compton wavelength of the scalar field $\lambda_c = 2\pi/\mu$ (where $\mu = mc/\hbar$) is of the order of the binary's orbital separation.

Much of our understanding of scalar field DM is based on the simplest model – a massive scalar field with potential $\mu^2\phi^2$. This approach mirrors the study of particle DM, where most research has focused on non-interacting, perfectly cold DM. As cosmological and astrophysical data have improved, interest has grown in more complex particle DM models that include multiple species, warm initial conditions, and self-interactions (Bertone and Tait, 2018). Self-interactions can significantly affect galaxy formation, transforming a cusped density profile into a cored profile, and have recently been proposed as a solution to the final parsec problem in the particle case (Alonso-Álvarez, Cline, and Dewar, 2024; Fischer and Sagunski, 2024). Whilst the impact of interactions will be small at average galactic DM densities, they may play a larger role at higher densities if DM accumulates, e.g. around stars or BHs (Budker et al., 2023; Shapiro and Paschalidis, 2014; Berezhiani et al., 2024; Kadota et al., 2024; Alonso-Álvarez, Cline, and Dewar, 2024; Boudon et al., 2024; Feng et al., 2022; Alvarez and Yu, 2021; Chia et al., 2023; Spieksma et al., 2023; Siemonsen et al., 2023; Cannizzaro et al., 2022; Boskovic

et al., 2019; Marsden et al., 2024; Khlopov et al., 1985). In the case of scalar DM, self-interactions enter as higher order terms in the potential, so a quartic term $\lambda\phi^4$ is a natural extension that preserves the parity symmetry. The coupling λ parameterises the strength of the self-interactions, with its sign indicating whether they are repulsive or attractive. This type of coupling provides the leading order term for DM with self-interactions, like those expected in the axion potential. Self-interacting scalar fields have been studied in the context of superradiance around isolated BHs, where it was proposed that attractive interactions could lead to rich and unique phenomenology, in particular *bosenova* explosions in which the cloud is radiated and absorbed into the BH (Roberts et al., 2001; Arvanitaki and Dubovsky, 2011; Yoshino and Kodama, 2012; Yoshino and Kodama, 2015). However, more recent work has shown that in the scalar case the bosenova is unlikely to be reached due to superradiance alone, as the growth saturates when higher modes are excited (Omiya et al., 2024; Omiya et al., 2023; Omiya, Takahashi, and Tanaka, 2022; Omiya, Takahashi, and Tanaka, 2021; Baryakhtar et al., 2021). Additional accretion may enhance the rate sufficiently to allow the instability to take hold (Hui et al., 2023), and it may play a role in dynamical capture around stars (Budker et al., 2023) or the higher densities of boson stars (Arakawa et al., 2024; Arakawa et al., 2023; Eby and Takhistov, 2024). Vector bosons are more promising and it has been shown numerically that vector fields with a Higgs-like mass mechanism can excite stringy bosenova explosions for sufficiently strong couplings (East and Huang, 2022; East, 2022), and tensors should in principle be even more explosive, although the models suffer from some pathologies (East and Siemonsen, 2023).

In this chapter, we use numerical simulations to study the accretion of self-interacting scalar fields onto BHs. First, we describe the setup and chosen model in Sec. 2.3. In Sec. 2.4, the evolution of DM near an isolated BH is studied, which provides information about the effect self-interactions have on the spike of the primary BH of an EMRI system, and highlights the possibility of achieving a bosenova-like explosion via accretion. In Sec. 2.5, numerical relativity simulations are used to study the growth of self-interacting scalar clouds during an equal-mass

BH merger, and quantify the impact these clouds have on the BBH by extracting the gravitational-wave signal during the inspiral, merger and ringdown. The results are summarised in Sec. 2.6. as well as comments on the physical relevance of the findings.

2.3 Scalar field dark matter model

We model DM as a minimally coupled complex scalar field Φ described by the action

$$S = \int \mathrm{d}^4x\sqrt{-g}\left(\frac{R}{16\pi G} - \frac{1}{2}\left(\nabla_\alpha\Phi\right)^*\left(\nabla^\alpha\Phi\right) - V(\Phi)\right), \tag{2.1}$$

In particular, we focus on the impact of self-interactions in the DM field by adding a quartic self-interacting term

$$V(|\Phi|) = \frac{\mu^2}{2}|\Phi|^2 + \frac{\lambda}{4}|\Phi|^4, \tag{2.2}$$

where λ is a real, dimensionful (in geometric units) coupling constant[1] that parameterises the strength of the self-interactions. The sign of λ specifies whether the self-interactions are repulsive ($\lambda > 0$) or attractive ($\lambda < 0$). If $\lambda > 0$, the potential becomes steeper for larger values of the field, which suppresses growth in the field. For $\lambda < 0$ on the other hand, the potential opens up asymptotically, making it easier to explore larger values. However, purely attractive couplings result in a potential that is unbounded from below for sufficiently large values of the field $|\Phi|$. To avoid possible issues when studying attractive self-interactions, we instead simulate

$$\begin{aligned} V(\Phi) &= \frac{\mu^4}{2\lambda}\left(\exp\left[\frac{\lambda}{\mu^2}|\Phi|^2\right] - 1\right) \\ &\approx \frac{\mu^2}{2}|\Phi|^2 + \frac{\lambda}{4}|\Phi|^4 + \mathcal{O}(|\Phi|^6), \end{aligned} \tag{2.3}$$

which approximates the quartic potential near the minimum but reaches a plateau rather than turning over after the maximum. Figure 2.1 illustrates the shape of this potential.

In the flat-space, homogeneous limit, and in the absence of self-interactions, modelling the DM with a complex scalar field allows one to obtain a stationary

[1]The quantity λ has units of M^{-2} in geometric units. We denote the dimensionless value as $\bar{\lambda}$, see Sec. 2.6 for more details on the conversion.

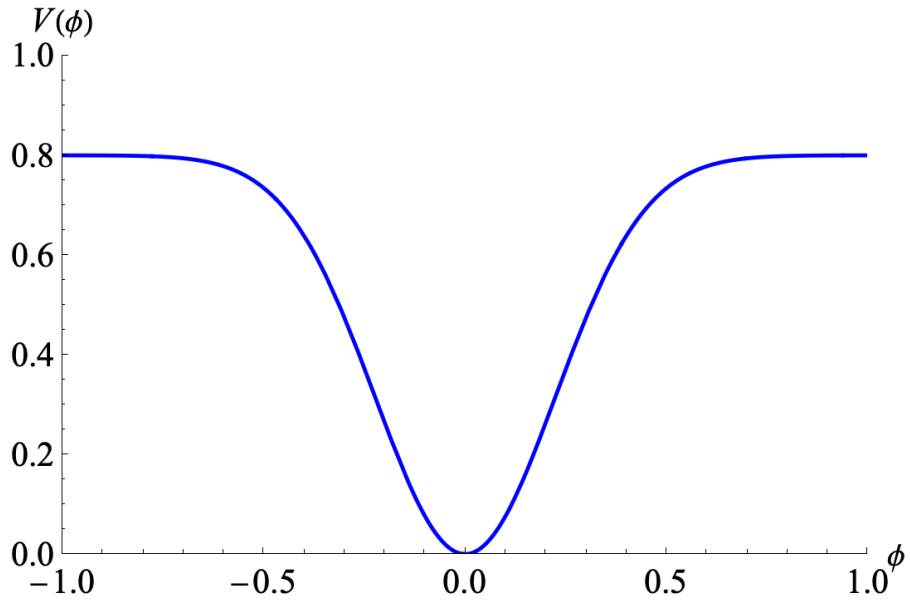


Figure 2.1: Shape of the potential as described by Equation (2.3). Before the turnover, the potential behaves as an attractive quartic potential. Beyond the turnovers however, the potential plateaus instead of then decreasing to an unbounded value in order to prevent simulations from crashing.

density[2]. The Noether current associated with the U(1) symmetry of the system corresponds to particle number conservation, making the DM stable. On the complex plane, where the scalar field is defined, the behaviour is that of an ellipse with semi-axis and orientation set by the initial conditions. Homogeneous initial conditions are chosen $\Phi = (\mathrm{Re}[\Phi], \mathrm{Im}[\Phi])$ such that

$$\Phi_0 = (\phi_0, 0)\,, \qquad \partial_t \Phi_0 = (0, \mu\phi_0)\,. \tag{2.4}$$

Then, although the asymptotic value of the fields oscillates ($\Phi \sim \exp[imt]$), the modulus $|\Phi(t)|$ remains constant throughout its evolution and the scalar field tracks circular orbits on the complex plane. This behaviour leads to a constant asymptotic energy density $\rho(t) = \rho_0$, with the magnitude determined by the initial conditions

$$\rho_0 = \mu^2\phi_0^2 + \frac{\lambda}{4}\phi_0^4\,. \tag{2.5}$$

The values of ϕ_0 and λ are chosen so that the self-interaction term is initially small ($\mu^2 \gg \lambda\phi_0^2$) and $\rho_0 \approx \mu^2\phi_0^2$.

[2]Massive, self-interacting complex scalar fields play a fundamental role in describing the behaviour of superfluid (zero viscosity) DM (Berezhiani and Khoury, 2015; Berezhiani, Elder, and Khoury, 2019; Berezhiani et al., 2024).

The dynamics of the scalar field is given by the Klein-Gordon equation

$$\nabla^{\alpha}\nabla_{\alpha}\Phi - \frac{\partial V(|\Phi|)}{\partial \Phi^{*}} = 0\,, \tag{2.6}$$

where ∇_{μ} is the covariant derivative operator associated to the metric $g_{\alpha\beta}$. In the first part of this chapter, we focus on solving this equation on a fixed Schwarzschild background, so that the metric $g_{\alpha\beta}$ does not evolve. In the second part, we use numerical relativity to solve the coupled system of the Einstein-Klein-Gordon equations to evolve both the scalar field and the spacetime metric for the case of an equal-mass binary merger.

2.4 Dark matter around an isolated black hole

During an extreme-mass-ratio inspiral, a stellar-mass BH emits gravitational waves as it orbits around a supermassive BH. Given the separation of scales, the smaller BH can be treated as a perturber of the primary BH's spacetime. If the primary has a DM environment, then as the secondary object moves through it, its geodesic motion will deviate from the vacuum case, and this, combined with effects like dynamical friction and accretion, may leave distinctive imprints in the gravitational-wave signal. These signatures are one of the key targets of the Laser Interferometer Space Antenna (Boudon et al., 2024; Bošković, Koschnitzke, and Porto, 2024; Cole et al., 2023a; Maselli et al., 2022; Zwick et al., 2022; Macedo et al., 2013; Barausse, Cardoso, and Pani, 2014; Cardoso and Maselli, 2020). However, characterizing these signatures requires a robust theoretical understanding of the expected environment. Motivated by this, we investigate the DM overdensity that forms around an isolated BH for different self-interactions, neglecting the backreaction of the DM onto the spacetime of the BH. Specifically, we use GRDzhadzha (Aurrekoetxea et al., 2024b) to solve the Klein Gordon equation on a BH background in Cartesian Kerr–Schild coordinates (Visser, 2007)

$$ds^2 = \left(\eta_{\mu\nu} + \frac{2M}{r} l_{\mu} l_{\nu}\right) \mathrm{d}x^{\mu}\mathrm{d}x^{\nu}\,, \tag{2.7}$$

where $\eta_{\mu\nu} = \text{diag}(-1, 1, 1, 1)$, M is the BH mass, and $l_\mu = (1,\, x/r,\, y/r,\, z/r)$ is the ingoing null vector with respect to both $g_{\mu\nu}$ and $\eta_{\mu\nu}$. Asymptotically the spacetime is flat and in the absence of self-interactions the scalar field oscillates with frequency proportional to its mass $\Phi \sim \exp[\mathrm{i}\mu t]$. Closer to the BH, the field is accreted and its amplitude and hence density grow (Clough, Ferreira, and Lagos, 2019; Hui et al., 2019; Bamber et al., 2021). After a short time, it reaches a quasi-stationary state with a density profile that (in the case of $\mu M \sim 1$) is proportional to $r^{-3/2}$. Notably, since the boundary conditions effectively feed in more scalar field over time, in the purely massive case, the overall amplitude of the cloud continues growing and does not stabilize, although the shape of the profile remains the same.

We start from the homogeneous initial conditions in Equation (2.4) with $\phi_0 = 0.2M$, and study the evolution of the self-interacting scalar field around a BH of mass M. We study cases where the mass of the scalar $\mu = M^{-1}$ and $\mu = 0.1M^{-1}$ to explore lower and higher masses, although in both cases the Compton wavelength of the scalar field is roughly of the same order of the Schwarzschild radius. These values are partly set by the numerics but also cover the wave-like regime where the density near the BH is not strongly suppressed by the pressure effects arising from a large Compton wavelength (unlike relatively low mass scalars $\mu M \ll 1$). We use a grid resolution of $N^3 = 128^3$ with 6 levels of refinement, and a physical box size of $L = 576M$, which gives a grid spacing of $0.07M$ at the BH horizon.

Diagnostics are used as in the approach of Clough, 2021; Croft, 2023; Traykova et al., 2021; Traykova et al., 2023; Aurrekoetxea et al., 2024a, and so a current $J^\mu = \xi^\nu T^\mu_\nu$ is defined in the direction ξ^ν, as well as an associated charge and flux

$$Q = -n_\mu J^\mu \,, \qquad F = \alpha N_i J^i \,, \tag{2.8}$$

where N_i is the outward normal direction to the surface that bounds the volume. If ξ^ν is a Killing vector then $\nabla_\mu J^\mu = 0$ and the change in charge is balanced by a flux through a surface. For the fixed background case $\xi^\nu_t = (1, 0, 0, 0)$ is a Killing

vector, which gives the density and fluxes across surfaces

$$\rho_E \equiv Q_t = -\alpha\rho + \beta_k S^k \,, \tag{2.9}$$

$$F_E \equiv F_t = N_i \left(\beta^i(\alpha\rho - \beta^j S_j) + \alpha(\beta^k S^i_k - \alpha S^i\right) \,, \tag{2.10}$$

where $N_i = s_i/\sqrt{(\gamma^{jk}s_j s_k)}$is the normalised radial unit vector, with $s_i = (x, y, z)/r$. Here $\alpha = 1/\sqrt{-g^{00}}$ and $\beta_i = g_{0i}$. The quantities ρ and S_i are the components of the stress-energy tensor measured by the normal observers

$$\rho = n^\mu n^\nu T_{\mu\nu} \,, \qquad S_i = n^\mu T_{\mu i} \,, \tag{2.11}$$

where $n_\mu = (-\alpha, 0, 0, 0)$.

In Figure 2.2 We plot radial profiles of the density ρ_E at different times. The top and bottom panels correspond to $\mu M = 1$ and $\mu M = 0.1$ respectively, and each column corresponds to attractive ($\lambda < 0$), free ($\lambda = 0$) and repulsive ($\lambda > 0$) self-interactions. For $\mu M = 1$, the repulsive case ($\lambda > 0$) exhibits two interesting properties compared to the density profiles of the free and attractive interaction cases: (i) The profile is flatter towards the centre, resulting in a more "cored" structure. (ii) The density saturates, leading the profile to settle into a stable configuration. In contrast, the attractive ($\lambda < 0$) and non-self-interacting ($\lambda = 0$) cases show minimal differences from each other within the limited time range shown here. This limitation arises because the dynamics of scalar fields in concave potentials are more challenging to resolve numerically when the timescale of the oscillation is short. We also study the low-frequency regime by decreasing the mass of the scalar field to $\mu M = 0.1$. The results are plotted in the bottom panel of Figure 2.2. In this limit, the power laws are approximately the same, but the results show that attractive self-interactions ($\lambda < 0$) enhance the growth of the cloud, while repulsive self-interactions ($\lambda > 0$) stabilize and saturate the growth. It can be seen that the field density first stabilizes at the horizon, and as accretion continues, it extends out to larger radii. The accretion flux stabilises at a maximum value and the scalar field is able to reach a stationary state.

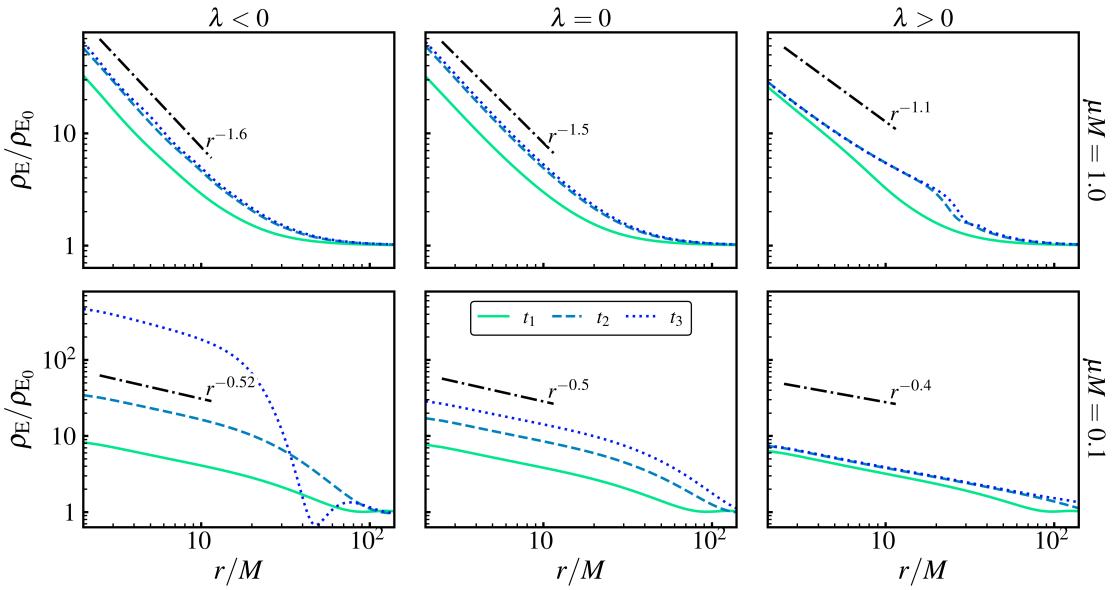


Figure 2.2: Growth of the dark matter density profile for different values of the mass μ and self-interaction λ. The top (bottom) panel shows the high (low) mass case as labelled. The left panels plot the evolution of the radial profiles for attractive self-interactions $\lambda = -150$ ($\lambda = -0.003$), the middle for the purely massive cases and the right panel for repulsive cases $\lambda = 1.6$ ($\lambda = 0.015$). The values of μ and λ for the high and low mass cases have be chosen so that the self interaction strength (see Section 2.6) is approximately of order unity. Beyond this however, λ has been adjusted on an experimental basis for each simulation so that the timescale for growth beyond the quadratic regime would occur in simulation time, and also to ensure the simulation was stable. The top and bottom rows therefore should be viewed independently from one another and as such only roughly compare the difference in evolution between high and low mass cases for the field. The different lines show the field density profiles over time $\{t_1, t_2, t_3\} = \{100, 200, 220\}M$ ($\{t_1, t_2, t_3\} = \{200, 600, 1000\}M$), normalised by the initial (homogeneous) density. The black dashed line shows a power law fit to the lines. It is expected that the power law profiles to continue to propagate outwards over time, but the limitation is in the length of the simulations by the domain size.

This saturation and enhancement of the scalar cloud, depending on the sign of the self-interactions, is more apparent in the top panel of Figure 2.3, where we plot the evolution of the density at $r = 3M$. Initially, the scalar field evolves with small oscillations in the quadratic part of the potential for all three cases, so the growth due to accretion shows negligible differences at early times. However, as the scalar field amplitude increases, it begins to probe the quartic part of the potential, leading to variations in the density profile. The attractive case shows an enhancement in the growth of the cloud compared to the $\lambda = 0$ case, while repulsive self-interactions result in the saturation of the cloud's growth. One can interpret these results using

the bottom three panels of Figure 2.3, where the fluxes are extracted at two different radii, $r = 3M$ and $r = 20M$. The difference between the fluxes, ΔF, indicates the build-up of energy within the volume. The panels show that for the attractive case, ΔF grows faster than in the $\lambda = 0$ case, leading to an enhancement in the cloud's density. In contrast, for the repulsive case, the outer and inner fluxes balance perfectly, causing the density profile to saturate and remain constant.

The saturation of the repulsive case can be understood as follows. The stability of the scalar cloud is related to the balance of the Newtonian gravitational potential, the gradient pressure of the scalar field, and the pressure induced by the self-interactions

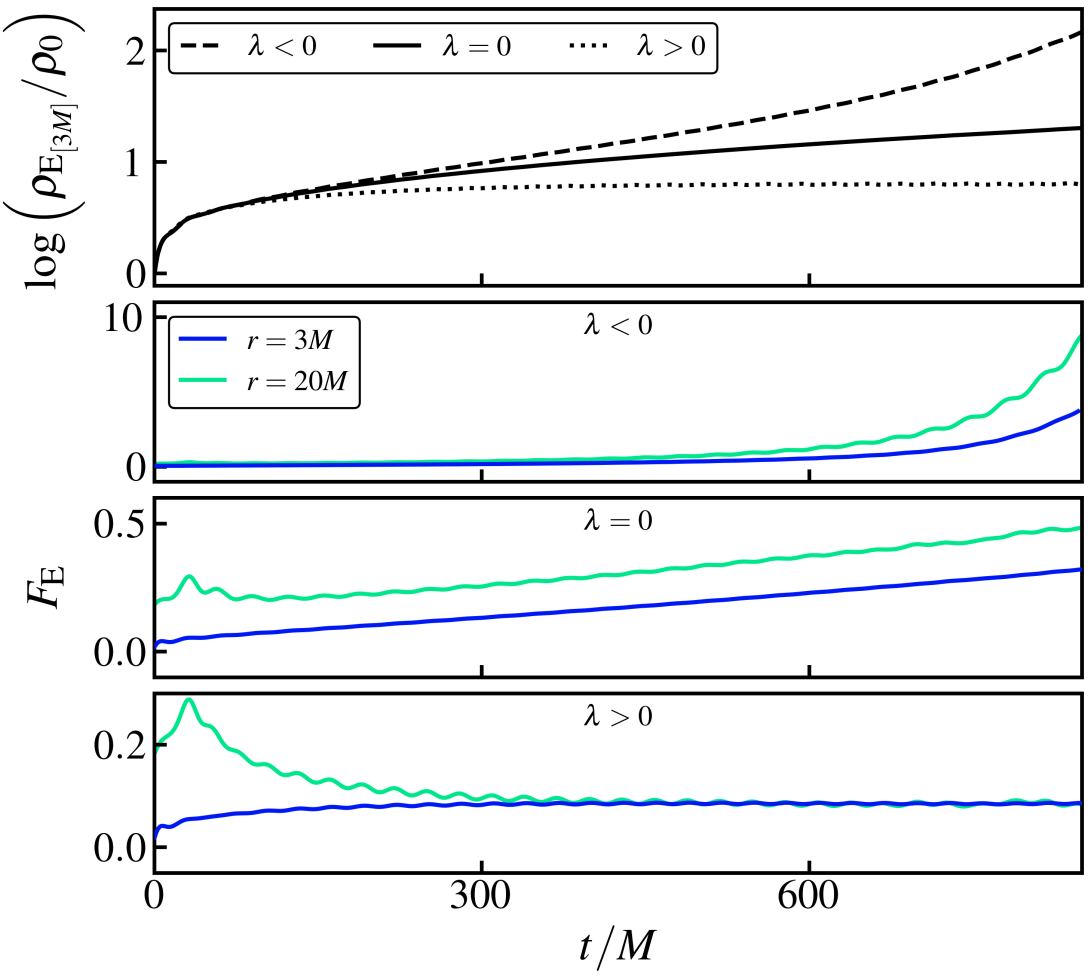


Figure 2.3: Top panel: Density of the dark matter cloud at $r = 3M$ for different values of $\lambda = -0.003$, $\lambda = 0$ and $\lambda = 0.015$. Bottom panels: Fluxes at radii $r = 3M$ and $r = 20M$. The growth of the density can be understood from the differences in the fluxes between these radii, which diverge, saturate or reach zero for each of the cases.

λ. When the scalar field probes the quadratic part of the potential, the gravitational potential dominates and results in the accretion and growth of the cloud. As has already been seen, this implies that the scalar field increases its amplitude and starts probing the quartic part of the potential. In the $\lambda > 0$ case, the interaction potential creates a repulsive "pressure" that allows the scalar cloud to reach hydrostatic equilibrium, with the repulsive self-interaction balancing the self-gravity.

The interaction changes sign and becomes attractive when $\lambda < 0$, so the only contribution that can lead to hydrostatic equilibrium is the gradient pressure of the scalar field. Attractive self-interactions enhance the growth of the cloud, but the gradient pressure cannot compete with the attractive force due to self-interactions. When the density becomes too high, the system undergoes a rapid collapse – a bosenova-like event. This collapse increases the density and potential energy, leading to an explosive ejection of energy from the cloud and a subsequent reduction in density. The inset panel of Figure 2.4, showing the evolution of density at $r = 3M$, illustrates this process. The evolution of the density profile is shown in the top panel, with blue to green colours (and transparency) depicting time, with the density profiles coloured more green representing the density of the cloud at later times. The density profile starts homogeneous but grows near the BH as time progresses. The density at all radii increases until $t \approx 1000M$, when the profile suddenly collapses and the cloud explodes, radiating part of its mass outwards and dramatically dropping in density at low radii. Inspecting the green set of profiles at $r < 50M$, one can see how the density profile of the cloud falls and even drops below the initial homogenous value of ρ_{E_0} in places as this matter is expelled outwards to larger radii, which is seen as a 'travelling' hump which slowly moves to the right of the plot as time increases. In the bottom panel we plot the evolution of the radial fluxes. Initially, the fluxes are positive everywhere, so that there is an ingoing flux of DM towards the BH as the field accretes. As the density grows, the field explores flatter regions of the potential, meaning that the density and flux is enhanced. Eventually, the flux reaches a maximum at $r \approx 25M$ and $t \approx 1000M$, after which the flux rapidly becomes negative. This results in the explosion that

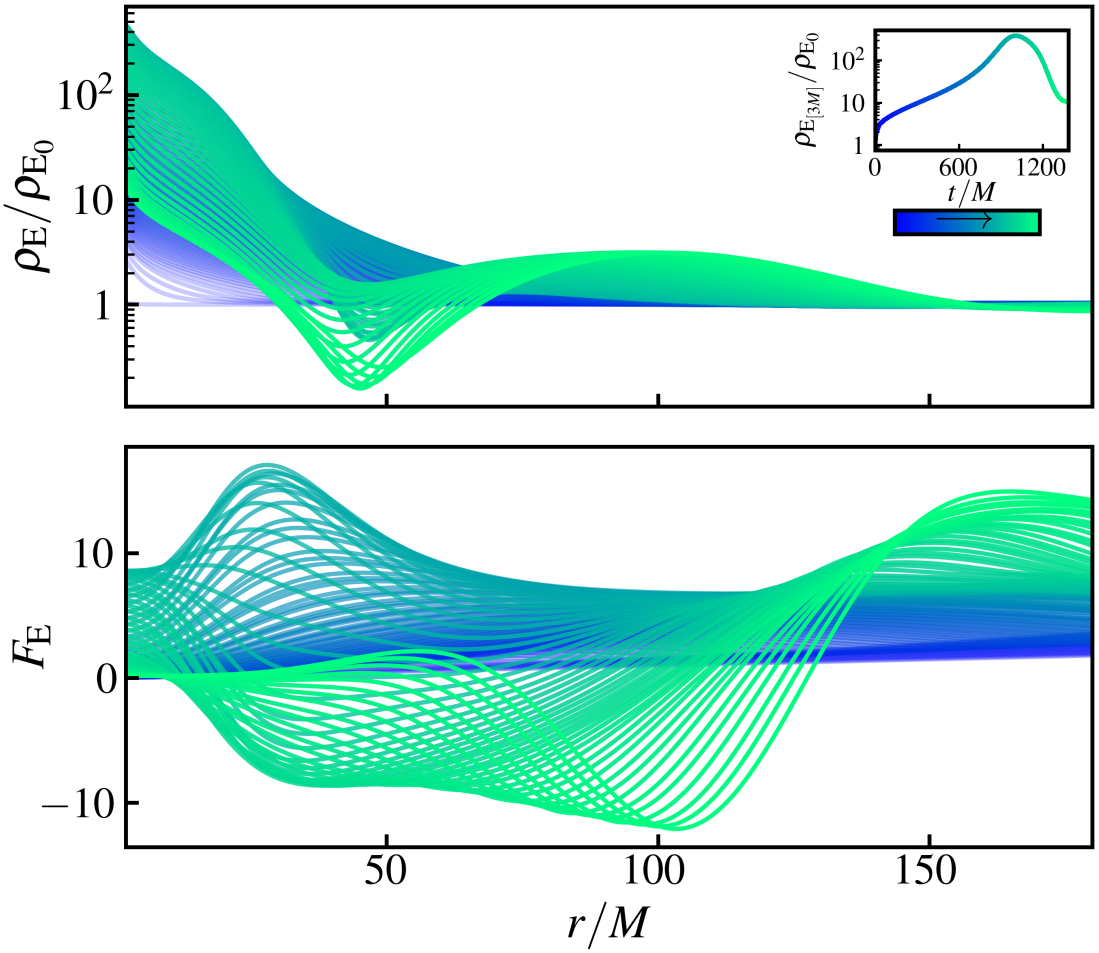


Figure 2.4: Evolution of the density and fluxes for the bosenova explosion for $\lambda = -0.003$. The top (bottom) panel shows the radial profiles of the density (radial flux). The inset panel tracks the density value at $r = 3M$. Positive and negative fluxes correspond to ingoing and outgoing radiation, respectively. The density reaches a peak following which the cloud collapses, and the system undergoes a violent burst of energy that propagates outwards.

reduces the density near the BH. This matter propagates outwards, shown by the negative fluxes at late times in the bottom panel of the figure. The travelling burst of matter is shown by the inverted hump of flux which begins at $r \approx 30M$, and moves to the right of the plot as time increases and therefore traces the movement of the matter which was expelled from near the BH at lower radii. At later times, the flux becomes positive once more which may be interpreted as a mixture of sudden, enhanced accretion to fill the under-density now present around the black hole, and a halting of the burst propagation, now beginning to infall once more.

2.5 Dark matter around an equal mass black hole merger

As discussed in the introduction, unlike in the particle DM case, equal-mass BHs immersed in scalars with Compton wavelength similar to the binary separation may retain the environment up to merger. This motivates the study of equal-mass binaries in such environments including backreaction, to quantify the potential impact on the GW signal. In such a case, the strong-field dynamics of the system needs to be resolved through numerical relativity. The line element is decomposed in the general ADM form (Arnowitt, Deser, and Misner, 1962)

$$ds^2 = -\alpha^2 \mathrm{d}t^2 + \gamma_{ij}(\mathrm{d}x^i + \beta^i \mathrm{d}t)(\mathrm{d}x^j + \beta^j \mathrm{d}t)\,. \tag{2.12}$$

Here γ_{ij} is the 3-dimensional metric, and the quantities α and β^i determine the choice of spatial hyperslicings and their coordinates, which follow the 1+log moving puncture gauge (Bona et al., 1995; Baker et al., 2006; Campanelli et al., 2006; van Meter et al., 2006). The extrinsic curvature tensor $K_{ij} = (2D_{(i}\beta_{j)} - \partial_t \gamma_{ij})/2\alpha$ is decomposed into a trace K and a traceless part A_{ij}, i.e. $K_{ij} = A_{ij} + (1/3)K\gamma_{ij}$. We evolve the coupled system of Klein-Gordon and general relativity equations in the CCZ4 formulation (Alic et al., 2012) using GRChombo (Andrade et al., 2021; Radia et al., 2022; Clough et al., 2015).

We study the tensor gravitational-wave modes emitted by the BBH. To do so, we extract the Newman-Penrose scalar Ψ_4 with tetrads proposed by Baker, Campanelli, and Lousto, 2002, projected into spin-weight -2 spherical harmonics,

$$\psi_{lm} = \oint_{S^2} \Psi_4\Big|_{r=r_{\rm ex}} \left[{}_{-2}\bar{Y}^{lm}\right] \mathrm{d}\Omega\,, \tag{2.13}$$

where $\mathrm{d}\Omega = \sin\theta\, \mathrm{d}\theta\, \mathrm{d}\varphi$ is the area element on the S^2 unit sphere. The merger or coalescence time for the 10-orbit binary in the absence of a dark matter cloud is $\bar{t}_{\rm c} \approx 2000\, M$, defined as when the amplitude of the dominant mode $|\psi_{22}|$ peaks. In Aurrekoetxea et al., 2024a, it was shown that scalar DM around the binary

induces a faster orbital decay, so that the gravitational-wave signal experiences a dephasing or delay of the coalescence time

$$\Delta t_{\rm c} \equiv t_{\rm c} - \bar{t}_{\rm c} \,. \tag{2.14}$$

In particular, it was found that the dephasing is maximized when the Compton wavelength of the scalar particle matches with the initial orbital separation of the binary, $2\pi/\mu \approx d_0$. For the 10-orbit binary, where $d_0 \approx 12M$, this corresponded to a scalar particle with mass $\mu \approx 0.5M^{-1}$.

Now we investigate the impact that repulsive and attractive self-interactions have on the growth of the DM cloud and the dephasing of the binary. For $\lambda > 0$, the system is evolved with the quartic potential in Equation (2.2). For $\lambda < 0$, we simulate the potential in Equation (2.3) to avoid unbounded values for large amplitudes of the field. We start from homogeneous initial conditions given by Equation (2.4) and choose Bowen-York initial data for A_{ij} for the boosted BHs (Bowen and York, 1980). The Hamiltonian and momentum constraints are solved using the CTTK-hybrid method (Aurrekoetxea, Clough, and Lim, 2023), so that the trace of the extrinsic curvature tensor is initially $K_0^2 = 16\pi G\rho_0$. We fix $\rho_0 \approx 10^{-9}M^{-2}$, $\mu = 0.43M^{-1}$, and vary both λ and ϕ_0 such that ρ_0 is unchanged via Equation (2.5). This approach ensures that the constraints only need to be solved once and the BHs have identical initial masses, velocities and directions for all the different runs. Then, any observed differences arise solely from their interaction with the DM cloud, and depend on the relative enhancements in the cloud density achieved for different scalar masses and interactions.

In Figure 2.5, we plot the evolution of the density (left to right) for three different self-interactions. The top and middle panels show the evolution of the DM cloud for attractive ($\lambda = -10^{-4}$) and without self-interactions ($\lambda = 0$). The profiles remain qualitatively unchanged, with both forming a similar overdensity between the BHs. In contrast, for repulsive self-interactions ($\lambda = 0.025$, bottom panel), the density of the DM cloud saturates, and there are significant changes in the structure of the cloud. Unlike the other two cases, repulsive self-interactions suppress the formation

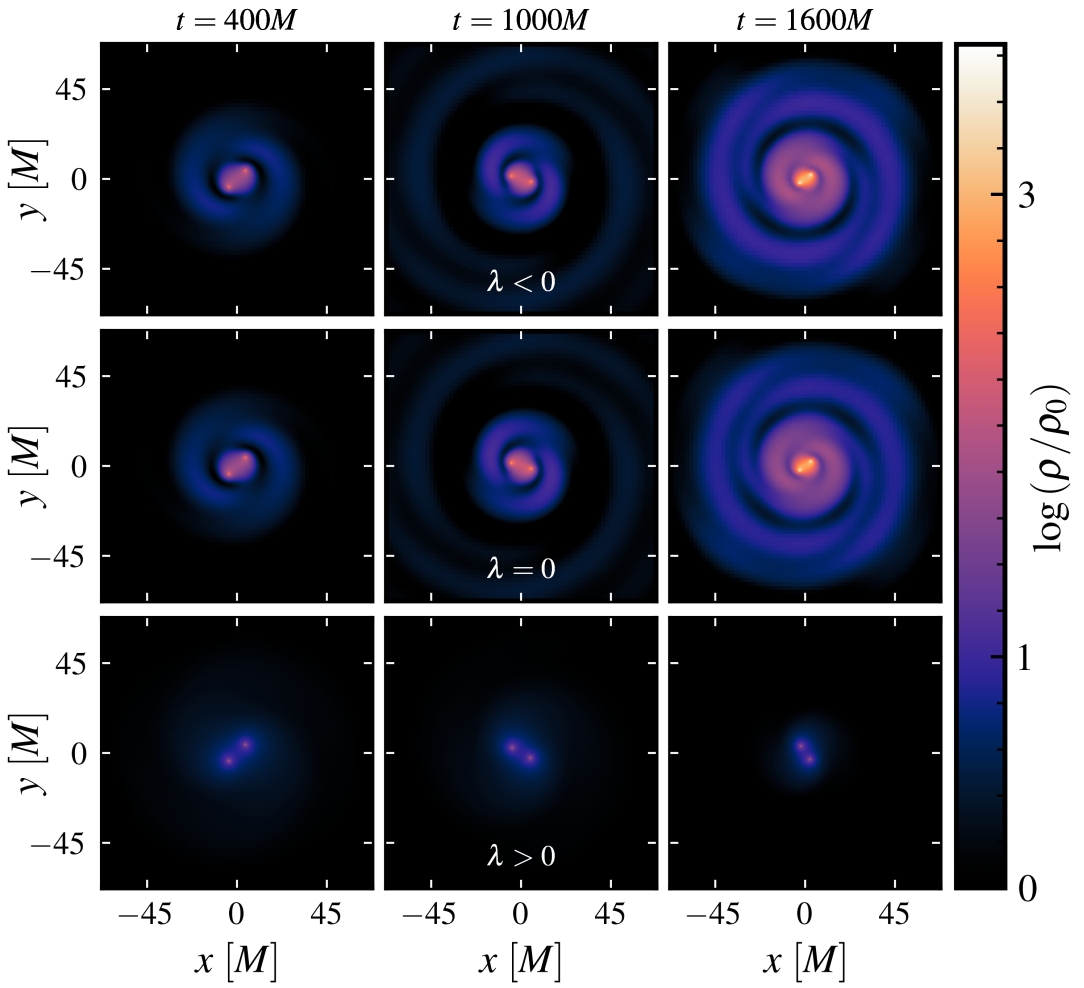


Figure 2.5: Evolution of the dark matter cloud for $\lambda = -10^{-4}$ (top), $\lambda = 0$ (middle) and $\lambda = 0.025$ (bottom). We plot 2D slices of the density. We see that in the repulsive case the overdensity around the binary is suppressed. In the attractive case shown here, the density does not become high enough to trigger a bosenova before the merger occurs, so its evolution is similar to the purely massive case, with only a slight enhancement in the density. A movie of the simulations can be found in https://youtu.be/ZeoMlUHknUM

of the central overdensity. In Figure 2.6, we plot the relative dephasing of the gravitational-wave signal. Repulsive self-interactions saturate the growth of the cloud, resulting in smaller dephasings. For attractive (but small) self-interactions, the dephasing is slightly larger due to the increased density of the cloud.

The cause of this dephasing can be quantified more precisely by computing the charges and fluxes associated with the currents in the time direction $\xi^\nu_t = (1, 0, 0, 0)$, angular direction $\xi^\nu_\phi = (0, -y, x, 0)$, and radial direction $\xi^\nu_r = -(0, x, y, z)/r$. The expressions for the time direction are in Eqns. (2.9-2.10), and the angular and

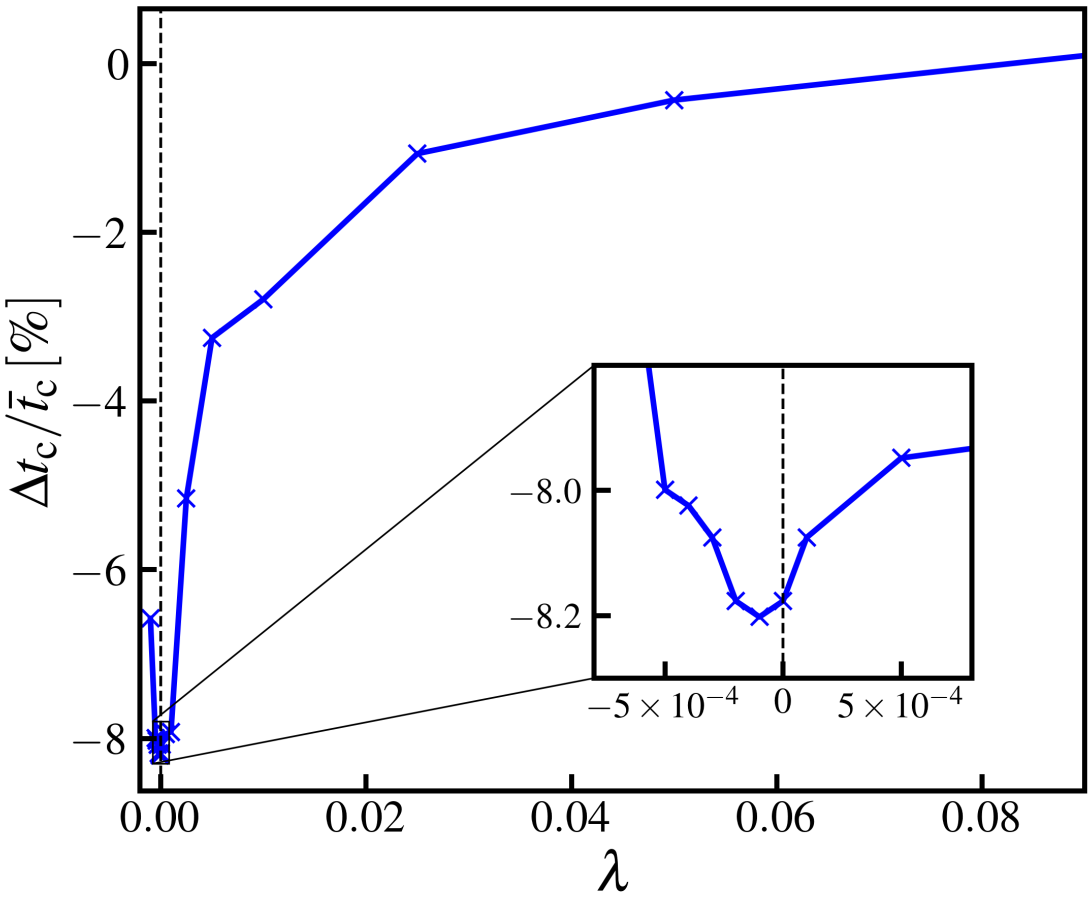


Figure 2.6: Decrease in the coalescence time $\Delta t_c \equiv t_c - \bar{t}_c$ extracted from the gravitational-wave signal, for different self-interaction scenarios. For positive values of λ (repulsive interactions), the dephasing is rapidly lost as the self-interaction increases due to the saturation of the cloud density. For small negative λ (attractive interactions), the density of the cloud is enhanced and the binary experiences a larger dephasing. However, for sufficiently negative λ, the bosenova-like event decreases the density and the dephasing is again reduced.

radial directions

$$Q_{\{\phi,r\}} = S_i \xi^i_{\{\phi,r\}} \,, \tag{2.15}$$

$$F_{\{\phi,r\}} = -N_i \beta^i S_j \xi^j_{\{\phi,r\}} + \alpha N_i S^i_j \xi^j_{\{\phi,r\}} \,, \tag{2.16}$$

where again $N_i = s_i/\sqrt{(\gamma^{jk} s_j s_k)}$ and $s_i = (x, y, z)/r$. We also track the flux through two inner surfaces that move together with the BHs, which introduces additional advection terms to the flux $F^{\rm BH} = \alpha N^{\rm BH}_i J^i - N^{\rm BH}_i \beta^i \, (Q - S/2)$.

As these directions do not correspond to Killing vectors, there must be an exchange of the charge between matter and curvature, which can be estimated by

computing the *source* terms associated to these currents

$$S = \alpha T^{\mu}_{\nu} \nabla_{\mu} \xi^{\nu} \,. \tag{2.17}$$

It is this quantity that corresponds to gravitational forces in the Newtonian limit, and that quantifies the way in which momentum is extracted from the binary by the matter[3]. The expressions for the source terms for the energy, angular and linear momentum currents are

$$S_t = -\rho \partial_t \alpha + S_i \partial_t \beta^i + \frac{\alpha}{2} S^{ij} \partial_t \gamma_{ij} \tag{2.18}$$

$$\begin{aligned} S_{\{\phi,r\}} =& \alpha S^{\mu}_{\nu} \partial_{\mu} \xi^{\nu}_{\{\phi,r\}} + \alpha S^{\mu (3)}_{\nu} \Gamma^{\nu}_{\mu\sigma} \xi^{\sigma}_{\{\phi,r\}} \\ & - S_{\nu} \beta^i \partial_i \xi^{\nu}_{\{\phi,r\}} + S_{\nu} \xi^{\mu}_{\{\phi,r\}} \partial_{\mu} \beta^{\nu} - \rho \xi^{\mu}_{\{\phi,r\}} \partial_{\mu} \alpha \end{aligned} \tag{2.19}$$

where $\partial_t \gamma_{ij} = -2\alpha K_{ij} + D_i \beta_j + D_j \beta_i$, and both $\partial_t \alpha$ and $\partial_t \beta^i$ are given by the moving puncture gauge conditions. The quantities $\partial_{\mu} \xi^{\nu}$ are all zero except $\partial_x \xi^y = 1$ and $\partial_y \xi^x = -1$.

In Figure 2.7 we plot the time integration of these quantities within a radius of $40M$ from the centre of the binary. These quantify the extraction of mass ΔM, angular momentum ΔJ and radial momentum ΔP_r from the binary by the matter, which drive the dephasing and the change in the coalescence time $\Delta t_{\rm c}$ since they affect the balance in the angular momentum $J = Mr^2 \, (2\pi/T)$. We compare the attractive $\lambda = -10^{-4}$ and repulsive $\lambda = 0.025$ cases to the $\lambda = 0$ case. In these cases, the attractive self-interaction gives the greatest relative dephasing at around 8.2%, although it is very similar to the purely massive case. The slight difference in the coalescence time can be attributed to the slightly higher values of ΔJ and ΔP_r in Figure 2.7. In the repulsive case, the dephasing is only around 1%: the exchanges in energy and angular momentum are highly suppressed (top and middle panels in Figure 2.7), whilst the radial exchange of momentum shown in the bottom panel is smaller.

In principle one may naively expect that increasing the attractive self-interactions further enhances the density of the cloud, but Figure 2.6 shows that for $\lambda \lessapprox -10^{-4}$,

[3]We also include in this quantity the accretion of the matter charge into spheres around the BHs, since the volume integral is not defined at the singularity.

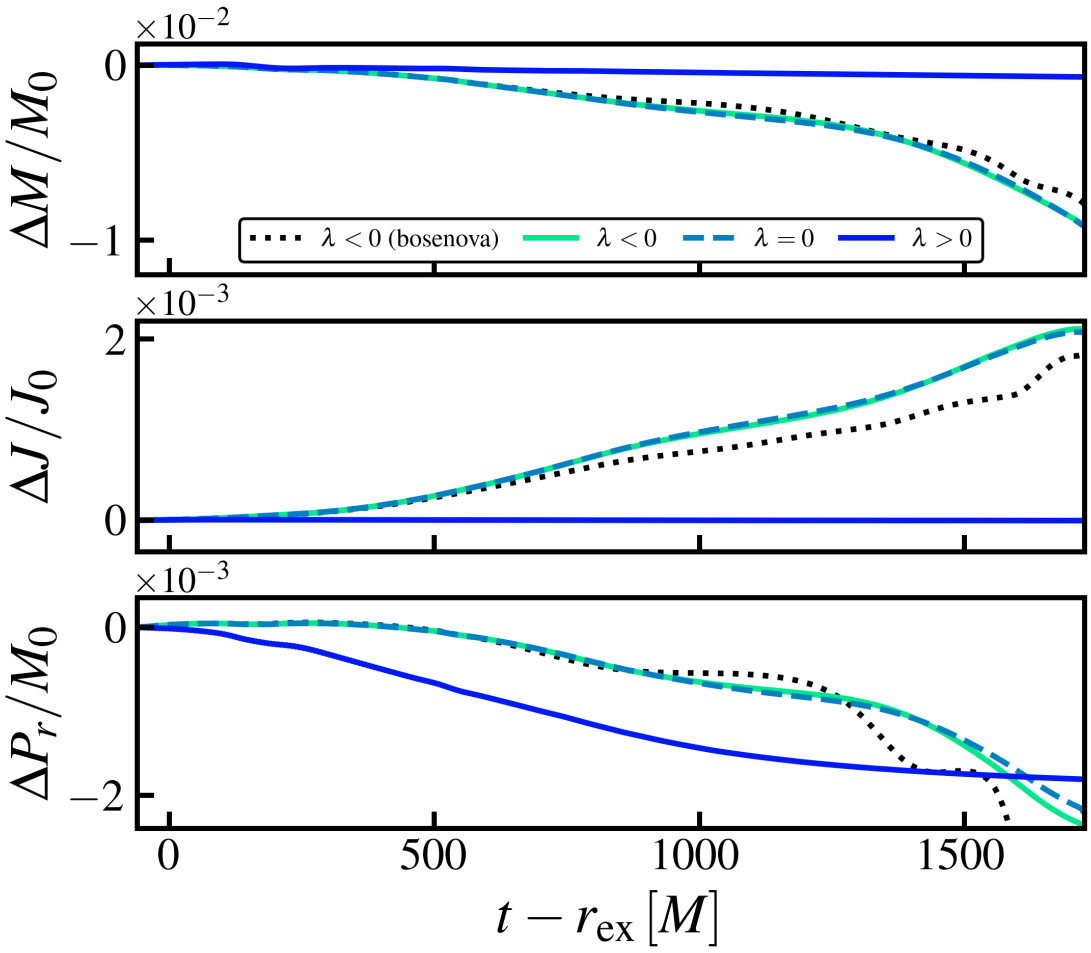


Figure 2.7: Time integrals of the source terms for the energy, angular and radial momentum currents (top, middle and bottom panels, respectively). These quantify the extraction of mass ΔM, angular momentum ΔJ and radial momentum ΔP_r from the binary by the matter, illustrating the effect the dark matter cloud has on the binary. We compare the attractive $\lambda = -10^{-4}$ and repulsive $\lambda = 0.025$ cases to the $\lambda = 0$ case, which are those shown in Figure 2.5.

the dephasing Δt_c decreases. This is because, as in the isolated BH case, when the field reaches sufficiently high values, the non-linear attractive interactions of the scalar field dominate and lead to a bosenova-like event. There is a sudden collapse at the overdensity between the binary that results in a burst of matter, disrupting the cloud, as illustrated in Figure 2.8. This behaviour seems to be generic for any kind of attractive self-interaction with $\lambda|\Phi|^4$ at leading order, but it is expected that the exact form of the ejection and recovery to the steady growth phase after the bosenova will depend somewhat on the form of the potential beyond the $\lambda|\Phi|^4$

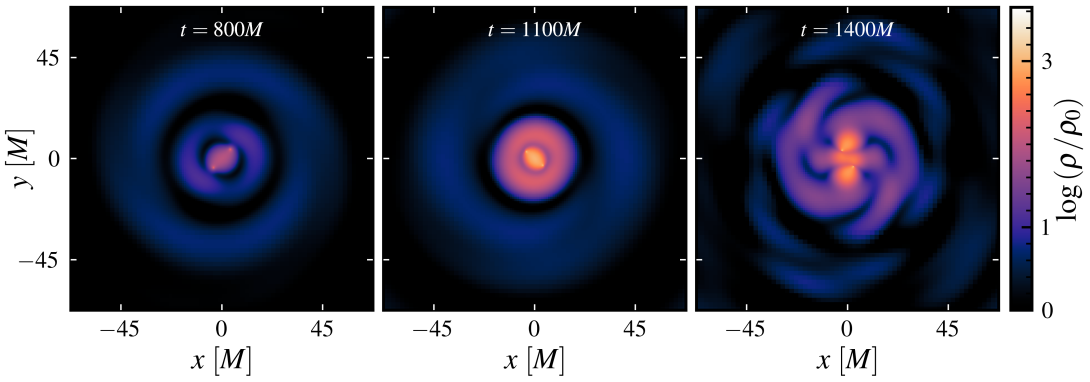


Figure 2.8: Bosenova explosion and disruption of the cloud during an equal-mass black hole merger for $\lambda = -10^{-3}$. The density of the dark matter cloud is enhanced due to the attractive self-interactions (compare the middle panel of this figure and those in Figure 2.5). However, attractive self-interactions dominate and result in the sudden collapse of the cloud, with a burst of radiation that reduces the cloud density, and hence the dephasing. A movie of the simulation can be found in https://youtu.be/ZeoMlUHknUM

regime. The critical value of λ at which it occurs will also depend on factors like the asymptotic density, the scalar mass and the parameters of the binary.

2.6 Discussion

We have studied the evolution of self-interacting dark matter around black holes using numerical simulations. Motivated by EMRIs, we have explored the accretion-driven growth of a scalar DM overdensity around an isolated Schwarzschild BH. It was found that the profile of the cloud is cored for repulsive self-interactions, and more cuspy when these are attractive. Repulsive self-interactions saturate the density of the cloud, while attractive self-interactions lead to a faster growth. However, when attractive self-interactions dominate the dynamics, this enhancement can be temporarily reversed by a bosenova-like event, as the cloud collapses and the system emits a violent burst of energy.

We used numerical relativity simulations that include backreaction onto the metric to study the growth of a DM cloud during an equal-mass BH merger. We have extracted the gravitational waves radiated during the inspiral, merger and ringdown phases and quantified the impact that self-interactions have in the waveform by computing the dephasing of the gravitational-wave signal. We found that repulsive

self-interactions reduce the amount of dephasing compared to the purely massive case because they suppress the DM density that accumulates around the binary. Attractive self-interactions enhance it, but if the cloud grows significantly, the binary triggers a bosenova-like event as in the isolated BH case. The cloud is then disrupted by the motion of the BHs, and the dephasing is again reduced relative to the purely massive case.

In the simulations, we are constrained to use larger values of the density in order to see the dephasing effects on the short timescales on which one is able to simulate the merger. Smaller values should result in similar effects but on longer timescales. To put the values we use into context – constraints exist on the total mass of dark matter around the supermassive BH at the centre of our galaxy, putting it at less than 0.1% of the mass of the central BH within 10^4 Schwarzschild radii using constraints from the S2 star (Abuter et al., 2022; Foschi et al., 2023). This corresponds to densities of roughly $10^{-15}M^{-2}$ in our units, which is significantly lower than the value of $10^{-9}M^{-2}$ that we use as the asymptotic density. However, the densities we use are lower than possible densities from superradiant clouds where 4-10% of the BH mass can be contained within a cloud out to around 1-10 Schwarzschild radii (Herdeiro, Radu, and Santos, 2022), which gives values up to $\sim 10^{-5}M^{-2}$. They are comparable to those expected from the isolated adiabatic evolution of dark matter spikes (Bertone et al., 2024).

Whilst the densities studied are large compared to galactic average values, the self-interactions that we study here are relatively small and not at a level that conflict with current observational constraints. The dimensionless coupling for the self-interaction $\bar{\lambda}$ for a scalar mass $m = \hbar\mu/c$ is constrained by BBN and structure formation to be (Li, Rindler-Daller, and Shapiro, 2014; Arbey, Lesgourgues, and Salati, 2003; Diez-Tejedor, Gonzalez-Morales, and Profumo, 2014)

$$\bar{\lambda} \lesssim 1 \left(\frac{m}{\mathrm{eV}}\right)^4 . \tag{2.20}$$

In our simulations we fixed the scalar mass to be $m \approx 5 \times 10^{-17}\ (M/10^6 M_\odot)^{-1}$ eV, which corresponds to the constraint

$$\bar{\lambda} \lesssim 6 \times 10^{-66} \left(\frac{M}{10^6 M_\odot} \right)^{-4} . \tag{2.21}$$

We chose the parameter $\lambda \approx \mathcal{O}(0 - 0.1) M^{-2}$, for which the upper end corresponds to the dimensionless value

$$\bar{\lambda} \sim 10^{-89} \left(\frac{M}{10^6 M_\odot} \right)^{-2} , \tag{2.22}$$

or equivalently a self-interaction energy scale $f = \sqrt{\lambda}/m \sim M_{\rm Pl}$. This interaction strength is below the bound above for all realistic BH masses[4].

Based on our results, self-interactions appear to mainly reduce rather than enhance dephasing effects. Even for the relatively small values of self-interaction studied, the non-linear part of the potential played a significant role, and both attractive and repulsive values mostly resulted in lower dephasing than the purely massive case. We are only considering a short period close to merger, and so given the much longer timescales available for build-up of the cloud prior to this point, the effects could become relevant well in advance of the actual merger. In the case of attractive self-interactions, this could mean bosenova-like explosions recurring during the inspiral. The absence or observation of such bursts can be used to put constraints on the existence of attractive scalar DM, as has been proposed in Budker et al., 2023; Arakawa et al., 2024; Arakawa et al., 2023; Eby and Takhistov, 2024.

[4]For comparison, the QCD axion has $\bar{\lambda} \sim 10^{-53}$ for an axion decay constant $f \sim 10^{12}$ GeV and a mass $m \sim 10^{-5}$ eV (Sikivie and Yang, 2009).

"If we want things to stay as they are, things will have to change."

— Giuseppe Tomasi di Lampedusa
The Leopard

3

Symmetry Restoration and Vacuum Decay around Black Holes

3.1 Motivation

In this chapter, I will extend on the work that I described in Chapter 2 regarding self-interacting dark matter models. In that chapter, I discussed how I, as part of a collaboration, simulated clouds of dark matter with quartic potentials undergoing accretion around black holes, and the phenomena which occur due to the density enhancement caused by this accretion mechanism. In essence, this density enhancement allows the field to explore further reaches of its potential, and into regions where the quartic terms dominate over the quadratic ones and so experience different effects based on the relative strength and sign of the self interaction terms.

A very interesting extension to this idea is to now include potentials with multiple minima. The setup and motivation remains the same as before - first consider a diffuse cloud of scalar wave-like dark matter surrounding a Schwarzschild black hole. As the field accretes around the black hole and so the field deviates from the initially quadratic potential, the question now is how the field will react to the changes induced not only by these additional terms8, but ones which induce multiple minima.

The motivation for studying these multi-minima potentials, in addition to it being a natural extension to the work we completed before, is that Nature often

hints at the idea of phase transitions. In brief, there are models predicted by particle physics suggesting that various fields in the universe have undergone what is known as a phase transition - a sudden change from one state to the other. In the simple context of a field residing in some potential, this implies a swift transition in the field going from oscillating in one minimum to another, or else in a manner which fundamentally changes the symmetry of the field. For one example, a field can go from oscillating in such a way that it is symmetric in reflection about the central axis or in some rotation if it's imaginary, to a state which breaks this. Our motivation is in trying to understand how black holes can catalyse these symmetry changing, and more generally, phase changing events. The work in this chapter is described in a published paper - Marsden et al., 2024. In it, I ran many of the simulations and contributed to the understanding of the behaviour of the fields when undergoing these various processes, as well as producing plots to help that end.

3.2 Introduction

Throughout its history, the Universe has undergone a cascade of phase transitions (Peter and Uzan, 2013). These transitions have been associated with symmetry breaking, in which the vacuum structure for fundamental fields has morphed from one of higher symmetry to one of lower symmetry (Coleman and Weinberg, 1973). It has also been proposed that our universe could, now or in the past, have lived in a false vacuum of some field, and that phase transitions may then be triggered that take it to a true minimum (Coleman, 1977; Callan and Coleman, 1977; Coleman and De Luccia, 1980; Hawking and Moss, 1982).

The case of quantum transitions between vacuum states has been extensively studied, including the impact of black holes in early works by Hawking and Moss (Moss, 1985; Hawking, 1981), and their potential to enhance the transition rate in more recent work by Gregory, Moss and others (Gregory, Moss, and Withers, 2014; Burda, Gregory, and Moss, 2015b; Burda, Gregory, and Moss, 2015a; Burda, Gregory, and Moss, 2016), see also Berezin, Kuzmin, and Tkachev, 1988; Hiscock, 1987; Arnold, 1990; Berezin, Kuzmin, and Tkachev, 1991; Mukaida and Yamada,

2017; Oshita, Yamada, and Yamaguchi, 2019; Oshita, Ueda, and Yamaguchi, 2020; Shkerin and Sibiryakov, 2021.

In this chapter, we study alternative, purely classical transitions that arise around black holes when they are immersed in coherent scalar fields (such as those that model wave-like dark matter with small mass and high number density, see Hui, 2021 for a review). Such effects are the extreme end of the study of self-interactions in the field, where attractive and repulsive forces arising from the shape of the potential play a role in the classical evolution. In the repulsive case (see Chapter 2 and Aurrekoetxea et al., 2024c) the self interactions saturate the growth of density around the black hole (BH), and so the field is confined to one region of the potential. In the attractive case, the growth does not saturate (at least initially), and as a result the field explores greater and greater regions of the potential. It is then affected by the wider shape and in particular the presence of other minima.

The effects that attractive corrections to a quadratic potential have on scalar (and vector) clouds near BHs have previously been considered for the case of self-interacting dark matter like axions (Shapiro and Paschalidis, 2014; Berezhiani et al., 2024; Kadota et al., 2024; Alonso-Álvarez, Cline, and Dewar, 2024; Boudon et al., 2024; Feng et al., 2022; Alvarez and Yu, 2021), including their potential to create so called 'bosenova' explosions in the case of superradiant clouds where the BH must have a relatively high spin and the scalar mass must satisfy the superradiant condition (Yoshino and Kodama, 2012; Yoshino and Kodama, 2015; Omiya et al., 2023; Omiya, Takahashi, and Tanaka, 2022; Omiya, Takahashi, and Tanaka, 2021; Omiya et al., 2024; East, 2022; Baryakhtar et al., 2021; Boskovic et al., 2019) (see Brito, Cardoso, and Pani, 2015 for a review). There, however, self-interactions can cause the saturation and dissipation of the cloud, which radiates and transitions to other bound states (although additional accretion may help (Hui et al., 2023)). The accretion case we study is therefore arguably more generic and inescapable, provided a (stable, sufficiently abundant) scalar with some multi-minima potential exists.

Other studies of classical transitions have focussed on more exotic overdensity scenarios, such as soliton stars (Coleman, 1985; Friedberg, Lee, and Pang, 1987;

Seidel and Suen, 1994; Arakawa et al., 2024), spontaneous scalarization (Doneva et al., 2024) or extra couplings to matter (Hook and Huang, 2018; Balkin et al., 2023), or been related to attempts to model the quantum process as a classical but stochastic process (Linde, 1992; Brown and Dahlen, 2011; Braden et al., 2019; Blanco-Pillado, Deng, and Vilenkin, 2019; Hertzberg and Yamada, 2019; Hertzberg, Rompineve, and Shah, 2020; Braden et al., 2023; Jenkins et al., 2023; Jenkins et al., 2024), with simulations that indicate that the transition (or decay rate) matches the quantum, path integral estimate up to factors of $O(1)$. The process described here is inherently classical and deterministic, and simply a consequence of the scalar field evolution on a curved background, rather than an approximation to a quantum system (although it may correspond to some semi-classical limit of a quantum process, it does not rely on fluctuations to occur).

We will characterise how the BH accretion process can lead the scalar field to gradually explore multiple vacua. Depending on the form of the potential, this may result in symmetry restoration or trigger a phase transition through vacuum decay. Such processes could be ubiquitous throughout the history of the Universe; BHs exist over a range of mass scales and over a range of times, and may serve as catalysts for such transitions. We consider an isolated Schwarzschild BH, characterising it through numerical simulations and extracting the key features and timescales that impact on observables.

3.3 Multi-minima wave-like dark matter models

In a cosmological setting, phase transitions arise from radiative corrections in field theory, which modify the effective potential seen by the field.[1] In classical field theory one considers the scalar field potential to be fixed and studies the

[1] In the case of a scalar field, Coleman & Weinberg (Coleman and Weinberg, 1973) explored how corrections to the potential could modify the vacuum structure, restoring symmetry at high energies. A chemical potential (Schäfer et al., 2001) or finite temperature corrections (Dolan and Jackiw, 1974) can have a similar effect.

dynamics of the field within it. We study the dynamics of a real scalar field ϕ, solving the Klein-Gordon equation

$$\nabla^\mu \nabla_\mu \phi - V'(\phi) = 0\,, \tag{3.1}$$

where ∇_μ is the covariant derivative operator associated to the metric $g_{\alpha\beta}$. We solve the Klein Gordon equation on a fixed Schwarzschild background, in horizon penetrating Cartesian Kerr–Schild coordinates (Visser, 2007)

$$\mathrm{d}s^2 = \left(\eta_{\mu\nu} + \frac{2M}{r} l_\mu l_\nu\right) \mathrm{d}x^\mu \mathrm{d}x^\nu\,, \tag{3.2}$$

where $\eta_{\mu\nu} = \mathrm{diag}(-1, 1, 1, 1)$ and M is the mass of the black hole. Here $l_\mu = (1,\, x/r,\, y/r,\, z/r)$ is the ingoing null vector with respect to both $g_{\mu\nu}$ and $\eta_{\mu\nu}$. We use t to represent the Kerr-Schild time coordinate, which is related to the usual Schwarzschild $\bar{t}$ as $\bar{t} = t - 2M \log(r - 2M)$. The radial coordinate r is the same in both systems. These coordinates allows one to evolve the fields smoothly across the horizon without the freezing that would occur in Schwarzschild-like coordinates, but we still need to excise the diverging region around the singularity. This freezing occurs in metrics which have the lapse go to zero at the event horizon. As the lapse function is related to the progression of time between each hypersurface, a lapse of zero effectively means no time progression, and so matter gets 'stuck' on the horizon in these simulations, like it would for the standard Schwarzschild lapse which indeed, goes to zero at the horizon. We focus in the plots on the behaviour in the observable region outside the horizon.

To illustrate both the mechanisms of symmetry restoration and vacuum decay, we choose a scalar potential with multiple minima

$$V(\phi) = \frac{\lambda}{4}\left(\phi^2 - \eta^2\right)^2 + \frac{g}{3}\eta\left(\phi + \eta\right)^3\,, \tag{3.3}$$

where λ and g are dimensionless coupling constants and η parameterizes the symmetry breaking scale. The cubic term controls the difference in the energy of each vacuum; in the $g = 0$ limit, the potential simplifies to the usual double-well

potential with degenerate vacua at $\phi_\pm = \pm\eta$. The locations of the minima are given by the parameters of the potential as

$$\phi_- = -\eta\,, \tag{3.4}$$

$$\phi_+ = +\eta\left(\frac{1}{2} + \frac{1}{2}\sqrt{1 - 12x + 4x^2} - x\right)\,, \tag{3.5}$$

where $x \equiv (g/2\lambda)$ and the difference in vacuum energy densities is given by $\Delta V \equiv V(\phi_+) - V(\phi_-)$, which is positive if $g > 0$ and negative if $g < 0$.

To lowest order around these minima, the potential is $V(\phi) \approx \mu^2\phi^2/2$, with mass $\mu \approx \sqrt{2\lambda}\eta$. In a flat spacetime, a spatially homogeneous value of the field ϕ close to a minimum would oscillate around it with frequency given by the mass μ. Thus, asymptotically far from the black hole the solutions of the scalar field have the form $\phi \propto \cos(\mu\bar{t})$ (which differs only by a slowly varying phase for Kerr-Schild time t at large r). In the purely massive case, closer to the black hole, the BH gradually accretes a cloud of scalar field (Clough, Ferreira, and Lagos, 2019; Bamber et al., 2021), described by the Heun functions as in Hui et al., 2019; Vieira, Bezerra, and Muniz, 2014; Hortacsu, 2012, with a power law envelope and characteristic oscillations of the spatial profile on length scales set by the scalar wavelength. Whilst the scalar in principle extends to infinity, in a physical scenario the accretion will only occur over a finite radius. In practice, one can treat it as infalling from the boundary (Hui et al., 2019). The presence of repulsive self-interactions ($V'' > 0$), can stabilise the accretion process and prevent the field amplitude from growing (Aurrekoetxea et al., 2024c). Attractive self-interactions ($V'' < 0$), on the other hand, result (at least initially, near the minimum of the potential, and as long as there is an asymptotic reservoir of scalar field to feed it) in a continuous growth of the profile, such that closer to the horizon, the amplitude of oscillations increases (Aurrekoetxea et al., 2024c). This means that the scalar field can explore other features of the potential, such as adjacent vacuum states.

It will be useful to define a mean, time averaged, value of the scalar field at some coordinate radius r

$$\langle\phi(r,t)\rangle \approx \frac{1}{T}\int_t^{t+T}\phi(r,t')dt'\,, \tag{3.6}$$

where $T \simeq 2\pi/\mu$ is the local period of the oscillation. If the field oscillates around the negative minimum of the potential $\langle\phi(r,t)\rangle = -\eta$.

In this chapter, we study the dynamics of scalar fields in black hole spacetimes for potentials with multiple minima. We fix $\eta = 1$, $\lambda = 0.1M^{-2}$ so that $\mu M \sim 0.5$ and vary g to study symmetry restoration and vacuum decay (we use geometric units $G = c = 1$, so that $[\phi] = 1$, $[\rho] = M^{-2}$). We choose the initial homogeneous value of the scalar field to be $\phi_0 = -0.8\eta$, so that it resides near the negative vacuum of a symmetry broken phase. These choices fix the asymptotic energy density to $\rho_0 \approx 0.03\lambda\eta^4$. If the local density of the scalar environment is much smaller than the curvature scale of the BH, $\rho M^2 \ll 1$, one can neglect the back-reaction of the scalar field on the metric. This allows us to rescale the results to different physical densities, as the equation of motion is invariant under the transformation $\phi_0 \to a\phi_0$ (or equivalently $\rho_0 \to a^2\rho_0$), as long as we keep μ constant via $\eta \to a\eta$ and $\lambda \to \lambda/a^2$.

We perform numerical simulations of the growth of the field using GRDzhadzha (Aurrekoetxea et al., 2024b; Andrade et al., 2021), with octant symmetry to simulate a physical box size of $L = 576M$, a coarsest grid resolution $N^3 = 256^3$ grid points, and 6 levels of refinement, which gives the finest resolution $dx_{\rm finest} = 0.035M$ at the BH horizon, located at $r = 2M$.

3.4 Results

We consider in turn the case of symmetry restoration, for degenerate minima, and then vacuum decay between false and true vacua. Movies of the two processes can be found in https://youtu.be/c2vcNoX8fVs

3.4.1 Symmetry restoration

We start by studying the case with $g = 0$, where $\Delta V = 0$ and, thus, the potential has two degenerate vacua at $\phi_\pm = \pm\eta$. In the left panel of Figure 3.1 we plot the potential, and in the right panel the evolution of the scalar field at the black hole horizon $r = 2M$ (note the use of the Kerr-Schild coordinates, corresponding to infalling observers). While asymptotically far from the black hole the field

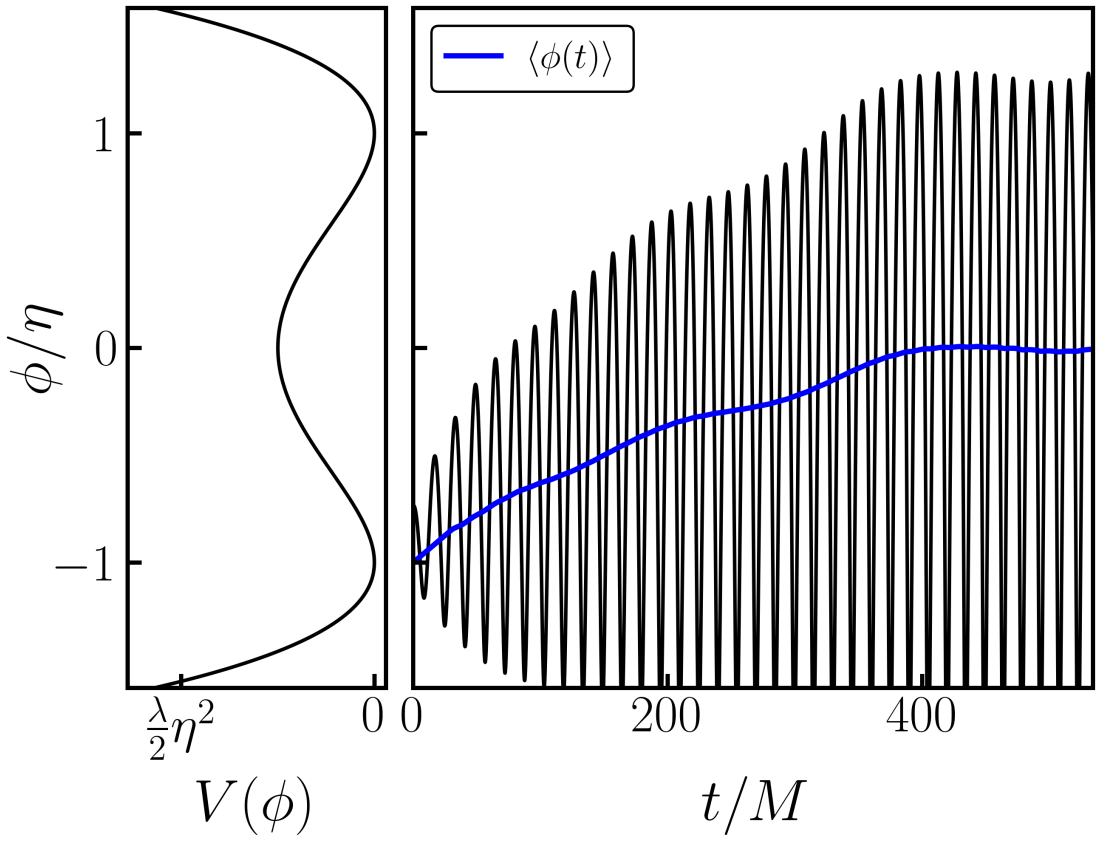


Figure 3.1: Symmetry restoration case, where the value of the scalar field at $r = 2M$ transitions the barrier and explores the other vacuum (black line). In blue we plot the mean value of the scalar field, which transitions from a symmetry broken phase at $\langle\phi(t)\rangle_{\rm bh} = -\eta$ to a restored phase at $\langle\phi(t)\rangle_{\rm bh} = 0$.

oscillates around the negative minimum ϕ_-, at smaller radii the field evolves over time. Initially it remains around ϕ_-, but the amplitude of the oscillations grows due to the increased density resulting from the accretion. The scalar field starts to probe the quartic part of the potential, and when the cloud has become dense enough, the field transcends the barrier and reaches the other vacuum state at $\phi_+ = +\eta$. The region of restored symmetry phase extends beyond the horizon and gradually expands as more matter is accreted - its extent will ultimately depend on the asymptotic reservoir available.

One can derive conditions on the timescale for the transition using the following argument. The field ϕ is at its maximum, when its time derivative is zero. The

energy density is, then approximately given by

$$\rho \approx V(\phi) + \frac{k^2}{2}(\phi + \eta)^2 \tag{3.7}$$

where $k \approx \mu$ is the typical inverse length scale of the gradient. When the field reaches the positive vacuum, at $\phi_+ = \eta$, the gradient term is the only contribution to the energy density, so that $\rho \approx 2k^2\eta^2 = 4\lambda\eta^4$. We choose the asymptotic, background, value of the density to be $\rho_0 \approx 0.03\lambda\eta^4$, which means the density near the black hole has to grow by ≈ 100 times to reach $\rho \approx 4\lambda\eta^4$. The timescale for the transition Δt is related to the scalar accretion rate $\dot{\rho}$. Using that, the accretion by the black hole is approximately given by $\dot{M} \sim \rho_0 v R^2$, with $v \approx 0.5$ the radial velocity,

$$\Delta t \approx \frac{4\lambda\eta^4 - \rho_0}{\dot{\rho}} \approx 4M\left(\frac{4\lambda\eta^4}{\rho_0} - 1\right). \tag{3.8}$$

We find that symmetry should be restored at $\Delta t \approx (\rho - \rho_0)/\dot{\rho} \approx 400M$, which is consistent with what we observe in Figure 3.1. After this state is reached the mean of the field near the black hole $\langle\phi\rangle_{\rm bh}$ appears to remain roughly constant, it now effectively evolves in a symmetric potential.

It is instructive to focus on the radial profiles of the mean value $\langle\phi(r,t)\rangle$, which we plot in Figure 3.2 at different times. Initially the scalar field oscillates around the negative minimum everywhere, so that $\langle\phi(r,t)\rangle = -\eta$ for all radii. The scalar amplitude grows near the black hole due to the accretion, so that the field transcends the barrier near the horizon and starts to oscillate periodically over the full double-well potential. Hence, $\langle\phi(t)\rangle_{\rm bh} = 0$ and symmetry is restored at that radius. However, the effects of gradients and asymptotic boundary conditions play an important role. At large radial distances from the black hole, the field remains oscillating around $\langle\phi(t)\rangle_\infty = -\eta$, so that adjacent values of the field (in space) experience a restoring force towards the original minimum. Since the symmetry restored phase requires the field to reach a certain density, it will only extend out as far as this density is reached. Hence, the timescale for symmetry restoration will strongly depend on the accretion rate. From Figure 3.2 one can infer that the symmetry restored phase propagates outwards, into the symmetry broken phase.

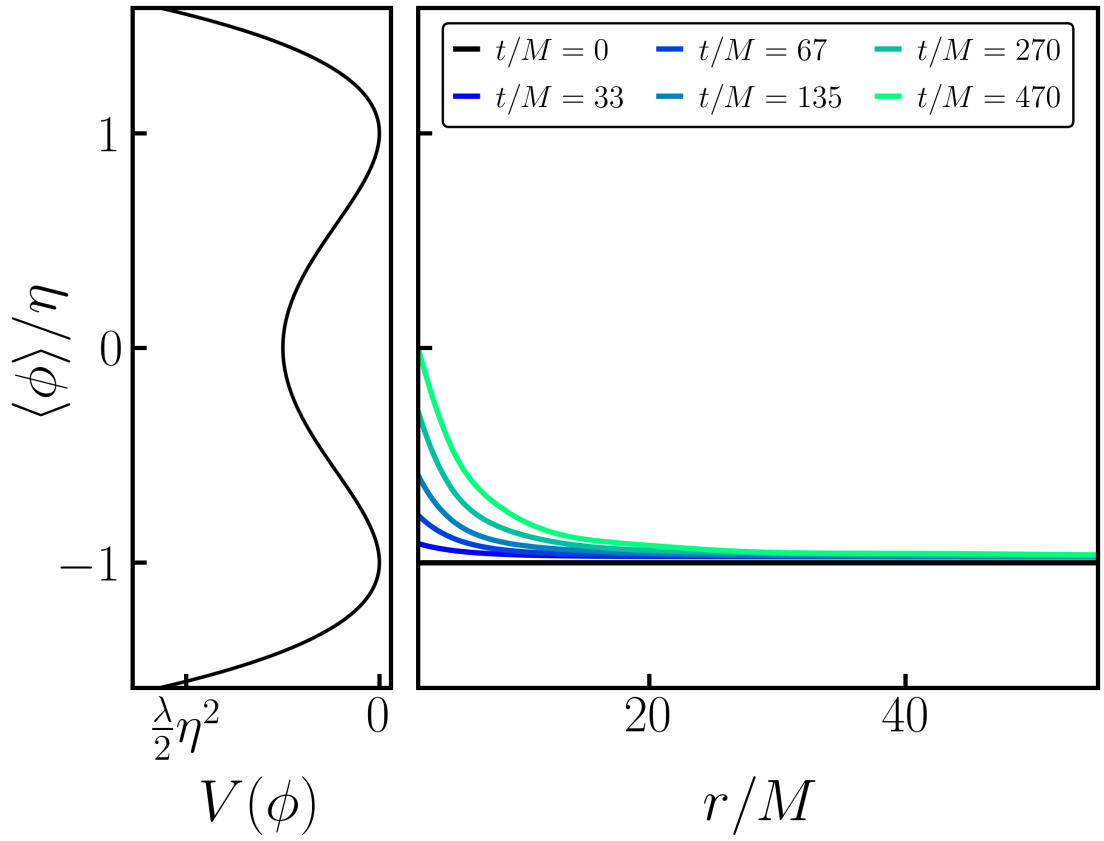


Figure 3.2: Evolution of the mean scalar field radial profile over time. Symmetry is restored near the black hole horizon as $\langle\phi(t)\rangle_{\rm bh} = 0$, and the field remains pinned down at $\langle\phi(t)\rangle_\infty = -\eta$ asymptotically. The restoration phase slowly grows outwards as the black hole accretes more scalar field.

This is a slow process, driven by the build up of the scalar matter via accretion, and so is different from the well-known expanding bubble of a new phase that is nucleated when there is a vacuum decay, which will be seen in the following section.

A question to ask, is what the end state of the process is. The density will only continue to increase whilst there is an asymptotic reservoir of the scalar feeding the growth. So only in the infinite accretion limit would the field fully restore symmetry. At some point the reservoir may be depleted and the cloud will then gradually decay into the black hole (a process that can be extremely long on astrophysical timescales for light scalars (Barranco et al., 2012)).

We also vary the initial value of the scalar field to test the robustness of these results and their sensitivity to the chosen initial parameters. In Figure 3.3, we compare the evolution of the mean scalar field $\langle\phi\rangle$ extracted at $r = 2M$ for

initial scalar field values $\phi_0 = \{0.7\eta, 0.8\eta, 0.9\eta\}$. These correspond to asymptotic densities $\rho_0 = \{0.065, 0.032, 0.009\}\,\lambda\eta^4$.

The accretion of scalar dark matter by the black hole is approximately given by $\dot{M} \sim \rho_0 v R^2$, with v the radial velocity, so that the density growth rate is

$$\dot{\rho} \sim \frac{\rho_0 v}{2M}\,, \tag{3.9}$$

where we have used $\dot{M} \sim \dot{\rho} R^3$ and $R = 2M$. This equation provides the right scaling and using the accretion rates we extract from the simulations, we estimate $v \approx 0.5$, so that $\dot{\rho} \approx \{2,\, 1,\, 0.2\} \times 10^{-3} M^{-3}$. Using the analytical estimate described previously for the timescale

$$\Delta t \approx \frac{4\lambda\eta^4 - \rho_0}{\dot{\rho}} \approx 4M \left(\frac{4\lambda\eta^4}{\rho_0} - 1 \right)\,, \tag{3.10}$$

We predict that symmetry restoration should occur at $t/M \approx \{200, 400, 2000\}$. This is in agreement with the observed timescales in Figure 3.3.

3.4.2 Vacuum decay

We now study how black holes can catalyze vacuum decay. To do so, we vary g in Equation (3.3), breaking the degeneracy between the minima by introducing a difference in vacuum potential energy densities ΔV. If $g < 0$, the energy difference between the minima is negative $\Delta V < 0$, and ϕ_- and ϕ_+ correspond to a false (metastable) and a true vacuum, respectively. This means that, as opposed to the degenerate case we have discussed before, there is now a preference for the field to decay to the lower energy state at ϕ_+.

The process for $g = -0.04 M^{-2}$ is illustrated in Figure 3.4, which shows how the profile of the time averaged scalar field $\langle \phi(r,t) \rangle$ changes over time. Close to the black hole, accretion drives the growth of the amplitude of the scalar field until it transcends the barrier and starts exploring the true vacuum ϕ_+ by forming a true vacuum bubble. When this bubble is large enough so that the energy difference between vacua can overcome the wall tension, it is more favourable for the bubble to expand radially outwards. The energy difference ΔV is transferred to the bubble

wall velocity, so that it quickly accelerates and expands at ultrarelativistic speeds. Gradients in the field once again play a crucial role. In this case, as opposed to keeping the field around the false minimum, they are responsible for dragging the rest of the field down to the true minimum, see Figure 3.5. Whilst this is similar to how vacuum bubbles that formed via quantum tunnelling propagate (Coleman, 1977; Callan and Coleman, 1977; Coleman and De Luccia, 1980), the timescale for the decay here is completely deterministic. In this classical scenario, the associated timescale is given by the initial conditions around the black hole, the details of the potential and the accretion rate (which itself depends on the ratio μM).

So what is the end state of this process? As the true vacuum bubble expands, it drags down the field in the false vacuum, which remains oscillating around the true minimum ϕ_+, as shown in Figure 3.5. More interestingly, very close to the black

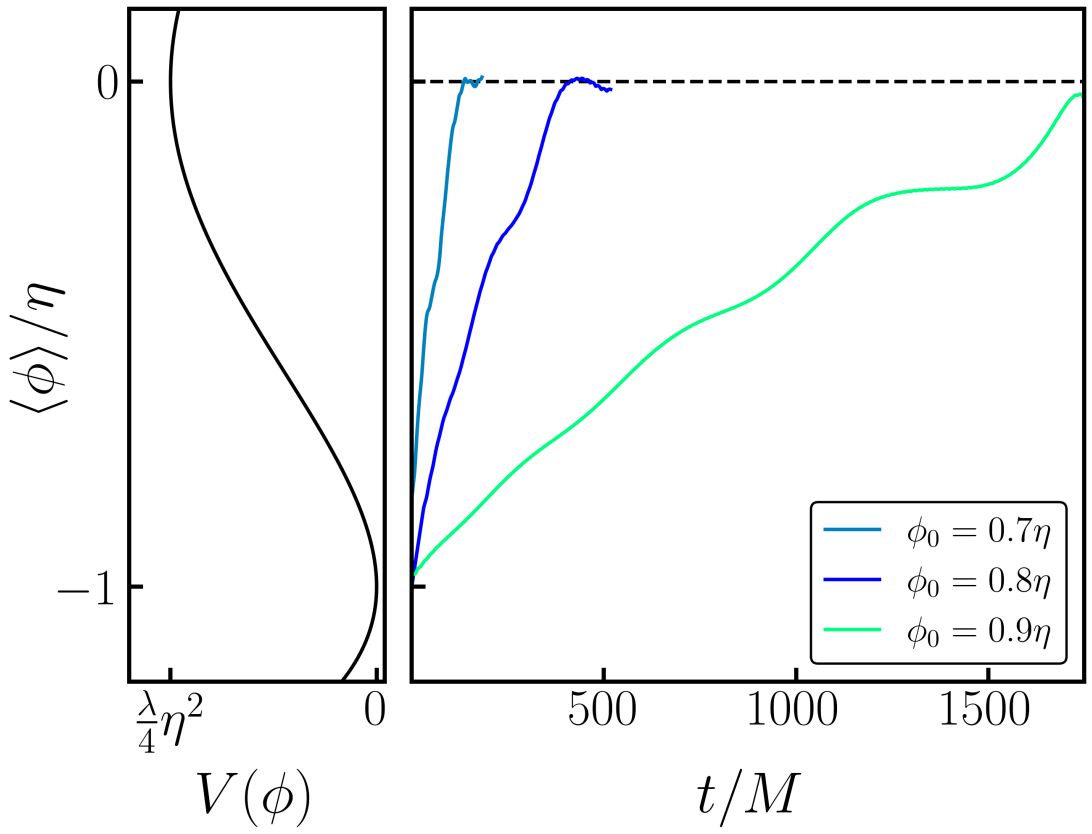


Figure 3.3: Evolution of the mean scalar field at $r = 2M$ for three different initial conditions ϕ_0. The figure shows how the smaller the initial density, the longer it takes to reach the symmetry restoration phase near the black hole.

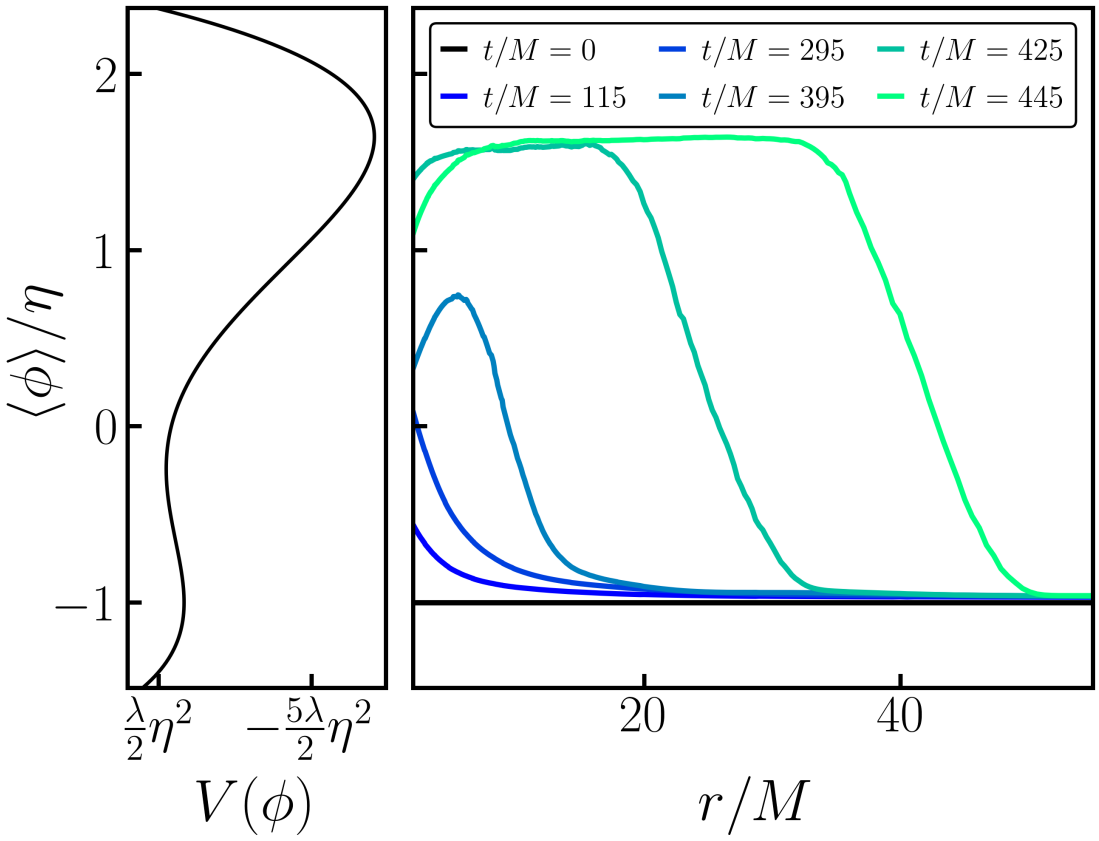


Figure 3.4: Evolution of the mean $\langle\phi(r,t)\rangle$ over time. The dynamics near the black hole triggers the nucleation of a true vacuum bubble that expands at ultrarelativistic speeds.

hole the symmetry restoration mechanism remains at play: the scalar field may sweep the whole potential, revisiting the false vacuum if the cloud density is large enough, see Figure 3.4. It would be interesting to study the possibility that this process could trigger the nucleation of a separate de Sitter universe when including backreaction, as observed in upward transitions of flyover vacuum decay (Blanco-Pillado, Deng, and Vilenkin, 2019). If, on the other hand, the field is decaying to an AdS vacuum $V(\phi_+) < 0$, the universe would transition to a collapsing phase that should eventually result in a Big Crunch, (although see also Cespedes et al., 2021 where scalar dynamics play a role). So although in this chapter we have ignored the effects of backreaction, this new vacuum decay mechanism triggered by black holes could have important gravitational consequences in the universe.

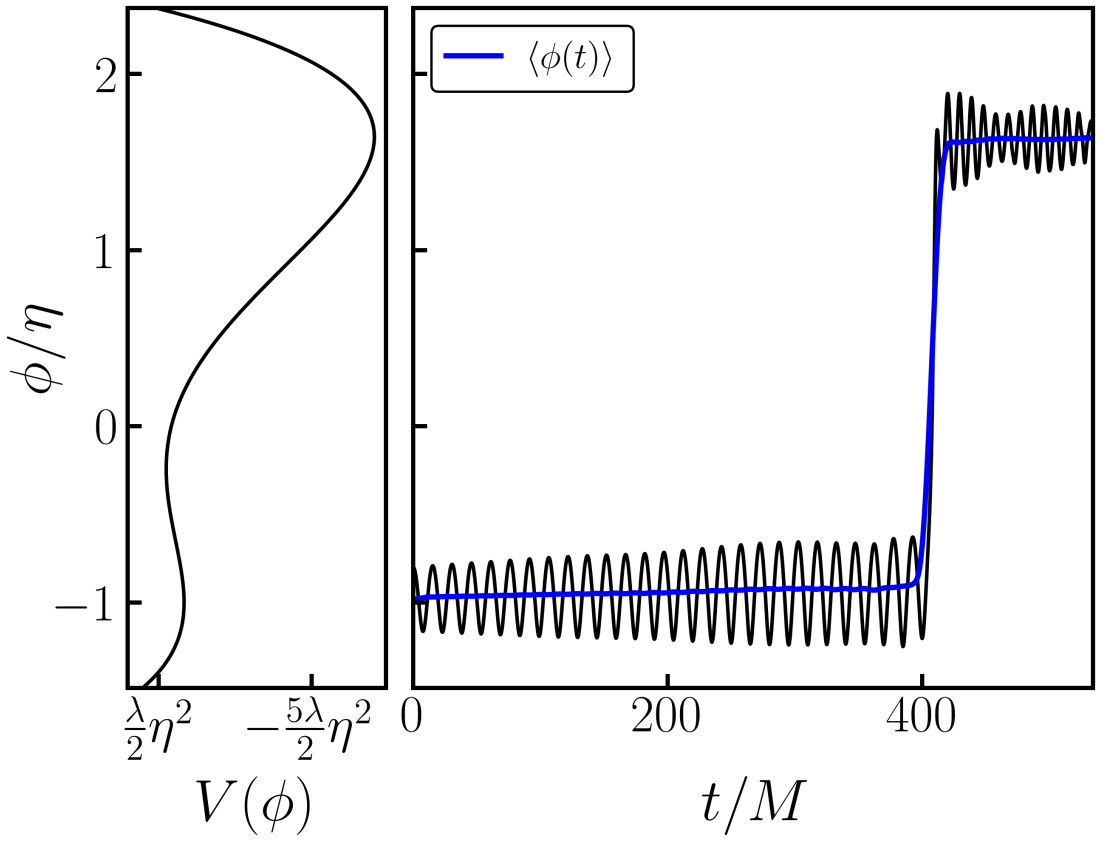


Figure 3.5: Vacuum decay case, showing the value of the scalar field at $r = 20M$ (black line). In blue we plot the mean value of the scalar field $\langle\phi(t)\rangle$, which transitions from ϕ_- to ϕ_+.

3.5 Discussion

In this chapter we proposed a novel mechanism by which black holes can alter the vacuum structure of the universe. The presence of compact objects leads to the formation of overdensities in scalar fields in their vicinity via accretion, which translate to large-amplitude oscillations in the potential. In the case of a scalar field embedded in a symmetry broken phase, these oscillations can transcend the potential barrier separating different vacua. As a result, shells of symmetry restored phase may be created around black holes. In the case in which the field is in a false vacuum, this mechanism can also trigger vacuum decay near the black hole, forming a true vacuum bubble that propagates outwards at ultrarelativistic speeds and changes the vacuum structure even far away from the black hole.

Whilst here we focus on the case of $\mu M \sim 0.5$ (with $\mu^2 = 2\lambda\eta^2$), this process should be relevant for scalar fields and black holes whenever $\mu M \gtrsim 1$ – the accretion clouds that we study are suppressed in the case of very light scalars (Hui et al., 2019). That is, for

$$\left(\frac{\mu}{10^{-11}\text{eV}}\right)\left(\frac{M}{M_\odot}\right) \gtrsim 1\,. \tag{3.11}$$

The decay rate of this classical mechanism is completely deterministic and depends on the accretion rate of the black hole. The timescale derived in Equation 3.8, which is valid for $\mu M \sim 1$, can be written in terms of physical quantities as

$$\Delta t \approx 1\,\text{sec}\,\left(\frac{\eta}{\text{GeV}}\right)^2\left(\frac{\text{GeV/cm}^3}{\rho_0}\right)\left(\frac{M}{M_\odot}\right)^{-1}\,, \tag{3.12}$$

showing that this mechanism could take place on short astrophysical timescales. The assumption that backreaction can be neglected is valid if the maximum density remains small relative to the curvature scale of the BH, which imposes the condition

$$\left(\frac{\rho_{\text{max}}}{10^{42}\,\text{GeV/cm}^3}\right)\left(\frac{M}{M_\odot}\right)^2 \ll 1\,. \tag{3.13}$$

This should be the case for most physically relevant scenarios involving stellar-mass black holes (the present average dark matter density is of order GeV/cm^3).

Here we have studied the simplest case of a minimally coupled scalar field around an isolated black hole, but similar transitions could be catalysed by accretion onto binary black holes (Bamber et al., 2023; Aurrekoetxea et al., 2024a). We conclude that the presence of scalar fields around black holes could have implications for a range of dark matter and early universe scenarios, the study of which we leave to future work.

十五从军征。八十始得归。 *At fifteen I joined the army on expedition. Only at eighty did I finally return.*
道逢乡里人：家中有阿谁？ *On the way I met a villager: "Who is left in my home?"*
遥望是君家，松柏冢累累。 *"See there in the distance is your home, among the pine, cypress, and graves piled high."*
兔从狗窦入，雉从梁上飞。 *"Rabbits enter through the dog hole, pheasants fly from the rafters."*
中庭生旅谷，井上生旅葵。 *In the parlour grows wild grain, upon the well grows wild vegetables.*
舂谷持作饭，采葵持作羹。 *I grind the grain for a meal, I pick the vegetables for the broth.*
羹饭一时熟，不知贻阿谁！ *Meal and broth are ready in an instant, but I know not whom to serve!*
出门东向看，泪落沾我衣。 *As I step out and look east, falling tears soak my clothes.*

— Unknown Han dynasty poet
Guo Maoqian 郭茂倩 *Anthology of Yuefu Poetry*
Translated by Jack Yuan

4 Rank-2 Tensor Fields in Numerical Relativity

4.1 Introduction

So far in this thesis, I have exclusively considered scalar fields. The final science chapter of this thesis is dedicated to rank-2 tensor fields and the methods by which to derive their associated equations of motion.

The first observation of gravitational waves was a revolution in the field. While first posed in the context of general relativity by Einstein, 1918, it was not until the LIGO collaboration (Aasi et al., 2015) almost a century later (Abbott et al., 2016) when they were first experimentally confirmed to exist. Numerical relativity played a large role in this discovery in the role of being used to calibrate the models which found the gravitational wave signals. In short summary, the initial hint of there being a gravitational wave signal was flagged by a generic gravitational-wave transient detector, which was then scanned more thoroughly by using templates. This is a technique called matched filtering, where families of potential gravitational waveforms given by the SEOBNRv2 effective-one-body model (Taracchini et al., 2014) are scanned through the data in these flagged section, looking for a 'match' between the gravitational-wave template and the raw output. A match means that a gravitational wave matching the form of the template has been found. These

effective-one-body models are directly calibrated to numerical relativity simulations [1]. Gravitational waves are solutions to the equations of motion for massless, rank-2 tensor fields and so are one of the motivations in this chapter for developing a useful approach to simulate rank-2 tensors in numerical relativity. I will also apply this method to scalar and vector fields to demonstrate both its versatility, but in its generality to other types of fields.

Our goal is to take an equation which is second order in time, and reduce it to a coupled system of differential equations which are first order in time. These describe the evolution of the field and its conjugate momentum, which is related to the time derivative of the field. By making this split, we end up with one equation which is found from the definition of the conjugate momentum, and a second from the equation of motion. On these two equations, we then perform a series of projections to find the Lie derivatives for the various fields. In the following, I apply this procedure to a massive rank 0 and 1 field to demonstrate the process, before applying it to rank 2 tensors.

4.2 Rank 0 - Scalar Field

In this example, I consider a real scalar field ϕ with potential $V(\phi)$ obeying the Klein-Gordon equation in Einstein gravity, and will demonstrate a simple method of finding the equations of motion. The scalar field action is:

$$S_\phi = \int d^4x\sqrt{-g}\left(-\frac{1}{2}\nabla^\mu\nabla_\mu\phi - V(\phi)\right) \tag{4.1}$$

Varying this action with respect to ϕ results in the Klein-Gordon equation:

$$\nabla^\mu\nabla_\mu\phi - V'(\phi) = 0 \tag{4.2}$$

Where we denote the partial derivative of the potential with respect to ϕ with the prime symbol. The standard approach to find the equations of motion in a

[1] While very accurate, it's not feasible to directly use the numerical relativity waveforms in matched filtering due to the comparative expense in producing them and so in building a comprehensive enough set of waveforms to cover the parameter space.

3+1 split would be to then define the conjugate momentum of this field as its negative time derivative, and then proceed to substitute this into the equation of motion and explicitly calculate the time derivative of the momentum through expanding all of the terms. This is laborious however as it involves steps such as substituting out four-dimensional Christoffel symbols for their three-dimensional counterparts, and quickly becomes complicated for when we want to repeat this process for fields of higher rank. Instead, we can define a vector field Ψ_μ for the scalar field, which is the covariant derivative of ϕ

$$\Psi_\mu = \nabla_\mu \phi. \tag{4.3}$$

Then, we write the most general 3+1 decomposition of Ψ_μ

$$\Psi_\mu = \kappa_\mu + n_\mu \Lambda \tag{4.4}$$

Where κ_μ is a general, purely spatial vector field and Λ is a scalar field. The meaning of κ_μ being spatial is that $n^\alpha \kappa_\alpha = 0$. We can now attempt to identify these general fields with specific objects. The conjugate momentum Π for the field ϕ is defined as

$$\mathcal{L}_n \phi = -\Pi \tag{4.5}$$

As $\mathcal{L}_n \phi = n^\mu \nabla_\mu \phi$, then we notice that $n^\mu \Psi_\mu = -\Pi$ and so $\Lambda = \Pi$. For similar reasons, we find that $\kappa_\mu = D_\mu \phi$ because $\gamma^\alpha{}_\mu \Psi_\alpha = \gamma^\alpha{}_\mu \nabla_\alpha \phi$ and $\gamma^\alpha{}_\mu \Psi_\alpha = \kappa_\mu$. With the equation of motion for ϕ found for Equation (4.5), we want to find the same for Π. This is done through the Klein-Gordon equation; we substitute in Equation (4.3):

$$\nabla^\mu \Psi_\mu - V'(\phi) = 0 \tag{4.6}$$

We can then expand this by using Equation (4.4)

$$\nabla^\mu \kappa_\mu + \Lambda \nabla^\mu n_\mu + n_\mu \nabla^\mu \Lambda - V'(\phi) = 0. \tag{4.7}$$

The key step is to use the fact that for spacetime covariant derivatives acting on purely spatial vectors[2],

$$\nabla^\mu V_\mu = \frac{1}{\alpha} D^\mu (\alpha V_\mu). \tag{4.8}$$

[2]See Baumgarte and Shapiro, 2010, Page 37, Equation (2.63)

We use this for the $\nabla^\mu \kappa_\mu$ term and then find

$$\mathcal{L}_n \Lambda = V'(\phi) - \frac{1}{\alpha} D^\mu \left(\alpha \kappa_\mu\right) - \Lambda \nabla^\mu n_\mu. \tag{4.9}$$

Lastly, we use $\nabla_\mu n_\nu = -n_\mu D_\nu \ln \alpha - K_{\mu\nu}$ and that $\kappa_\mu = D_\mu \phi$, $\Lambda = \Pi$ to reach the equation of motion for the conjugate momentum

$$\mathcal{L}_n \Pi = V'(\phi) - \frac{1}{\alpha} D^\mu \left(\alpha D_\mu \phi\right) + K\Pi. \tag{4.10}$$

For massive scalars, $V(\phi) = \frac{1}{2} m^2 \phi^2$ where m is the mass. Then, recalling the definition of the time vector from Equation (1.68), we arrive at the equations of motion we require

$$\partial_t \phi = \mathcal{L}_\beta \phi - \alpha \Pi, \tag{4.11}$$

$$\partial_t \Pi = \mathcal{L}_\beta \Pi + \alpha m^2 \phi - D^\mu \left(\alpha D_\mu \phi\right) + \alpha K \Pi. \tag{4.12}$$

We note that the choice to treat κ_μ as a relabelling of $D_\mu \phi$ is a choice. In theory, we could treat it as an evolving variable and find its own evolution equation through the time derivative of Equation (4.4). This is also an idea to consider for higher rank fields - we often 'over-describe' the system by having a surplus of equations and so have a freedom in choosing how we reduce them.

4.3 Rank 1 - Proca Field

This technique can now be repeated for a massive vector field (a Proca field). Classical electromagnetism permits two degrees of freedom, relating to the two possible polarisation vectors for the field. For the case of the Proca field, we introduce a new mass term quadratic in the field to the Lagrangian. The presence of this mass breaks the usual gauge symmetry we can apply in the massless, or Maxwellian case, and so we gain an extra degree of freedom, giving three in total The Lorenz gauge is effectively upgraded to a constraint as opposed to a gauge condition, which we shall also see in the case of the massive rank-2 tensor field. This extra degree of freedom corresponds to a longitudinal polarisation, in addition

to the two usual transverse polarisations we see in massless vector fields. Consider the action describing a massive, real vector field A_μ

$$S_A = \int d^4x\sqrt{-g}\left(-\frac{1}{4}F^{\mu\nu}F_{\mu\nu} - \frac{1}{2}m^2 A_\mu A^\mu\right). \tag{4.13}$$

Where $F_{\mu\nu}$ is the antisymmetric field strength tensor, defined as

$$F_{\mu\nu} = \nabla_\mu A_\nu - \nabla_\nu A_\mu. \tag{4.14}$$

The equation of motion for the 4-vector A_μ is

$$\nabla^\mu F_{\mu\nu} - m^2 A_\nu = 0. \tag{4.15}$$

or, by substituting out the field strength:

$$\nabla^\mu\nabla_\mu A_\nu - \nabla^\mu\nabla_\nu A_\mu - m^2 A_\nu = 0 \tag{4.16}$$

We can decompose the Proca field as follows

$$A_\mu = X_\mu + n_\mu \hat{X}. \tag{4.17}$$

where X_μ and $\hat{X}$ are both spatial. As with the scalar field case, we make a general decomposition of the field strength tenor - the equivalent of Equation (4.4). This is

$$F_{\mu\nu} = Q_{\mu\nu} + n_\mu P_\nu + n_\nu R_\mu + n_\mu n_\nu S, \tag{4.18}$$

where $Q_{\mu\nu}$, P_μ, R_μ are all purely spatial and S is a scalar. The notion of $Q_{\mu\nu}$ being 'spatial' means $n^\mu Q_{\mu\nu} = 0$. For the Proca field strength tensor, we need to take into account the antisymmetry in its indices. Inspecting Equation (4.18) shows that we must therefore have $R_\mu = -P_\mu$, $S = 0$, and $Q_{\mu\nu}$ to be antisymmetric in order for the overall decomposition of $F_{\mu\nu}$ to be antisymmetric. Doing this, and relabelling P_μ to E_μ, we see

$$F_{\mu\nu} = Q_{\mu\nu} + n_\mu E_\nu - n_\nu E_\mu. \tag{4.19}$$

Where $Q_{\mu\nu}$ is antisymmetric. We can calculate its value by doubly projecting Equation (4.19) with the projection operator after substituting in the definition of $F_{\mu\nu}$ in terms of A_μ. Doing this, we find:

$$Q_{\mu\nu} = D_\mu X_\nu - D_\nu X_\mu \tag{4.20}$$

$F_{\mu\nu}$ is therefore

$$F_{\mu\nu} = D_\mu X_\nu - D_\nu X_\mu + n_\mu E_\nu - n_\nu E_\mu. \tag{4.21}$$

We now proceed to find the equations of motion. The definition of E_μ from Equation (4.21) and by substituting in Equations (4.14) and (4.17), we see

$$E_\mu = -\hat{X} D_\mu \ln \alpha - D_\mu \hat{X} - \mathcal{L}_n X_\mu. \tag{4.22}$$

Rearranging this, we find the equation of motion for X_μ.

$$\partial_t X_\mu = \mathcal{L}_\beta X_\mu - \alpha E_\mu - \hat{X} D_\mu \alpha - \alpha D_\mu \hat{X}. \tag{4.23}$$

Due to the asymmetry of $F_{\mu\nu}$, the equation of motion for $\hat{X}$ is found differently. We return to Equation (4.15) and take the covariant derivative, producing

$$\nabla^\nu \nabla^\mu F_{\mu\nu} = m^2 \nabla^\nu A_\nu \tag{4.24}$$

Using the identity $\nabla^\mu \nabla^\nu T_{\mu\nu} = 0$, for an antisymmetric tensor field $T_{\mu\nu}$, we see

$$m^2 \nabla^\mu A_\mu = 0. \tag{4.25}$$

As the mass is in general non-zero, $m \neq 0$, this then amounts to the condition of $\nabla^\mu A_\mu = 0$. Note that this is the Lorenz gauge, now upgraded to a full constraint due to the presence of the mass term. We can now substitute in the decomposition of A_μ in terms of X_μ and $\hat{X}$ from Equation (4.17) to find the following equation of motion for $\hat{X}$

$$\partial_t \hat{X} = \mathcal{L}_\beta \hat{X} - \alpha D^i X_i - X_i D^i \alpha + \alpha K \hat{X} \tag{4.26}$$

We now wish to find the equation of motion for E_i, which is the equivalent of the vector momentum for the system. We return to Equation (4.15) which we notice is the vector field equivalent of Equation (4.6). We substitute in Equation (4.21) and then project. For this we require the rank-2 equivalent of Equation (4.8) which is

$$\nabla^\alpha A_{\alpha\mu} = \frac{1}{\alpha} D^\alpha \left(\alpha A_{\alpha\mu}\right) - n_\mu A_{\alpha\beta} K^{\alpha\beta} \tag{4.27}$$

So, proceeding with projecting Equation (4.15) we find

$$\partial_t E_i = \mathcal{L}_\beta E_i + \alpha m^2 X_i + \alpha D^j D_i X_j - \alpha D_i D^j X_j + D^j \alpha D_i X_j - D_j \alpha D^j X_i + \alpha K E_i \tag{4.28}$$

With this, we have found the equations of motion for the system, for both the first and second order fields as required.

4.4 Primary and Secondary Constraints

Throughout the process of deriving the equations of motion for the various fields, we discover new equations which do not contain second time derivatives. These are constraint equations as opposed to evolution equations; they do not describe how the field changes over time, but instead demand certain requirements to be kept on each hypersurface. The Proca field permits one primary constraint, which is a linear combination of the components of the equations of motion which do not contain second order time derivatives of the field A_μ.

Given N fields in a theory, we are only able to define $M < N$ equations of motion from the original Lagrangian, that is, equations which contain second order time derivatives of the fields. From these, we are able to construct a series of $N - M$ primary constraints by taking linear combinations of the M equations of motion which do not contain any second order time derivatives of the fields. For example with the scalar field case, we find no primary constraints as we only have one original field, ϕ, and managed to find a second order time derivative for it through obtaining $\partial_t \Pi$. Thus, $N = M = 1$, and so we are left with $N - M = 0$ primary constraints. For the Proca field, we have found only one acceleration via $\partial_t E_i$ out of two constituent fields X_μ and $\hat{X}$. Now, $N - M = 1$ and so there is therefore one primary constraint.

By demanding that the primary constraints are constant in time, we then find additional secondary constraints, and some of the missing accelerations. This process is iterated until we have found all the missing constraints and accelerations. See Buchbinder et al., 2000 for more details.

We can return to the derivation of the primary constraint for the Proca field. We begin with Equation (4.16), which we label $\mathcal{E}_\mu$ and equate the contents to this new labelling:

$$\mathcal{E}_\mu = \nabla^\alpha \nabla_\alpha A_\mu - \nabla^\alpha \nabla_\mu A_\alpha - m^2 A_\mu \ \ (= 0) \tag{4.29}$$

Following the methods of Buchbinder et al., 2000, we want to find linear combinations of these equations which contain no second order derivatives in time of the field A_μ. Thus, we want to find the terms which contain $\nabla_0 \nabla_0$, which in turn contain second order time derivatives, such that we can eliminate them. Here, the subscript 0 denotes specifically the zeroth component of a given object, and the equivalent applies for all of the other explicitly labelled indices.

Lowering the summed index above, we find:

$$\mathcal{E}_\mu = \left(g^{\alpha\beta} \delta^\lambda{}_\mu \nabla_\alpha \nabla_\beta - g^{\alpha\lambda} \nabla_\alpha \nabla_\nu \right) A_\lambda - m^2 A_\mu \tag{4.30}$$

Component by component, the equations of motion contain the following second order derivatives in time:

$$\mathcal{E}_0 = \left(g^{00} \delta^\lambda{}_0 - g^{0\lambda} \right) \nabla_0 \nabla_0 A_\lambda + \mathcal{O}\left(\nabla_0\right) \tag{4.31}$$

$$\mathcal{E}_i = g^{00} \delta^\lambda{}_i \nabla_0 \nabla_0 A_\lambda + \mathcal{O}\left(\nabla_0\right) \tag{4.32}$$

Wishing to eliminate the second time derivatives, notice the similarity between the terms when we take the following contractions with the metric:

$$g^{00} \mathcal{E}_0 = \left(g^{00} g^{00} \delta^\lambda{}_0 - g^{00} g^{0\lambda} \right) \nabla_0 \nabla_0 A_\lambda + \mathcal{O}\left(\nabla_0\right) \tag{4.33}$$

$$g^{0i} \mathcal{E}_i = g^{00} g^{0i} \delta^\lambda{}_i \nabla_0 \nabla_0 A_\lambda + \mathcal{O}\left(\nabla_0\right) \tag{4.34}$$

The first terms in each equation sum to $g^{00} g^{0\alpha} \delta^\lambda{}_\alpha \nabla_0 \nabla_0 A_\lambda$, and we notice that:

$$g^{00} g^{0\lambda} \nabla_0 \nabla_0 A_\lambda = g^{00} g^{0\alpha} \delta^\lambda{}_\alpha \nabla_0 \nabla_0 A_\lambda \tag{4.35}$$

Hence, the only linear combination of these equations of motion which eliminate all of the second order time derivatives is:

$$\mathcal{E}^0 = g^{00} \mathcal{E}_0 + g^{0i} \mathcal{E}_i \tag{4.36}$$

And therefore, the primary constraint of the system is:

$$\nabla^\alpha \nabla_\alpha A^0 - \nabla^\alpha \nabla^0 A_\alpha - m^2 A^0 = 0 \tag{4.37}$$

This is tricky to evaluate, as we now have specified components in the zero indices. We need to be careful about the evaluation of these components (i.e. setting $n^0 = \alpha^{-1}$) as we have covariant derivatives which make this operation complicated. As a rule of thumb, an index should never be 'selected' when acted upon by a covariant derivative, and instead, we exploit the metric compatibility to write the constraint as:

$$g^{0\beta}\left(\nabla^\alpha \nabla_\alpha A_\beta - \nabla^\alpha \nabla_\beta A_\alpha - m^2 A_\beta\right) = 0 \tag{4.38}$$

Then, using $g^{\alpha\beta} = \gamma^{\alpha\beta} - n^\alpha n^\beta$, the bracket can now be evaluated, substituting out the A_μ terms for the field strength tensor $F_{\mu\nu}$ to reduce this to a first-order derivative problem. This allows us to move the troublesome 0 index outside of the covariant derivatives, and convert it to n^0 using the definition of the metric (recalling that $\gamma^{0\mu} = 0$ as it is spatial).

Then, substituting out the field strength for its spatial decomposition, we come to the following

$$D^k E_k - m^2 \hat{X} = 0. \tag{4.39}$$

Which is the primary constraint for the Proca field. We are now presented with a choice. We have 'over-specified' the system, as we have both this constraint, and Equation (4.26) to dictate the value of $\hat{X}$. As with κ_μ in Section 4.2, we face the choice of either treating $\hat{X}$ as a dynamically evolving variable, or by having its value fixed through Equation (4.39). Either way is equivalent and so the choice is made for convenience.

We have not fully exhausted every different projection we can do. The other action we can perform on Equation (4.15) is to contract it with the normal vector. We expect this to yield a constraint from this operation as currently we have four degrees of freedom defined (one from $\hat{X}$ and three from X_μ), but expect only three in our system as we are fundamentally evolving a massive vector field. As the

system only permits one constraint, we expect that contracting Equation (4.15) with the normal vector and evaluating Equation (4.37) yields the same constraint. In general, the direct evaluation of the primary constraint is the more general method to find the constraints of the system.

4.5 Rank 2 - Tensor Field

The principles for finding the 3+1 equations of motion for the rank-2 field are the same as in Sections 4.2 and 4.3 - we take the equation of motion for the spin-2 field, then proceed down the two possible paths of either directly recasting it into a 3+1 form in terms of spatial fields, or by initially substituting in the decomposition of the field strength tensor in terms of its own constituent spatial fields, and then proceeding with the decomposition from there.

4.5.1 3+1 Equations of Motion for a Tensor Field

We consider the action describing a symmetric, massive, spin-2 field $H_{\mu\nu}$ with mass m in a four-dimensional Einstein spacetime (Buchbinder et al., 2000)[3]. The action for the field is

$$S = \int d^4x\sqrt{-g}\Big\{\frac{1}{4}\nabla_\mu H\nabla^\mu H - \frac{1}{4}\nabla_\mu H_{\nu\rho}\nabla^\mu H^{\nu\rho} - \frac{1}{2}\nabla^\mu H_{\mu\nu}\nabla^\nu H + \\ + \frac{1}{2}\nabla_\mu H_{\nu\rho}\nabla^\rho H^{\nu\mu} + \frac{1}{8}RH_{\mu\nu}H^{\mu\nu} + \frac{1}{8}RH^2 - \frac{m^2}{4}H_{\mu\nu}H^{\mu\nu} + \frac{m^2}{4}H^2\Big\}. \quad (4.40)$$

We denote the trace of the field by $H = H^\mu{}_\mu$. The variation of the action with respect to the field results in the following equation of motion(Buchbinder et al., 2000)

$$\nabla^\alpha\nabla_\alpha H_{\mu\nu} + 2R^\alpha{}_\mu{}^\beta{}_\nu H_{\alpha\beta} - m^2H_{\mu\nu} = 0. \quad (4.41)$$

The four primary constraints associated with this action are:

$$g^{00}\nabla_0\nabla_i H^i{}_\nu - g^{0i}\nabla_0\nabla_i H^0{}_\nu - g^{0i}\nabla_i\nabla_0 H^0{}_\nu - g^{ij}\nabla_i\nabla_j H^0{}_\nu - \\ - 2R^{\alpha0\beta}{}_\nu H_{\alpha\beta} + m^2H^0{}_\nu = 0. \quad (4.42)$$

[3]In this paper, there is an additional parameter ξ. Here, we have set this to 1.

As discussed in Section 4.4, we then find a series of secondary derivatives from the condition that the primary constraints are invariant over time. These are

$$H^{\mu}_{\ \mu} = 0, \tag{4.43}$$

$$\dot{H}^{\mu}_{\ \mu} = 0, \tag{4.44}$$

$$\nabla^{\mu} H_{\mu\nu} = 0. \tag{4.45}$$

These are nominally gauge conditions, but are upgraded to full constraints when considering a massive rank-2 field (see Brito, 2016 for a longer discussion). Now, I define a tensor

$$\Sigma_{\alpha\mu\nu} = \nabla_{\alpha} H_{\mu\nu} \tag{4.46}$$

in analogy with Ψ_{μ} in the scalar case and $F_{\mu\nu}$ in the vector case. This is an object which contains first derivatives of the field. Note the symmetry in the μ, ν pair of indices through the given definition. One can now substitute this into Equation (4.41) to find the following first-order differential equation

$$\nabla^{\alpha}\Sigma_{\alpha\mu\nu} + 2R^{\alpha\ \ \beta}_{\ \mu\ \ \nu} H_{\alpha\beta} - m^2 H_{\mu\nu} = 0. \tag{4.47}$$

Now one has the choice of how to decompose the 4-field $H_{\mu\nu}$. I could proceed by simply writing it as the most general decomposition of a rank-2 tensor, but can instead link it to the ADM (Arnowitt, Deser, and Misner, 1962) decomposition of general relativity. This is pertinent because we now have a rank-2 field evolving in a spacetime described itself by the metric - a rank-2 field. We need to distinguish therefore what constitutes the 'field' and what is the 'background' spacetime. In the limit of each component of $H_{\mu\nu}$ being much less than each component of $g_{\mu\nu}$, we can treat it as a perturbation to the metric, and so can use this as inspiration for the decomposition. The general ADM line element is

$$ds^2 = \left(-\alpha^2 + \beta_{\lambda}\beta^{\lambda}\right) dt^2 + \gamma_{ij}\left(\beta^j dx^i dt + \beta^i dx^j dt + dx^i dx^j\right). \tag{4.48}$$

Perturbing this results in

$$\delta(ds^2) = \left(-2\alpha\delta\alpha + 2\beta^{\lambda}\delta\beta_{\lambda}\right) dt^2 + 2\delta\beta_i dx^i dt + \delta\gamma_{ij} dx^i dx^j. \tag{4.49}$$

Writing this in matrix form

$$g_{\mu\nu} = \begin{pmatrix} -2\alpha\delta\alpha + 2\beta^i\delta\beta_i & \delta\beta_i \\ \delta\beta_j & \delta\gamma_{ij} \end{pmatrix}. \tag{4.50}$$

We recall Equation (4.18) and so can make a spatial decomposition for $H_{\mu\nu}$ taking into account its symmetry:

$$H_{\mu\nu} = h_{\mu\nu} + n_\mu \bar{h}_\nu + n_\nu \bar{h}_\mu + n_\mu n_\nu \hat{h} \tag{4.51}$$

Now, we want to try and compare Equation (4.51) somehow to Equation (4.50). We notice that in Equation (4.51), we have a scalar part, one vector part, and a tensor part. This means that it is possible to construct a 4x4 matrix out of these parts. This matrix is:

$$H_{\mu\nu} = \begin{pmatrix} n_0 n_0 \hat{h} & n_0 \bar{h}_i \\ n_0 \bar{h}_j & h_{ij} \end{pmatrix} \tag{4.52}$$

We can now make associations between Equations (4.52) and (4.50). We can first directly associate $\delta\gamma_{ij} = h_{ij}$, so the spatial part of the tensor field is simply the perturbation of the spatial metric. I also assign $n_0\bar{h}_i = -\alpha\bar{h}_i = \delta\beta_i$, and so re-scale the spatial vector $\bar{h}_i$ by a factor of $-1/\alpha$ to associate it with the perturbation of the shift vector. For the time component, we have $\alpha^2\hat{h} = -2\alpha\delta\alpha + 2\beta^i\delta\beta_i$. By absorbing the factor of two into the field, and ignoring the cross-mixing terms from the shift for simplicity, I then rescale $\hat{h}$ by $-1/\alpha$ as well. Therefore, the decomposition of the field from Equation (4.51) can be rewritten as:

$$H_{\mu\nu} = h_{\mu\nu} - \frac{1}{\alpha}\left(n_\mu \bar{h}_\nu + n_\nu \bar{h}_\mu + n_\mu n_\nu \hat{h}\right) \tag{4.53}$$

We can now find the equations of motion in the same manner as the scalar and vector field case. Starting with $\Sigma_{\alpha\mu\nu}$, its most general decomposition into spatial fields is:

$$\begin{aligned}\Sigma_{\alpha\mu\nu} = F_{\alpha\mu\nu} + n_\alpha B_{\mu\nu} + n_\mu A_{\alpha\nu} + n_\nu A_{\alpha\mu} + \\ + n_\mu n_\nu V_\alpha + n_\alpha n_\nu W_\mu + n_\alpha n_\mu W_\nu + n_\alpha n_\mu n_\nu \hat{\Sigma}\end{aligned} \tag{4.54}$$

It is important to note that the spatial field $A_{\mu\nu}$ is not symmetric due to the lack of symmetry in $\Sigma_{\alpha\mu\nu}$ in the α, μ and α, ν pairs of indices. For the same reason, $F_{\alpha\mu\nu}$ is only symmetric in μ, ν. The momentum $B_{\mu\nu}$ is symmetric however.

By inspecting Equation (4.54), we can see how these fields are related to $\Sigma_{\alpha\mu\nu}$. For example, consider acting with the projection operator on each index of $\Sigma_{\alpha\mu\nu}$. After substituting in Equation (4.54), we see that

$$\gamma^{\rho}{}_{i}\gamma^{\sigma}{}_{j}\gamma^{\beta}{}_{k}\Sigma_{\beta\rho\sigma} = \gamma^{\rho}{}_{i}\gamma^{\sigma}{}_{j}\gamma^{\beta}{}_{k}\left(F_{\beta\rho\sigma} + n_{\beta}B_{\rho\sigma} + n_{\rho}A_{\beta\sigma} + n_{\sigma}A_{\beta\rho} + ...\right) \tag{4.55}$$

$$= F_{kij}. \tag{4.56}$$

Therefore, by repeating this process, we see that the rest of the fields are defined in relation to $\Sigma_{\alpha\mu\nu}$ as

$$F_{kij} = \gamma^{\rho}{}_{i}\gamma^{\sigma}{}_{j}\gamma^{\beta}{}_{k}\Sigma_{\beta\rho\sigma}, \tag{4.57}$$

$$B_{ij} = -\gamma^{\rho}{}_{i}\gamma^{\sigma}{}_{j}n^{\beta}\Sigma_{\beta\rho\sigma}, \tag{4.58}$$

$$A_{ij} = -\gamma^{\beta}{}_{i}\gamma^{\rho}{}_{j}n^{\sigma}\Sigma_{\beta\rho\sigma}, \tag{4.59}$$

$$V_{i} = \gamma^{\beta}{}_{i}n^{\rho}n^{\sigma}\Sigma_{\beta\rho\sigma}, \tag{4.60}$$

$$W_{i} = \gamma^{\rho}{}_{i}n^{\beta}n^{\sigma}\Sigma_{\beta\rho\sigma}, \tag{4.61}$$

$$\hat{\Sigma} = -n^{\beta}n^{\rho}n^{\sigma}\Sigma_{\beta\rho\sigma}. \tag{4.62}$$

We now want to see the definitions of these fields in terms of $h_{ij}, \bar{h}_{i}$ and $\hat{h}$. We recall the definition that $\Sigma_{\alpha\mu\nu} = \nabla_{\alpha}H_{\mu\nu}$ from Equation (4.46), and so can substitute this into the equations above. For example, by performing this substitution in Equation (4.57), we see

$$F_{kij} = \gamma^{\rho}{}_{i}\gamma^{\sigma}{}_{j}\gamma^{\beta}{}_{k}\nabla_{\beta}H_{\sigma\rho} \tag{4.63}$$

$$= \gamma^{\rho}{}_{i}\gamma^{\sigma}{}_{j}\gamma^{\beta}{}_{k}\nabla_{\beta}\left(h_{\sigma\rho} - \frac{1}{\alpha}\left[n_{\sigma}\bar{h}_{\rho} + n_{\rho}\bar{h}_{\sigma} + n_{\sigma}n_{\rho}\hat{h}\right]\right) \tag{4.64}$$

$$= D_{k}h_{ij} + \frac{K_{ik}\bar{h}_{j}}{\alpha}, \tag{4.65}$$

where we have also used Equation (4.53) to substitute out $\nabla_\alpha H_{\mu\nu}$. By repeating this process first for F_{kij}, A_{ij}, and $\hat{\Sigma}$, we find the following:

$$F_{kij} = D_k h_{ij} + \frac{K_{jk}\bar{h}_i}{\alpha} + \frac{K_{ik}\bar{h}_j}{\alpha}, \tag{4.66}$$

$$A_{ij} = -\frac{D_i\bar{h}_j}{\alpha} + \frac{\bar{h}_j D_i\alpha}{\alpha^2} - K^k{}_i h_{jk} + \frac{K_{ij}\hat{h}}{\alpha}, \tag{4.67}$$

$$V_i = -\frac{D_i\hat{h}}{\alpha} + \frac{\hat{h}D_i\alpha}{\alpha^2} + \frac{2K^k{}_i\bar{h}_k}{\alpha}. \tag{4.68}$$

From these equations, we can see that F_{kij}, A_{ij}, and V_i do not contain Lie derivatives of the components of $H_{\mu\nu}$. Therefore, I choose to treat them as relabellings instead of dynamical variables and so can be substituted out as such. I now repeat the projection and contraction for the other fields:

$$\hat{\Sigma} = \frac{\mathcal{L}_n\hat{h}}{\alpha} + \frac{2\bar{h}^k D_k\alpha}{\alpha^2}, \tag{4.69}$$

$$W_i = \frac{\mathcal{L}_n\bar{h}_i}{\alpha} + \frac{\hat{h}D_i\alpha}{\alpha^2} - \frac{h_{ik}D^k\alpha}{\alpha} + \frac{K^k{}_i\bar{h}_k}{\alpha}, \tag{4.70}$$

$$B_{ij} = -\mathcal{L}_n h_{ij} + \frac{\bar{h}_i D_j\alpha}{\alpha^2} + \frac{\bar{h}_j D_i\alpha}{\alpha^2} - K_j{}^k h_{ik} - K_i{}^k h_{kj}. \tag{4.71}$$

Then, rearranging for the time derivatives we see that

$$\partial_t\hat{h} = \mathcal{L}_\beta\hat{h} + \alpha^2\hat{\Sigma} - 2\bar{h}^k D_k\alpha, \tag{4.72}$$

$$\partial_t\bar{h}_i = \mathcal{L}_\beta\bar{h}_i + \alpha^2 W_i - \hat{h}D_i\alpha + \alpha h_{ik}D^k\alpha - \alpha K^k{}_i\bar{h}_k, \tag{4.73}$$

$$\partial_t h_{ij} = \mathcal{L}_\beta h_{ij} - \alpha B_{ij} + \bar{h}_i D_j\ln\alpha + \bar{h}_j D_i\ln\alpha - \alpha K^k{}_j h_{ik} - \alpha K^k{}_i h_{kj}. \tag{4.74}$$

$\hat{\Sigma}$, W_i, and B_{ij} are the associated conjugate momenta of the respective fields but however, we shall see that $\hat{\Sigma}$ and W_i can be constrained by equations arising from the Lorentz condition in Equation (4.45). We can act on this equation with the projection operator and the normal vector, substitute $\nabla^\mu H_{\mu\nu}$ for $\Sigma^\mu{}_{\mu\nu}$ using Equation (4.46), and then expand in terms of the spatial components of $\Sigma_{\alpha\mu\nu}$ with Equations (4.66, 4.67, 4.68). One can equivalently expand $H_{\mu\nu}$ using Equation (4.53), and then substitute out the Lie derivatives of $\hat{h}$ and $\bar{h}_i$ which appear using

Equations (4.69) and (4.70). This produces

$$\hat{\Sigma} = -\frac{D^k \bar{h}_k}{\alpha} + \frac{\bar{h}_k D^k \alpha}{\alpha^2} + \frac{K\hat{h}}{\alpha} - K^{kl} h_{kl}, \tag{4.75}$$

$$W_i = D^k h_{ik} + \frac{K\bar{h}_i}{\alpha} + \frac{K^k{}_i \bar{h}_k}{\alpha}. \tag{4.76}$$

These equations therefore constrain $\hat{\Sigma}$ and W_i. We can do the same thing for the traceless condition by expanding Equation (4.43) and using Equation (4.53) to find

$$\hat{h} = -\alpha h^k{}_k, \tag{4.77}$$

which is a full constraint in the case of a massive rank-2 field. With Equation (4.77), one can optionally find an additional constraining evolution equation for $\hat{h}$, or simply directly fix its value. Therefore, the appropriate equations of motion for the components of $H_{\mu\nu}$, having used Equations (4.75) and (4.76) are

$$\partial_t \hat{h} = \mathcal{L}_\beta \hat{h} - D^k \left(\alpha \bar{h}_k\right) + \alpha K \hat{h} - \alpha^2 K^{kl} h_{kl}, \tag{4.78}$$

$$\partial_t \bar{h}_i = \mathcal{L}_\beta \bar{h}_i + \alpha D^k \left(\alpha h_{ik}\right) - \hat{h} D_i \alpha + \alpha K \bar{h}_i, \tag{4.79}$$

$$\partial_t h_{ij} = \mathcal{L}_\beta h_{ij} - \alpha B_{ij} + \bar{h}_i D_j \ln\alpha + \bar{h}_j D_i \ln\alpha - \alpha K^k{}_j h_{ik} - \alpha K^k{}_i h_{kj}. \tag{4.80}$$

Now, the goal is to find the equation of motion for B_{ij} in a similar way to the scalar and vector cases. Here, I constrain $\hat{\Sigma}$ and W_i directly with Equations (4.75) and (4.76) and as such they do not need evolution equations. We will need another extension to Equations (4.8) and (4.27), which is

$$\nabla^\alpha F_{\alpha\mu\nu} = \frac{1}{\alpha} D^\alpha \left(\alpha F_{\alpha\mu\nu}\right) - n_\mu F_{\alpha\beta\nu} K^{\alpha\beta} - n_\nu F_{\alpha\mu\beta} K^{\alpha\beta}. \tag{4.81}$$

As a final step before finding the equations of motion for B_{ij}, consider the second term in Equation (4.47). The Riemann curvature tensor in this equation is the 4-dimensional version, and so needs to be written in terms of 3-dimensional

counterparts. This is

$$
\begin{aligned}
{}^{(4)}R_{\alpha\mu\beta\nu} = {}^{(3)}R_{\alpha\mu\beta\nu} - K_{\alpha\nu}K_{\mu\beta} + K_{\alpha\beta}K_{\mu\nu} - K^{\lambda}{}_{\mu}K_{\nu\lambda}n_{\alpha}n_{\beta} + K^{\lambda}{}_{\lambda}K_{\nu\mu}n_{\alpha}n_{\beta} + \\
+ R_{\nu\mu}n_{\alpha}n_{\beta} + K^{\lambda}{}_{\alpha}K_{\nu\lambda}n_{\beta}n_{\mu} - K^{\lambda}{}_{\lambda}K_{\nu\alpha}n_{\beta}n_{\mu} - R_{\nu\alpha}n_{\beta}n_{\mu} + K^{\lambda}{}_{\mu}K_{\beta\lambda}n_{\alpha}n_{\nu} - \\
- K^{\lambda}{}_{\lambda}K_{\beta\mu}n_{\alpha}n_{\nu} - R_{\beta\mu}n_{\alpha}n_{\nu} - K^{\lambda}{}_{\alpha}K_{\beta\lambda}n_{\mu}n_{\nu} + K^{\lambda}{}_{\lambda}K_{\beta\alpha}n_{\mu}n_{\nu} + R_{\beta\alpha}n_{\mu}n_{\nu} + \\
+ n_{\nu}D_{\alpha}K_{\mu\beta} - n_{\beta}D_{\alpha}K_{\mu\nu} + n_{\mu}D_{\beta}K_{\alpha\nu} - n_{\alpha}D_{\beta}K_{\mu\nu} - n_{\nu}D_{\mu}K_{\alpha\beta} + \\
+ n_{\beta}D_{\mu}K_{\alpha\nu} - n_{\mu}D_{\nu}K_{\alpha\beta} + n_{\alpha}D_{\nu}K_{\mu\beta}. \quad (4.82)
\end{aligned}
$$

Starting from Equation (4.47), one substitutes in Equation (4.54) and projects both free indices using the projection operator to find

$$
\begin{aligned}
\partial_t B_{ij} = \mathcal{L}_{\beta}B_{ij} + \alpha m^2 h_{ij} - 2\alpha h^{kl}R_{ikjl} + 2\hat{h}R_{ij} - D_k h_{ij}D^k\alpha - D^k h_{ik}D_j\alpha - \\
- D^k h_{jk}D_i\alpha + 2KK_{ij}\hat{h} + B_{ij}K\alpha - B_j{}^k K_{ik}\alpha - B_i{}^k K_{jk}\alpha - 2K^{kl}K_{ij}h_{kl}\alpha + \\
+ 2K_i{}^k K_j{}^l h_{kl}\alpha - K_k{}^l K_j{}^k h_{il}\alpha - K_k{}^l K_i{}^k h_{jl}\alpha - \bar{h}_j D_k K_i{}^k + 4\bar{h}^k D_k K_{ij} - \\
- \bar{h}_i D_k K_j{}^k - \alpha D_k D^k h_{ij} - 2K_{jk}D^k\bar{h}_i - 2K_{ik}D^k\bar{h}_j + \frac{K_{jk}\bar{h}_i D^k\alpha}{\alpha} + \frac{K_{ik}\bar{h}_j D^k\alpha}{\alpha} - \\
- 2\bar{h}^k D_i K_{jk} - 2\bar{h}^k D_j K_{ik} - 2K_{ij}K^{kl}h_{kl}\alpha - \frac{K^k{}_j\bar{h}_k D_i\alpha}{\alpha} - \frac{K^k{}_i\bar{h}_k D_j\alpha}{\alpha} - \\
- \frac{K\bar{h}_j D_i\alpha}{\alpha} - \frac{K\bar{h}_i D_j\alpha}{\alpha}. \quad (4.83)
\end{aligned}
$$

Finally, we need to determine the constraints of the system. We have already seen that the transverse and traceless gauges are upgraded to constraints when considering massive fields, so we now consider the four primary constraints of the system, seen in Equation (4.42).

A slight difference is with the 'selected' indices appearing in the equation, i.e., the components which I have chosen to be zero or purely spatial. In this case, I 'move' these indices onto Kronecker delta symbols, i.e. $W_i = \delta^{\alpha}{}_{i}W_{\alpha}$, which are then compatible with the covariant derivative and so can be taken outside of the derivative. Then, I rewrite the Kronecker deltas in terms of projection operators and normal vectors. This is done to remove the ambiguity about when to substitute in the specified components, for example, $n_0 = -\alpha$, as doing this before or after resolving a covariant derivative can lead to inconsistencies.

We also need to take care with the covariant derivatives as we can accidentally reintroduce time derivatives of the fields, which we do not want in the constraints. We therefore commute covariant derivatives, of the form $\nabla_0\nabla_i H^{\cdots}{}_{\cdots}$ to $\nabla_i\nabla_0 H^{\cdots}{}_{\cdots}$. This is because when written in terms of Σ_{kij} and then expanded, $\nabla_i\Sigma_0{}^{\cdots}{}_{\cdots}$ does not contain second order time derivatives while $\nabla_0\Sigma_i{}^{\cdots}{}_{\cdots}$ does. After these precautions, we can then find the primary scalar and vector constraints. Recalling the primary constraints from Equation (4.42), I find the 3+1 forms. The primary scalar constraint is

$$m^2\hat{h} + \alpha h^{ij(3)}R_{ij} + \hat{h}^{(3)}R - \alpha D^i D^j h_{ij} + 2D_i\hat{h}D^i\ln\alpha - 2\hat{h}D_i(\ln\alpha)D^i(\ln\alpha) - \\ - D_i D^i\hat{h} + \frac{1}{\alpha}\hat{h}D_i D^i\alpha = 0, \quad (4.84)$$

and the primary vector constraint is

$$m^2\bar{h}_i - \bar{h}^{j(3)}R_{ij} + \bar{h}_i{}^{(3)}R - \alpha D^j B_{ij} + 2D_j\bar{h}_i D^j\ln\alpha - 2\bar{h}_i D_j(\ln\alpha)D^j(\ln\alpha) - \\ - D^j D_j\bar{h}_i + \frac{1}{\alpha}\bar{h}_i D^j D_j\alpha = 0. \quad (4.85)$$

In summary, the 3+1 equations of motion for a massive rank-2 tensor field are

$$\partial_t\hat{h} = \mathcal{L}_\beta\hat{h} - D^k\left(\alpha\bar{h}_k\right) + \alpha K\hat{h} - \alpha^2 K^{kl}h_{kl}, \quad (4.86)$$

$$\partial_t\bar{h}_i = \mathcal{L}_\beta\bar{h}_i + \alpha D^k\left(\alpha h_{ik}\right) - \hat{h}D_i\alpha + \alpha K\bar{h}_i, \quad (4.87)$$

$$\partial_t h_{ij} = \mathcal{L}_\beta h_{ij} - \alpha B_{ij} + \bar{h}_i D_j\ln\alpha + \bar{h}_j D_i\ln\alpha - \alpha K^k{}_j h_{ik} - \alpha K^k{}_i h_{kj}, \quad (4.88)$$

$$\partial_t B_{ij} = \mathcal{L}_\beta B_{ij} + \alpha m^2 h_{ij} - 2\alpha h^{kl}R_{ikjl} + 2\hat{h}R_{ij} - D_k h_{ij}D^k\alpha - D^k h_{ik}D_j\alpha - \\ - D^k h_{jk}D_i\alpha + 2KK_{ij}\hat{h} + B_{ij}K\alpha - B_j{}^k K_{ik}\alpha - B_i{}^k K_{jk}\alpha - 2K^{kl}K_{ij}h_{kl}\alpha + \\ + 2K_i{}^k K_j{}^l h_{kl}\alpha - K_k{}^l K_j{}^k h_{il}\alpha - K_k{}^l K_i{}^k h_{jl}\alpha - \bar{h}_j D_k K_i{}^k + 4\bar{h}^k D_k K_{ij} - \\ - \bar{h}_i D_k K_j{}^k - \alpha D_k D^k h_{ij} - 2K_{jk}D^k\bar{h}_i - 2K_{ik}D^k\bar{h}_j + \frac{K_{jk}\bar{h}_i D^k\alpha}{\alpha} + \frac{K_{ik}\bar{h}_j D^k\alpha}{\alpha} - \\ - 2\bar{h}^k D_i K_{jk} - 2\bar{h}^k D_j K_{ik} - 2K_{ij}K^{kl}h_{kl}\alpha - \frac{K^k{}_j\bar{h}_k D_i\alpha}{\alpha} - \frac{K^k{}_i\bar{h}_k D_j\alpha}{\alpha} - \\ - \frac{K\bar{h}_j D_i\alpha}{\alpha} - \frac{K\bar{h}_i D_j\alpha}{\alpha}. \quad (4.89)$$

The constraints are

$$\hat{h} = -\alpha h^k{}_k, \tag{4.90}$$

$$m^2\hat{h} + \alpha h^{ij\,(3)}R_{ij} + \hat{h}^{(3)}R - \alpha D^i D^j h_{ij} + 2D_i\hat{h}D^i \ln\alpha - 2\hat{h}D_i(\ln\alpha)D^i(\ln\alpha) - \\ - D_i D^i\hat{h} + \frac{1}{\alpha}\hat{h}D_i D^i\alpha = 0, \tag{4.91}$$

$$m^2\bar{h}_i - \bar{h}^{j\,(3)}R_{ij} + \bar{h}_i{}^{(3)}R - \alpha D^j B_{ij} + 2D_j\bar{h}_i D^j \ln\alpha - 2\bar{h}_i D_j(\ln\alpha)D^j(\ln\alpha) - \\ - D^j D_j\bar{h}_i + \frac{1}{\alpha}\bar{h}_i D^j D_j\alpha = 0. \tag{4.92}$$

4.5.2 Gravitational Wave Solutions and Scattering

Now that the formalism has been developed, I now present some examples of its use, starting with gravitational waves. Gravitational waves can be treated as linear perturbations of the background flat spacetime metric, that is:

$$g_{ab} = \eta_{ab} + h_{ab} \tag{4.93}$$

Here, η_{ab} is the flat Minkowski metric, and h_{ab} is the linear perturbation. Following for example, the steps laid out in Baumgarte and Shapiro, 2010, we define the trace-reversed version of the perturbation:

$$\bar{h}_{ab} \equiv h_{ab} - \frac{1}{2}\eta_{ab}h^c{}_c \tag{4.94}$$

And impose the Lorentz gauge:

$$\nabla^a\bar{h}_{ab} = 0 \tag{4.95}$$

With these defined, the vacuum Einstein's equations, i.e. Equation (1.13), become:

$$\nabla^c\nabla_c\bar{h}_{ab} = 0 \tag{4.96}$$

Lastly, we use the remaining gauge freedoms to impose the transverse-traceless gauge, or TT gauge as follows:

$$\bar{h}_{0a} = 0 \tag{4.97}$$

$$\bar{h}^a{}_a = 0 \tag{4.98}$$

Equation (4.96) is the equation of motion for this perturbative gravitational wave. This can be solved exactly in many different analytic contexts, but an interesting problem is to be able to find the solution of a gravitational wave in a fully-general background. In this case, we can return to methods associated with numerics, specifically, fixed-background evolution. It is well known that gravitational waves can be described as a massless rank-2 field, with the two independent components being the magnitude of the 'plus' and 'cross' polarisation modes of the strain. We can model these modes as linear perturbations of a background metric in order to simulate them in arbitrary spacetimes.

Looking back at Equation (4.93), a different interpretation we can make is that this represents a matter field evolving on top of a background. This newly-interpreted version for a full spacetime metric g_{ab} is therefore:

$$g_{ab} = g'_{ab} + H_{ab} \tag{4.99}$$

Where g'_{ab} is the 'background' metric and H_{ab} is the rank-2 tensor field. As found in Section 4.5.1, Equations (4.78, 4.79, 4.80) are the evolution equations for this field. In this massless case, $m = 0$. We want to consider how to draw analogies between the gravitational wave strain tensor and the tensor field we are simulating. In the TT gauge we imposed for gravitational waves, i.e. Equations (4.97, 4.98), the gravitational wave strain for a wave propagating in the z direction in Minkowski spacetime is

$$\bar{h}_{\mu\nu} = \begin{pmatrix} 0 & 0 & 0 & 0 \\ 0 & h_+ & h_\times & 0 \\ 0 & h_\times & -h_+ & 0 \\ 0 & 0 & 0 & 0 \end{pmatrix}. \tag{4.100}$$

We can conceive in the language of 3+1, and divide it into the scalar, vector, and tensor components which evolve as in Equations (4.78, 4.79, 4.80). From this, we can see that the transverse part of the gauge implies that $\hat{h}$ and $\bar{h}_i$ should be set to zero, thus leaving h_{ij} as the only non-zero first order evolution variable and thus representing the lower right hand block of the original gravitational wave strain. From here, we have the ability to set the remaining components of h_{ij} freely, ensuring

that it follows the gauges set above. We can then give the wave its initial momentum by setting the components of the second order, momentum tensor to be the first time derivatives of the appropriate components of h_{ij}, that is $B_{11} = \partial_t h_{11},\ B_{12} = \partial_t h_{12} \ldots$. Overall then, the evolution equations for the system are

$$\partial_t h_{ij} = \mathcal{L}_\beta h_{ij} - \alpha B_{ij} - \alpha K^k{}_j h_{ik} - \alpha K^k{}_i h_{kj}, \tag{4.101}$$

and

$$\begin{aligned}\partial_t B_{ij} = \mathcal{L}_\beta B_{ij} - 2\alpha h^{kl} R_{ikjl} - D_k h_{ij} D^k \alpha - D^k h_{ik} D_j \alpha - D^k h_{jk} D_i \alpha + \\ + B_{ij} K^k{}_k \alpha - B_j{}^k K_{ik} \alpha - B_i{}^k K_{jk} \alpha - 2K^{kl} K_{ij} h_{kl} \alpha + \\ + 2K_i{}^k K_j{}^l h_{kl} \alpha - K_k{}^l K_j{}^k h_{il} \alpha - K_k{}^l K_i{}^k h_{jl} \alpha - \alpha D_k D^k h_{ij}.\end{aligned} \tag{4.102}$$

This looks complex still, but can be simplified if we consider spacetimes with no cross-terms in the metric. Spacetimes with these properties have no extrinsic curvature, so $K_{ij} = 0$. In this case, the equations reduce to

$$\partial_t h_{ij} = \mathcal{L}_\beta h_{ij} - \alpha B_{ij}, \tag{4.103}$$

and

$$\partial_t B_{ij} = \mathcal{L}_\beta B_{ij} - 2\alpha h^{kl} R_{ikjl} - \alpha D_k D^k h_{ij} - D_k h_{ij} D^k \alpha - D^k h_{ik} D_j \alpha - D^k h_{jk} D_i \alpha. \tag{4.104}$$

While the choice of setting $\hat{h}$ and $\bar{h}_i$ above was inspired by waves propagating in flat spacetime, we can still make this choice for more general spacetimes by ensuring that whatever initial data select for h_{ij} and B_{ij} obeys all the constraint equations. As gravitational waves only have these two modes, we do not expect that $\hat{h}$ and $\bar{h}_i$ become sourced.

According to Equation (4.99), we can treat gravitational waves, here represented by a massless rank-2 field, as a perturbation on top of a general metric, such as a black hole solution. It is possible to find an equation of motion for these perturbations of black hole spacetimes, and therefore, using numerical methods, to be able to study the general evolution of gravitational waves in black hole

spacetimes such as in the work done by He and Wu, 2022. In this work, they start from the equations of motion for spacetime in the ADM formalism - Equations (1.71) and (1.72) - and directly perturb them to find the equations of motion for a perturbation. I verify the results of this work by instead using the formalism described before of a general rank-2 tensor field evolving on a background spacetime found independently from any perturbation.

To proceed, I choose the isotropic Schwarzschild line metric to be the background spacetime. This is because the conformality of the metric in the spatial, Cartesian coordinates makes it easier to set 'plane' initial data. The isotropic Schwarzschild line element is:

$$\mathrm{d}s^2 = -\left(\frac{1-\frac{M}{2r}}{1+\frac{M}{2r}}\right)^2 \mathrm{d}t^2 + \left(1+\frac{M}{2r}\right)^4 \left(\mathrm{d}x^2+\mathrm{d}y^2+\mathrm{d}z^2\right) \tag{4.105}$$

The equations of motion for the system are Equations (4.103) and (4.104). Far away from the black hole, we are in flat Minkowski spacetime to a high degree of approximation, as we can deduce by inspecting Equation 4.105 as we increase r. Therefore, I set initial conditions for the gravitational wave to be any function of my choosing. To verify the work of He and Wu, 2022, I therefore choose the initial conditions to be a sinusoidal wave packet modulated by a Gaussian so that

$$h_{ij} = \begin{pmatrix} A\sin(\omega z)e^{-(z-\beta)^2/2} & 0 & 0 \\ 0 & -A\sin(\omega z)e^{-(z-\beta)^2/2} & 0 \\ 0 & 0 & 0 \end{pmatrix}, \tag{4.106}$$

and where $B_{11} = -B_{22} = A\left(\omega\cos\left(\omega z\right) - \left(z-\beta\right)\sin\left(\omega z\right)\right)e^{-(z-\beta)^2/2}$.

For simplicity, here I choose to only populate the plus modes. I then run simulations using GRDzhadzha with these initial data.

Figure 4.1 shows a series of two-dimensional slices of the simulation on the $x-z$ plane at various time steps, with the central black hole drawn in the middle of each. In the top panel, we see how the wave propagates along the negative z direction. By the middle panel, the wave begins to be 'dragged' around the black hole, with the wave front being more strongly bent at lower impact parameters. We can see this as a kind of friction-like effect, where the wavefront is delayed compared to the

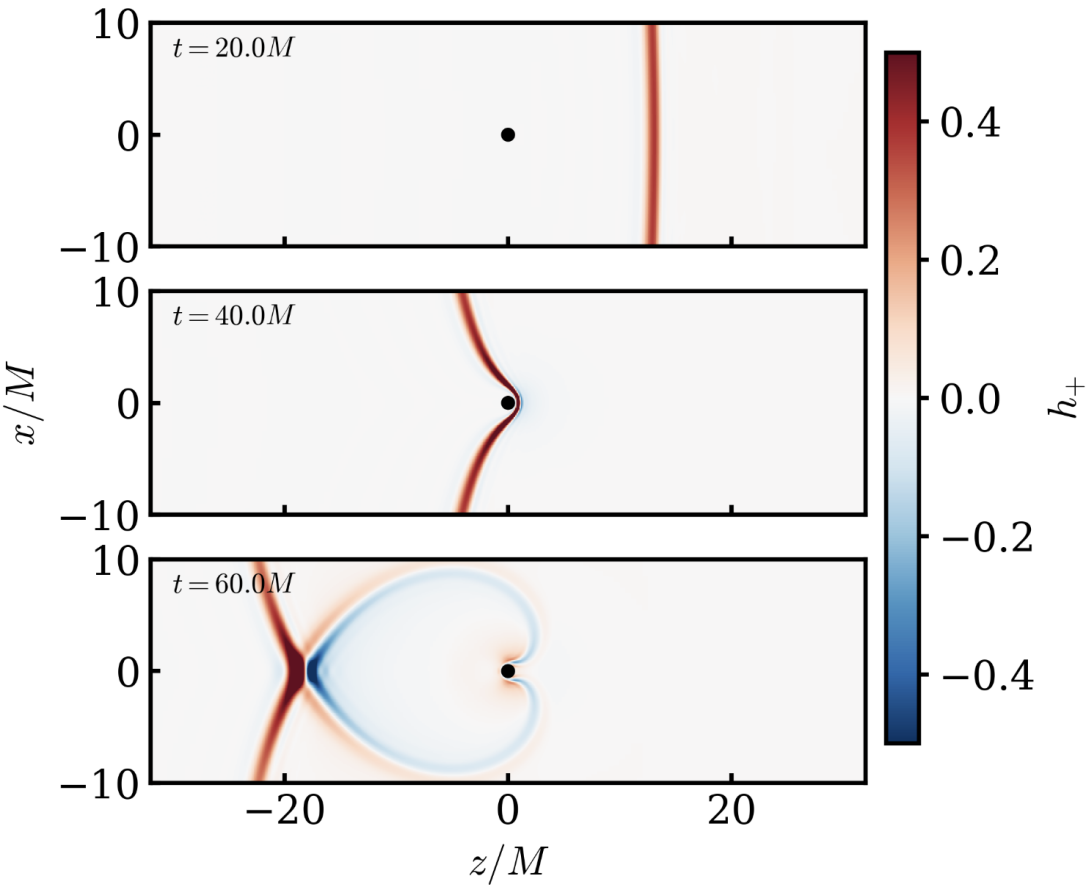


Figure 4.1: Simulation of a gravitational wave scattering off a central Schwarzschild black hole. The panels, top to bottom, show the simulation at progressively later time steps. The colour of the data shows the amplitude of the h_+ mode.

mostly undisturbed sections of the wave at larger impact parameters. Additionally, we see that the wave increases in amplitude close to the black hole. In the bottom panel, the wave has continued to propagate, becomes more deformed, and further increases in amplitude on the central propagation axis. There also now appears to be two main parts of the wave - there is the initial wave front of positive h_+ which continues to propagate in the negative z direction, and then a 'heart-shaped' wake behind the initial wavefront, propagating in all directions. It is also interesting to note how for a section of this wake, the overall sign of the field has changed to negative. This behaviour of the wave is also seen in the work of He and Wu, 2022.

There are many extensions which can be made for this work. It would be interesting to calculate the momentum transfer from the wave to the black hole

to see how much of a 'kick' it receives, and how this might affect the overall wave. Additionally, there are different potential observational signatures associated with this scenario. By inspecting Figure 4.1, we already see how the deformation and change in amplitude of the wave could potentially be detectable, as well as the secondary wake changing sign entirely. Under further study and comparison with other scenarios, it would be interesting to see if these features of the scattered wavefront could serve to 'fingerprint' and so identify these events in the real Universe.

4.5.3 Tensor Fields on Taub Spacetime

I also consider the case of the Taub metric. This metric is a vacuum, static, plane-symmetric solution to the Einstein field equations. The line element is as follows:

$$\mathrm{d}s^2 = z^{-2/3}\mathrm{d}t^2 - z^{4/3}\left(\mathrm{d}x^2 + \mathrm{d}y^2\right) - \mathrm{d}z^2 \tag{4.107}$$

This is a simple metric whose change in geometry is solely in the z direction, and so in effect acts at a 'ramp', with spacetime becoming more and more curved away from the $z = 0$ plane of origin. As a result, it is an interesting spacetime to test simulations on, with more interesting phenomenology possible than Minkowski space, yet being less complicated than full black hole spacetimes. Using intuition from gravitational wave solutions, I choose a solution for the initial data of the form

$$\bar{h}_{\mu\nu} = \begin{pmatrix} 0 & 0 & 0 & 0 \\ 0 & h_+(t,z) & h_\times(t,z) & 0 \\ 0 & h_\times(t,z) & -h_+(t,z) & 0 \\ 0 & 0 & 0 & 0 \end{pmatrix}. \tag{4.108}$$

Here, h_+ and $h_\times$ are be functions of t and z, so they can be solved for a general initial solution. Note that we don't need to consider functional dependence in the x-y plane as the Taub metric is simply the Minkowski metric in this case. By substituting this into Equation (4.41) and calculating all the geometric objects with the Taub metric, one finds

$$\left(\frac{16}{9z^2} - m^2\right) h_+(t,z) - \frac{5\partial_z h_+(t,z)}{3z} + \partial_z^2 h_+(t,z) - z^{2/3}\partial_t^2 h_+(t,z) = 0, \tag{4.109}$$

$$\left(\frac{16}{9z^2} - m^2\right) h_\times(t,z) - \frac{5\partial_z h_\times(t,z)}{3z} + \partial_z^2 h_\times(t,z) - z^{2/3}\partial_t^2 h_\times(t,z) = 0. \tag{4.110}$$

As can be seen, Equations (4.109) and (4.110) are wave equations themselves. As a first example, one can solve a massless, time independent version of these equations to find $h_+ = h_\times \sim z^{4/3}$. We can also find a propagating wave solution. For simplicity, as the equations for the two modes are identical, they can be denoted jointly by h_A. Before proceeding, these equations can be simplified. By making the coordinate transformation $\mathrm{d}z_* = z^{1/3}\mathrm{d}z$, and in the massless case, we have

$$-\frac{h_A}{z_*^2} + \frac{\partial_{z_*} h_A}{z_*} - \partial_{z_*}^2 h_A + \partial_t^2 h_A = 0. \tag{4.111}$$

Multiplying through by $-z_*^2$, this becomes

$$z_*^2 \partial_{z_*}^2 h_A - z_* \partial_{z_*} h_A + h_A + z_*^2 \partial_t^2 h_A = 0. \tag{4.112}$$

This is remarkably close to the general form of Bessel's equation. To continue, we can Fourier transform the above such that $\partial_t^2 h_A = -\omega^2 h_A^2$ where ω is the frequency of the wave, producing

$$z_*^2 \partial_{z_*}^2 h_A - z_* \partial_{z_*} h_A + h_A - \omega^2 z_*^2 h_A = 0. \tag{4.113}$$

The solution to this equation is a combination of first order Bessel functions with prefactors like so

$$h_A(t, z_*) = A(z_* - t) J_0(\omega(z_* - t)) + B(z_* - t) Y_0(\omega(z_* - t)). \tag{4.114}$$

Here, J_0 and Y_0 are zeroth order Bessel functions of the first and second kind respectively, and A and B are arbitrary constants. Freely being able to choose the values of A and B, one sets $A = 1$ and $B = 0$ to find the initial conditions for a wave on Taub spacetime in 3+1 form as

$$h_{ij} = \begin{pmatrix} z_* J_0(\omega z_*) & z_* J_0(\omega z_*) & 0 \\ z_* J_0(\omega z_*) & -z_* J_0(\omega z_*) & 0 \\ 0 & 0 & 0 \end{pmatrix}. \tag{4.115}$$

As previously mentioned, the initial momentum of the system is the time derivative of the spatial field, evaluated at $t = 0$. Note there there is some flexibility here in the choice for the momentum, namely in which direction we wish the field to propagate in. Inspecting Equation (4.114), I choose a solution which propagates in the positive

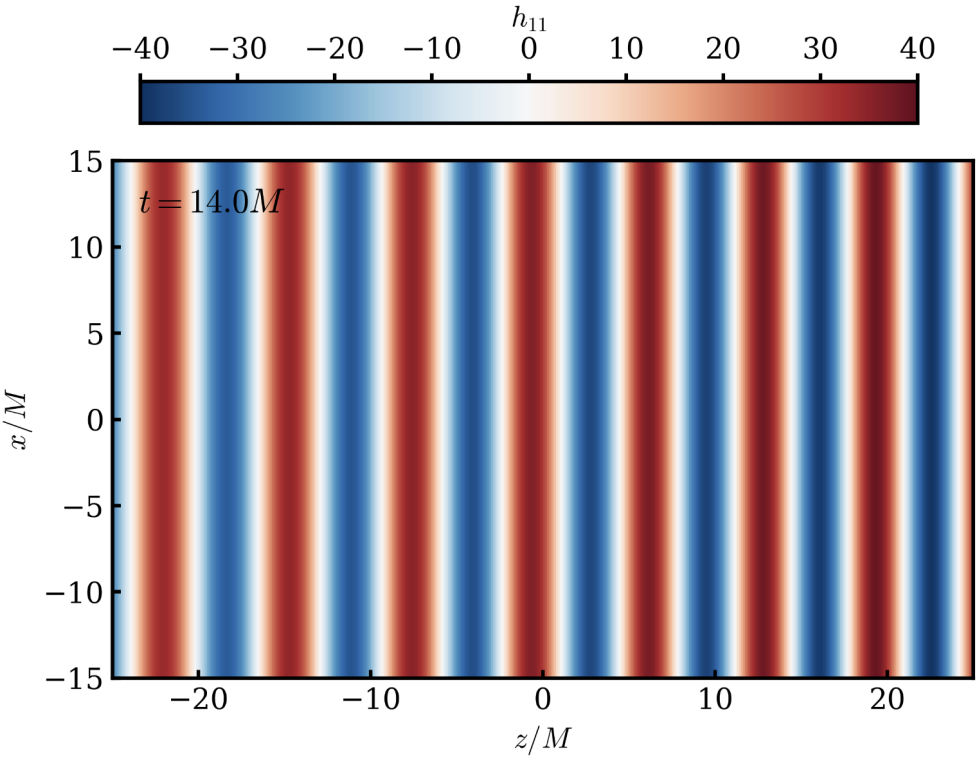


Figure 4.2: Simulation of a Bessel function wave in Taub spacetime on the $x - z$ plane at simulation time $t = 14M$. The colour of the plot shows the amplitude of h_{11}.

z_* direction, but could equally have chosen the negative z_* direction instead. Taking the time derivative therefore multiplies the overall momentum by a factor of ± 1 depending on the choice we make, and as the initial conditions are always evaluated for $t = 0$, it effectively means we can freely change the overall sign of the momentum depending on the direction we want the solution to initially travel in. So, the initial momentum for the components of the Taub wave is $\pm\left(z_* J_0(\omega z_*) - z_* J_1(\omega z_*)\right)$ where the overall sign depends on the component of h_{ij} and the direction in which the wave is travelling. Here, $J_1(\omega z_*)$ is a first-order Bessel function of the first kind, where $\partial_x J_0(Ax) = A J_1(Ax)$. The equations of motion for the spatial fields are Equations (4.103) and (4.104) as with the gravitational wave scattering case.

I ran simulations with this initial configuration, but with an overall coordinate shift applied in the z direction to the initial wave. Results are shown in Figure 4.2 and Figure 4.3. Figure 4.2 shows a slice of the field on the $x - z$ plane at a time step after the beginning of the simulation, where the colour of the field shows the

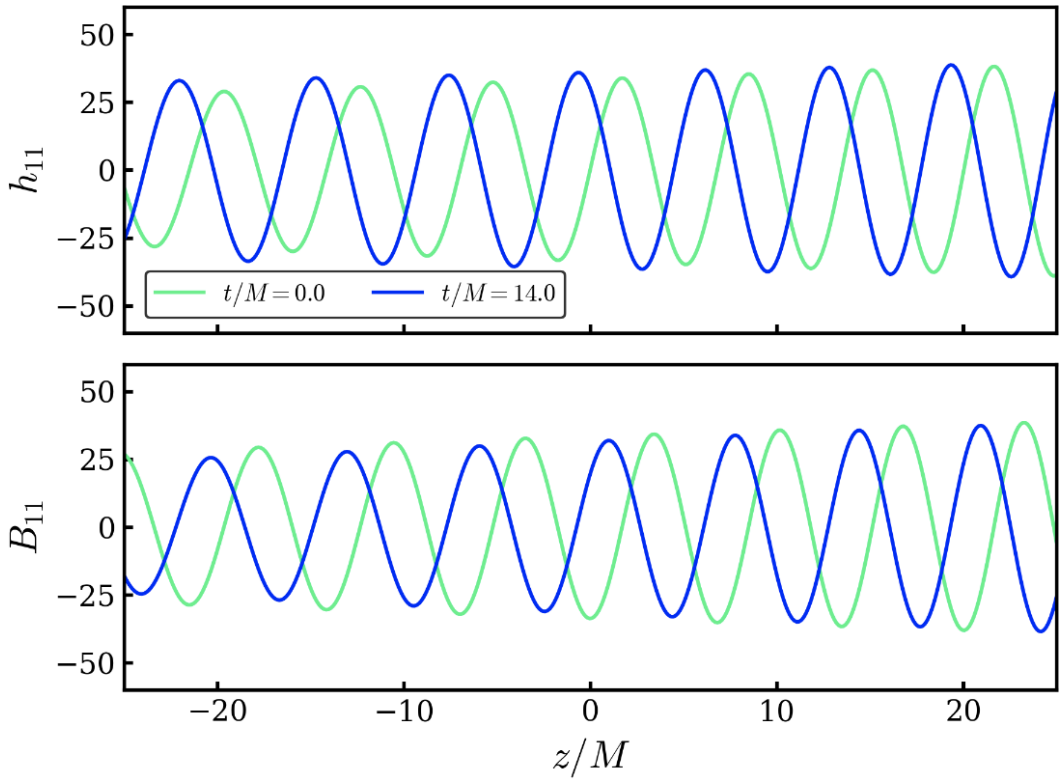


Figure 4.3: One-dimensional version of Figure 4.2, with added panel for conjugate momentum component B_{11}. The two different coloured lines show the simulation at times $t = 0M$ and $t = 14M$ respectively.

amplitude of the h_{11} component. One can see the symmetry along the x axis, and the various wavefronts along the z axis. Figure 4.3 shows this same field alongside conjugate momentum B_{11} but now at two different time steps and with the x axis suppressed. One can see more clearly the peaks of the Bessel function wave and their decreasing amplitude in the negative z direction. We see how the wave is propagating in the negative z direction, but that the behaviour for the field and the momentum is different. The momentum at both time steps shows the same overall behaviour with the amplitude of its peaks - decrease in the negative z direction - and the wave at the later time step fitting within the envelope of the first. It is interesting to note however that for the h_{11} component, this does not hold. The amplitude still decreases to the left of the plot, but the amplitude of the peaks at $t = 14M$ increases relative to those same peaks but at $t = 0$. This highlights the interesting geometry involved in Taub spacetime.

4.5.4 Future Work

Further projects with this tensor formalism include the simulation of spin-2 superradiance. As discussed in Section 1.3, tensor fields are compelling objects of study due to the shorter timescales on which superradiant instabilities occur for them compared to scalar and vector fields. Recently, superradiance has been simulated for rank-2 fields East and Siemonsen, 2023 thus opening up a wide and interesting field of study and motivating the development of various frameworks to simulate these fields in high energy environments. One can therefore verify the various rates calculated in these works using an independent method. Furthermore, as this requires dynamic spacetime, it would use the full toolkit of numerical relativity and so pose a rewarding challenge to ensure that the equations of motion I derived behave in these evolving spacetimes. This would likely involve the testing of the hyperbolicity of equations of motion, and so in the process revealing potential improvements which can be made. Additionally, it could be possible study various models of massive gravity and massive gravitational waves using this framework.

Additionally, it would be interesting to follow the work of Chapters 2 and 3 by investigating the effects that accretion around a black hole has on the phenomenology of a massive spin-2 field. One can then consider different models of spin-2 particles with different potentials to see how this changes their behaviour. This would be more general than the gravitational wave scattering scenario, as it tests the evolution of all components of the field - not just those which are relevant for the propagation of gravitational waves. This is all made more compelling due to the status of massive rank-2 fields as dark matter candidates (Babichev et al., 2016; Chu and Garcia-Cely, 2017; Manita et al., 2023). By understanding their behaviour in different environments and eventually calculating various observables, one can contribute to the discussion of their potential viability as dark matter candidates and even methods for detection and discerning between different possible models.

"I'm really very sorry for you all, but it's an unjust world, and virtue is triumphant only in theatrical performances."

—W.S Gilbert
The Mikado

5 Conclusion

The work I have presented in this thesis represents my investigations into the behaviour of fundamental fields in curved spacetime. Firstly, I presented the work done on the accretion of scalar field dark matter around black holes in Chapters 2 and 3. We focused on the introducing quartic self-interactions and other higher order terms into the standard quadratic models of wave-like dark matter to study the differences in behaviour these additions to the potential cause when such dark matter is excited to higher densities. To do this, we used the GRDzhadzha software (Aurrekoetxea et al., 2024b), to simulate the accretion of an initially homogenous, infinite cloud of this modified wave-like dark matter onto a Schwarzschild black hole.

In Chapter 2, we were concerned with models of particles with additional quartic ($\sim \lambda\phi^4$) contributions to the quadratic potential, where λ is the self-interaction coupling strength parameter. Particles with different signs and values of this parameter show interesting, different phenomenology. A positive parameter makes the potential well steeper, while a negative one introduces a turnover. The relative contributions between the two terms therefore creates this set of regimes where either the quadratic or quartic part of the potential dominates depending on λ. We showed how the evolution of the accreted field is the same in these scenarios until a transition between regimes is reached. For $\lambda > 0$, we demonstrated how the growth rate of the field is reduces compared to the $\lambda = 0$ case. The field keeps

growing in density near the horizon of the black hole until it saturates. This is because the inwards force arising from the gravitational potential which eventually becomes 'balanced' by the repulsive pressure arising from the $\lambda > 0$ quartic term. In the $\lambda < 0$ case the force due to the quartic term is attractive instead of positive, making the potential shallower instead of steeper. The growth rate of the cloud becomes enhanced, but when the density reaches a certain point, the field begins to collapse as matter is pushed outwards. The three final states for these $\lambda = 0$, $\lambda > 0$ and $\lambda < 0$ cases are three distinct observable outcomes: a continually growing field, a solitonic configuration, and a collapsed field.

In Chapter 3, we looked at a similar scenario, involving the accretion of complex scalar fields with self-interaction terms around black holes, but instead considered models with multiple minima. Motivated by processes such as symmetry restoration and vacuum decay in nature, we investigated whether black hole accretion could catalyse these phenomena to occur in scalar fields possessing such multi-minima potentials. The models of particles we considered had either a symmetric double-well potential, or an asymmetric version where the depth of one well was greater than the other. In the symmetry restoration case, we showed that as the field accreted around the black hole, the oscillations around one potential minimum grew until the field started exploring regions of the potential beyond the central maximum. As accretion continued, the average value of the field began to tend from it initial value towards zero, thus restoring symmetry. We found the timescale on which symmetry is restored is reduced for scalar fields with higher mass and with less separation between the two minima in the potential. The other case was for vacuum decay. Here, we saw that the initial behaviour was the same as with the symmetry restoration scenario - as the black hole accretes matter, the field explores further regions of the potential as it eventually traverses the central maximum. In this case however, as the second well is much deeper, the field is dragged into it and becomes confined, therefore oscillating around this new minimum and in the process forming a bubble of 'true vacuum' which begins to expand radially outwards. The change in energy as more of the field is dragged into the true vacuum then feeds into

expanding this bubble. As with the symmetry restoration scenario, the mass of the field and the height of the central barrier both contribute to the decay timescales.

In Chapter 4, I derived the decomposition and simulated spin-2 tensor fields on a fixed background. I took inspiration from the ADM equations for the form of the decomposition for the tensor field. The evolution equations for the fields were found by introducing a tensor Σ_{kij} and splitting the Teukolsky equation into two first order differential equations. To test these equations of motion, I presented two example scenarios. Firstly, I looked at the case of gravitational waves scattering around a black hole to verify the work of He and Wu, 2022. The simulation was prepared such that a plane gravitational wave approached a Schwarzschild black hole. As the evolution continued, one could see how the wave front scattered around the black hole, forming new wavefronts propagating in different directions. Secondly, I looked at the case of wave dark matter on a Taub space time, and showed how this permits solutions in the form of propagating Bessel functions. In addition, with the fundamental simulation being that of a massless spin-2 wave, it permits great flexibility in testing other situations. With the same framework, one can simulate cases such as massive gravitational waves, and non standard wave solutions with little additional effort.

In addition to the future work regarding rank-2 fields proposed in Section 4.5.4, there are numerous extensions which would be interesting to study. General extensions to the works in Chapters 2 and 3 would be to investigate the effects that rotating black holes have on the results, and whether any new phenomena occur due to this. Additionally, as this work was in the fixed-background limit, another future project would be to re-introduce back-reaction and so a dynamic background spacetime and see what occurs as a result. This would requite the use of GRChombo and full numerical relativity.

It would also be interesting to study the mechanisms of symmetry restoration and vacuum decay in Chapter 3 in a wider astrophysical and cosmological context. In particular, it would be interesting to see how the bubble of symmetry restored state and of true vacuum interact with one-another. In the early universe in particular,

where symmetry breaking and phase differences are posed to be more likely, one could see what the final state of a patch of universe becomes after a number of seed vacuum decays or symmetry restorations occur within it. Furthermore, it would be interesting to see what observational signatures or effects on the present Universe this might produce.

All of these described additions to my work are exciting prospects to investigate, and each represent a humble exploration into Nature's infinite designs. Unlike Nature and her mysteries however, this thesis cannot be so vast, and therefore must now conclude.

> "*Live, then, and be happy, beloved children of my heart, and never forget that until the day when God shall deign to reveal the future to man, all human wisdom is summed up in these two words* - 'Wait and hope.'"
> –Alexandre Dumas
> *The Count of Monte Cristo, Translated by Robin Buss*

Appendices

A
Numerical Relativity

A.1 The BSSN System

The Hamiltonian and momentum constraints are

$$R - K_{ij}K^{ij} + K^2 = 2\rho, \tag{A.1}$$

and

$$D_j K^j_{\ i} - D_i K = S_i, \tag{A.2}$$

Where ρ is the energy density and S_i the momentum density both as measured by normal observers. Baumgarte and Shapiro, 1998 starts by defining the conformal spatial metric as

$$\tilde{\gamma}_{ij} = e^{-4\phi}\gamma_{ij} \tag{A.3}$$

with conformal factor ϕ and chooses

$$e^{4\phi} = \gamma^{1/3} \equiv \det(\gamma_{ij})^{1/3}. \tag{A.4}$$

to make the determinant of the conformal metric $\tilde{\gamma}_{ij}$ equal to one. The trace-free part of the extrinsic curvature is written as

$$A_{ij} = K_{ij} - \frac{1}{3}\gamma_{ij}K, \tag{A.5}$$

which also has its own conformal equivalent

$$\tilde{A}_{ij} = e^{-4\phi} A_{ij}. \tag{A.6}$$

Any of these conformal objects have their indices raised or lowered with the conformal spatial metric. The evolution equations for the conformal factor and the trace of the extrinsic curvature are

$$\frac{d}{dt}\phi = -\frac{1}{6}\alpha K \tag{A.7}$$

and

$$\frac{d}{dt}K = -\gamma^{ij} D_j D_i \alpha + \alpha(\tilde{A}_{ij}\tilde{A}^{ij} + \frac{1}{3}K^2) + \frac{1}{2}\alpha(\rho + S), \tag{A.8}$$

The evolution equations for the conformal spatial metric and the conformal trace-free part of the extrinsic curvature are

$$\frac{d}{dt}\tilde{\gamma}_{ij} = -2\alpha\tilde{A}_{ij} \tag{A.9}$$

and

$$\begin{aligned} \frac{d}{dt}\tilde{A}_{ij} &= e^{-4\phi}\left(-(D_i D_j \alpha)^{TF} + \alpha({}^{(3)}R_{ij}^{TF} - S_{ij}^{TF})\right) \\ &\quad +\alpha(K\tilde{A}_{ij} - 2\tilde{A}_{il}\tilde{A}^{l}{}_{j}). \end{aligned} \tag{A.10}$$

Where the TF superscript denotes objects as the trace-free parts. The Ricci tensor can be split into

$${}^{(3)}R_{ij} = {}^{(3)}\tilde{R}_{ij} + {}^{(3)}R_{ij}^{\phi}. \tag{A.11}$$

Where ${}^{(3)}R_{ij}^{\phi}$ is

$${}^{(3)}R_{ij}^{\phi} = -2\tilde{D}_i\tilde{D}_j\phi - 2\tilde{\gamma}_{ij}\tilde{D}^l\tilde{D}_l\phi + 4(\tilde{D}_i\phi)(\tilde{D}_j\phi) - 4\tilde{\gamma}_{ij}(\tilde{D}^l\phi)(\tilde{D}_l\phi), \tag{A.12}$$

and $\tilde{D}_i$ is the conformal spatial covariant derivative and is associated with the conformal spatial metric. The conformal Christoffel symbols are

$$\tilde{\Gamma}^i \equiv \tilde{\gamma}^{jk}\tilde{\Gamma}^i_{jk} = -\tilde{\gamma}^{ij}{}_{,j}, \tag{A.13}$$

where commas in the indices are used to denote partial derivatives. The evolution equation for the conformal connection is

$$\frac{\partial}{\partial t}\tilde{\Gamma}^i = -2\tilde{A}^{ij}\alpha_{,j} + 2\alpha\Big(\tilde{\Gamma}^i_{jk}\tilde{A}^{kj} - \frac{2}{3}\tilde{\gamma}^{ij}K_{,j} - \tilde{\gamma}^{ij}S_j + 6\tilde{A}^{ij}\phi_{,j}\Big) + \\ + \frac{\partial}{\partial x^j}\Big(\beta^l\tilde{\gamma}^{ij}{}_{,l} - 2\tilde{\gamma}^{m(j}\beta^{i)}{}_{,m} + \frac{2}{3}\tilde{\gamma}^{ij}\beta^l{}_{,l}\Big). \quad \text{(A.14)}$$

A.2 The CCZ4 System

This derivation is following the method in (Alic et al., 2012). The first step in deriving the CCZ4 system is to begin with the constraint-damped Z4 system, which is:

$$(\partial_t - \mathcal{L}_\beta)\,\gamma_{ij} = -2\alpha K_{ij}\,, \quad \text{(A.15)}$$

$$(\partial_t - \mathcal{L}_\beta)\,K_{ij} = -\nabla_i\alpha_j + \alpha\Big({}^{(3)}R_{ij} + \nabla_i Z_j + \nabla_j Z_i - 2K_{ij}K^{ij} \\ + (K - 2\Theta)\,K_{ij} - \kappa_1\,(1+\kappa_2)\,\Theta\gamma_{ij}\Big) - 8\pi\alpha\left(S_{ij} - \frac{1}{2}\,(S-\tau)\,\gamma_{ij}\right), \quad \text{(A.16)}$$

$$(\partial_t - \mathcal{L}_\beta)\,Z_i = \alpha\left(\nabla_k\left(K^k{}_i - \delta^k{}_i K\right) + \partial_i\Theta - \frac{\Theta}{\alpha}\alpha_i - 2K^k{}_i Z_k\right) \\ +\alpha\,(\kappa_1 Z_i - 8\pi S_i)\,, \quad \text{(A.17)}$$

$$(\partial_t - \mathcal{L}_\beta)\,\Theta = \frac{\alpha}{2}\left({}^{(3)}R + (K-2\Theta)\,K - K^2 + 2\nabla_k Z^k - \frac{2}{\alpha}\alpha_k Z^k\right) \\ +\frac{\alpha}{2}\,(-2\kappa_1\,(2+\kappa_2)\,\Theta - 16\pi\tau)\,,. \quad \text{(A.18)}$$

where $\alpha_i \equiv \nabla_i\alpha$, and τ_1, τ_2 are damping constants - refer to (Alic et al., 2012) for details. S_i, S_{ij} and τ are all matter related quantities and are defined as $S_i \equiv \gamma^\mu{}_i n_\nu T^\nu{}_\mu\,, S_{ij} \equiv \gamma^\mu{}_i\gamma^\nu{}_j T_{\mu\nu}$, and $\tau \equiv n_\mu n_\nu T^{\mu\nu}$. We first begin by redefining the spatial metric to be conformal instead. This means that

$$\tilde{\gamma}_{ij} = \phi^2\gamma_{ij}, \quad \text{(A.19)}$$

with unit determinant $\phi = (\det(\gamma_{ij}))^{-1/6}$. Next, we decompose the extrinsic curvature into its trace ($K \equiv K_{ij}\gamma^{ij}$) and trace free components. The trace free part is

$$\tilde{A}_{ij} = \phi^2\left(K_{ij} - \frac{1}{3}K\gamma_{ij}\right). \quad \text{(A.20)}$$

We can now write the three-dimensional Ricci tensor ${}^{(3)}R_{ij}$ as two parts - one which contains conformal terms, and the other spatial derivatives of the conformal metric $\tilde{\gamma}_{ij}$. This splitting of $R_{ij} = \tilde{R}_{ij} + R^{\phi}_{ij}$ is given by the components

$$\tilde{R}_{ij} = -\frac{1}{2}\tilde{\gamma}^{lm}\partial_l\partial_m\tilde{\gamma}_{ij} + \tilde{\gamma}_{k(i}\partial_{j)}\tilde{\Gamma}^k + \tilde{\Gamma}^k\tilde{\Gamma}_{(ij)k}\tilde{\gamma}^{lm}\left(2\tilde{\Gamma}^k{}_{l(i}\tilde{\Gamma}_{j)km} + \tilde{\Gamma}^k{}_{im}\tilde{\Gamma}_{kjl}\right) \quad \text{(A.21)}$$

$$\tilde{R}^{\phi}_{ij} = \frac{1}{\phi^2}\left(\phi\left(\tilde{\nabla}_i\tilde{\nabla}_j\phi + \tilde{\gamma}_{ij}\tilde{\nabla}^l\tilde{\nabla}_l\phi\right) - 2\tilde{\gamma}_{ij}\tilde{\nabla}^l\phi\tilde{\nabla}_l\phi\right). \quad \text{(A.22)}$$

The derivation for the full system of equations now consists of taking the Z4 formulation, and substituting in the modified variables as have just been defined above. As a brief demonstration of this, one can take Equation (A.15) and substitute in Equation (A.19) to find

$$\phi^{-2}\left(\partial_t - \mathcal{L}_\beta\right)\tilde{\gamma}_{ij} - 2\phi^{-3}\tilde{\gamma}_{ij}\left(\partial_t - \mathcal{L}_\beta\right)\phi = -2\alpha K_{ij}. \quad \text{(A.23)}$$

Then, K_{ij} can be substituted out using Equation (A.20) to find

$$\phi^{-2}\left(\partial_t - \mathcal{L}_\beta\right)\tilde{\gamma}_{ij} - 2\phi^{-3}\tilde{\gamma}_{ij}\left(\partial_t - \mathcal{L}_\beta\right)\phi = -2\alpha\tilde{A}_{ij}\phi^{-2} - \frac{2}{3}\alpha\phi^{-2}K\tilde{\gamma}_{ij}. \quad \text{(A.24)}$$

This equation can then be separated and expanded to find:

$$\partial_t\tilde{\gamma}_{ij} = -2\alpha\tilde{A}_{ij} + 2\tilde{\gamma}_{k(i}\partial_{j)}\ \beta^k - \frac{2}{3}\tilde{\gamma}_{ij}\partial_k\ \beta^k + \beta^k\partial_k\tilde{\gamma}_{ij} \quad \text{(A.25)}$$

and

$$\partial_t\phi = \frac{1}{3}\alpha\phi K - \frac{1}{3}\phi\partial_k\beta^k + \beta^k\partial_k\phi\,, \quad \text{(A.26)}$$

The full CCZ4 system (Alic et al., 2012) of equations is then found by repeating

the above process for all of the other variables. The system is given by

$$\partial_t \tilde{\gamma}_{ij} = -2\alpha \tilde{A}_{ij} + 2\tilde{\gamma}_{k(i}\partial_{j)}\ \beta^k - \frac{2}{3}\tilde{\gamma}_{ij}\partial_k\ \beta^k + \beta^k \partial_k \tilde{\gamma}_{ij}\,, \tag{A.27}$$

$$\begin{aligned}\partial_t \tilde{A}_{ij} &= \phi^2 \left[-\nabla_i\nabla_j\alpha + \alpha\left(R_{ij} + \nabla_i Z_j + \nabla_j Z_i - 8\pi S_{ij}\right)\right]^{\mathrm{TF}} \\ &\quad +\alpha\tilde{A}_{ij}\left(K - 2\Theta\right) - 2\alpha\tilde{A}_{il}\tilde{A}^l_j + 2\tilde{A}_{k(i}\partial_{j)}\ \beta^k - \frac{2}{3}\tilde{A}_{ij}\partial_k\ \beta^k \\ &\quad +\beta^k\partial_k\tilde{A}_{ij}\,,\end{aligned} \tag{A.28}$$

$$\partial_t \phi = \frac{1}{3}\alpha\phi K - \frac{1}{3}\phi\partial_k\beta^k + \beta^k\partial_k\phi\,, \tag{A.29}$$

$$\begin{aligned}\partial_t K &= -\nabla^i\nabla_i\alpha + \alpha\left(R + 2\nabla_i Z^i + K^2 - 2\Theta K\right) \\ &\quad +\beta^j\partial_j K - 3\alpha\kappa_1\left(1+\kappa_2\right)\Theta + 4\pi\alpha\left(S - 3\tau\right)\,,\end{aligned} \tag{A.30}$$

$$\begin{aligned}\partial_t \Theta &= \frac{1}{2}\alpha\left(R + 2\nabla_i Z^i - \tilde{A}_{ij}\tilde{A}^{ij} + \frac{2}{3}K^2 - 2\Theta K\right) \\ &\quad -Z^i\partial_i\alpha + \beta^k\partial_k\Theta - \alpha\kappa_1\left(2+\kappa_2\right)\Theta - 8\pi\alpha\,\tau\,,\end{aligned} \tag{A.31}$$

$$\begin{aligned}\partial_t \hat{\Gamma}^i &= 2\alpha\left(\tilde{\Gamma}^i_{jk}\tilde{A}^{jk} - 3\tilde{A}^{ij}\frac{\partial_j\phi}{\phi} - \frac{2}{3}\tilde{\gamma}^{ij}\partial_j K\right) \\ &\quad +2\tilde{\gamma}^{ki}\left(\alpha\partial_k\Theta - \Theta\partial_k\alpha - \frac{2}{3}\alpha K Z_k\right) \\ &\quad -2\tilde{A}^{ij}\partial_j\alpha + \tilde{\gamma}^{kl}\partial_k\partial_l\beta^i + \frac{1}{3}\tilde{\gamma}^{ik}\partial_k\partial_l\beta^l \\ &\quad +\frac{2}{3}\tilde{\Gamma}^i\partial_k\beta^k - \tilde{\Gamma}^k\partial_k\beta^i + 2\kappa_3\left(\frac{2}{3}\tilde{\gamma}^{ij}Z_j\partial_k\beta^k - \tilde{\gamma}^{jk}Z_j\partial_k\beta^i\right) \\ &\quad +\beta^k\partial_k\hat{\Gamma}^i - 2\alpha\kappa_1\tilde{\gamma}^{ij}Z_j - 16\pi\alpha\tilde{\gamma}^{ij}S_j\,,\end{aligned} \tag{A.32}$$

$$\partial_t\alpha = -2\alpha\left(K - 2\Theta\right) + \beta^k\partial_k\alpha\,, \tag{A.33}$$

$$\partial_t\beta^i = fB^i + \beta^k\partial_k\beta^i\,, \tag{A.34}$$

$$\partial_t B^i = \partial_t\hat{\Gamma}^i - \beta^k\partial_k\hat{\Gamma}^i + \beta^k\partial_k B^i - \eta B^i\,, \tag{A.35}$$

Here, $\hat{\Gamma}^i$ is defined as

$$\hat{\Gamma}^i \equiv \tilde{\Gamma}^i + 2\tilde{\gamma}^{ij}Z_j. \tag{A.36}$$

Equations (A.33 - A.35) arise due to choices for the gauge conditions - see Alcubierre et al., 2003.

A.3 Alternative Derivation For Proca - Laplace Operator Form

This is an alternative approach to deriving the equations of motion for a Proca field. In this approach, we seek wave equations of the form which can be written as a Laplace operator acting on the field, plus some function dependant on curvature and mass terms. This will allow us to define the field strength simply as the covariant derivative of the field

$$\tilde{F}_{\mu\ldots} = \nabla_\alpha H_{\ldots} \tag{A.37}$$

To rewrite the wave equation in 4.15 to look like this, we can commute the indices using the standard identity

$$\nabla_\beta \nabla_\alpha A_\mu - \nabla_\alpha \nabla_\beta A_\mu = R^\lambda{}_{\mu\alpha\beta} A_\lambda, \tag{A.38}$$

which, when raising an index, gives

$$\nabla^\mu \nabla_\nu A_\mu - \nabla_\nu \nabla^\mu A_\mu = R^\mu{}_\nu A_\mu. \tag{A.39}$$

Substituting this into Equation (4.16) results in:

$$\nabla^\mu \nabla_\mu A_\nu - \nabla_\nu \nabla^\mu A_\mu - R^\mu{}_\nu A_\mu - m^2 A_\nu = 0 \tag{A.40}$$

The second term on the left hand side can be eliminated using the Lorenz condition $\nabla^\mu A_\mu = 0$, which then yields the following:

$$\nabla^\mu \nabla_\mu A_\nu - R^\mu{}_\nu A_\mu - m^2 A_\nu = 0. \tag{A.41}$$

To proceed, we define a new tensor

$$P_{\mu\nu} = \nabla_\mu A_\nu, \tag{A.42}$$

which when substituted into Equation (A.41) results in

$$\nabla^\mu P_{\mu\nu} - R^\mu{}_\nu A_\mu - m^2 A_\nu = 0. \tag{A.43}$$

The primary constraint for the modified Proca field is more difficult to construct than before, as now we note that $\nabla^2 A^0 = \nabla^\alpha P^{\alpha 0}$ contains time derivatives of the conjugate momenta, meaning that there are second order time derivatives overall. Therefore, we perform some slight tricks to rewrite this constraint into a more appropriate form. We begin with $\mathcal{E}^0$ which is written as

$$\nabla^\mu \nabla_\mu A^0 - R^{\mu 0} A_\mu - m^2 A^0 = 0. \tag{A.44}$$

Lowering one of the dummy indices with the metric and expanding the summation, we find

$$g^{00}\nabla_0\nabla_0 A^0 + g^{0i}\nabla_0\nabla_i A^0 + g^{0i}\nabla_i\nabla_0 A^0 + g^{ij}\nabla_i\nabla_j A^0 - R^{\mu 0} A_\mu - m^2 A^0 = 0. \tag{A.45}$$

The first two terms are problematic; the first term contains a second order time derivative while the second contains a time derivative of $\nabla_i A^0 = P_i{}^0$. The first term in Equation (A.45) can be fixed by using:

$$g^{00}\nabla_0\nabla_0 A^0 = g^{00}\nabla_0\nabla_\mu A^\mu - g^{00}\nabla_0\nabla_i A^i \tag{A.46}$$

Then the first term on the right hand side can be eliminated with the Lorenz condition $\nabla_\mu A^\mu = 0$. Now, we need to permute the order of the covariant derivatives of these first two terms, such that we have a spatial index on the covariant derivative acting on the field strength tensor. Using Kronecker delta symbols, we can rewrite the term as:

$$g^{00}\nabla_0\nabla_i A^i = g^{00}\delta^a{}_0\delta^b{}_i\delta^i{}_c\nabla_a\nabla_b A^c \tag{A.47}$$

Then, as $\nabla_a\nabla_b A^c = \nabla_b\nabla_a A^c + R^{\lambda c}{}_{ba}$, the term becomes

$$g^{00}\nabla_0\nabla_i A^i = g^{00}\left(\nabla_i\nabla_0 A^i + R^{\lambda i}{}_{i0} A_\lambda\right). \tag{A.48}$$

The primary constraint is then

$$\begin{aligned} -g^{00}\nabla_i\nabla_0 A^i + 2g^{0i}\nabla_i\nabla_0 A^0 + g^{ij}\nabla_i\nabla_j A^0 + \\ + \left(-g^{00}R^{\lambda i}{}_{i0} + g^{0i}R^{\lambda 0}{}_{i0} - R^{\lambda 0}\right) A_\lambda - m^2 A^0 = 0. \end{aligned} \tag{A.49}$$

Now, we see that we have eliminated all of the second order time derivatives. The Proca field itself is decomposed in the same way as in the previous method, i.e. Equation (4.17), while the new field strength tensor is decomposed as

$$P_{\mu\nu} = \tilde{Q}_{\mu\nu} + n_\mu \bar{E}_\nu + n_\nu \tilde{E}_\mu + n_\mu n_\nu \hat{E}. \tag{A.50}$$

Following the procedure of applying the projection operator and contracting with the normal vector, we find

$$\partial_t \hat{X} = \mathcal{L}_\beta \hat{X} - \alpha \hat{E} - X_i D^i \alpha, \tag{A.51}$$

$$\partial_t X_i = \mathcal{L}_\beta X_i - \alpha \bar{E}_i - \hat{X} D_i \alpha + \alpha K^k{}_i X_k. \tag{A.52}$$

In addition to

$$\tilde{E}_i = D_i \hat{X} - K^k{}_i X_k, \tag{A.53}$$

$$\tilde{Q}_{ij} = D_i X_j - K_{ij} \hat{X}. \tag{A.54}$$

We now need to impose the Lorenz constraint, $\nabla^\mu A_\mu = 0$ to remove a degree of freedom so that we have only three overall. By decomposing this constraint into 3+1 form, either by directly evaluating it or substituting in the field strength tensor, we find the following two equations

$$X^k D_k \alpha + \alpha D_k X^k - \alpha K \hat{X} + \alpha \mathcal{L}_n \hat{X} = 0, \tag{A.55}$$

$$D_k X^k - K \hat{X} - \hat{E} = 0. \tag{A.56}$$

Firstly, we recognise Equation (A.55) as simply the equation of motion for $\hat{X}$ in Equation (A.51) without $\hat{E}$ and with some additional terms. By comparing Equations (A.55) and (A.51), or by simply looking at Equation (A.56), we notice that $\hat{E}$ is directly specified by a combination of the first order fields:

$$\hat{E} = D_i X^i - K \hat{X} \tag{A.57}$$

Therefore, $\bar{E}_i$ is the momentum of the system, with its three degrees of freedom now consistent with the overall three degrees of freedom for the Proca field, while

in this case we choose $\hat{E}$, $\tilde{E}_i$, and $\tilde{Q}_{ij}$ to be non-evolving. Substituting the values of $\hat{E}$, $\tilde{E}_i$, and $\tilde{Q}_{ij}$ in, the field strength tensor becomes:

$$P_{\mu\nu} = D_\mu X_\nu - K_{\mu\nu} + n_\nu \left(D_\mu \hat{X} - K^\alpha{}_\mu X_\alpha \right) + n_\mu \bar{E}_\nu + n_\mu n_\nu \left(D_\alpha X^\alpha - K\hat{X} \right) \quad \text{(A.58)}$$

As with the previous cases, we now wish to project with the projection operator and contract with the normal vector on Equation (A.43). The derived equation of motion for the momentum is

$$\begin{aligned} \partial_t \bar{E}_i = \mathcal{L}_\beta \bar{E}_i + \alpha m^2 X_i - \alpha D_j D^j X_i - D_j X^j D_i \alpha - D_j X_i D^j \alpha + \\ + \alpha K \bar{E}_i - \alpha K_{jk} K_i{}^k X^j + 2\alpha \hat{X} D_j K_i{}^j + K_{ij} \hat{X} D^j \alpha + \\ + 2\alpha K_{ij} D^j \hat{X} - \alpha \hat{X} D_i K + K \hat{X} D_i \alpha. \quad \text{(A.59)} \end{aligned}$$

So, with Equations (A.51, A.52, A.59) we have found the equations of motion using this alternative method.

B

Error Analysis - Convergence Testing

An important facet to consider of any simulation is that of numerical error. Numerical errors are a fundamental problem inherent to using numerics to solve a problem instead of analytics. The question is therefore how to mitigate sources of numerical error rather than eliminate them due to finite memory limitations. We are able to accurately track numerical error and even where it arises in a simulation through the aforementioned constraint equations. For the spacetime itself, there are the Hamiltonian and momentum constraints, found before as Equations (1.66) and (1.67). For the evolution of a system to be valid, these constraints must be satisfied at all times. As mentioned however, if numerical errors arise, then these constraints become violated and no longer hold. Evidently, we must find ways to combat this. One solution is to develop formalisms which have ways of 'damping' the error, such as the Z4 and CCZ4 systems as described in Section 1.4.2.4. Here, the addition of the Z_μ vector helps counteract the effect of numerical error and attempts to reduce the constraint violations back down to zero. Other ways involved more careful choices of coordinates, in particular with regards to the behaviour of the metric around the horizon. As numerical errors are generated by singularities in the coordinates, they will be in principle confined to regions of the simulation within the event horizon as opposed to in a region where they can communicate with the rest of the simulation domain.

The way to quantify the amount of numerical error in simulation is through a process called convergence testing. In essence, as one increases the resolution of the grid, we expect the amount of numerical error to decrease by a given factor. By increasing the resolution of the simulation, we can make more precise calculations and so introduce less error.

Here, I follow the arguments presented in Alcubierre, 2008 and Baumgarte and Shapiro, 2010. Suppose that there exists an exact solution to a differential equation, $u(t, x)$. It was observed by Richardson, 1911 that an approximate solution $u_\Delta(t, x)$can be expanded as a power series in terms of the grid spacing Δ, that is

$$u_\Delta(t, x) = u(t, x) + \Delta E_1(t, x) + \Delta^2 E_2(t, x) + \Delta^3 E_3(t, x) + \mathcal{O}(\Delta^4). \tag{B.1}$$

Note that these errors are independent of Δ. Next, as an example, let us assume we have a numerical scheme that is accurate to second order. This means that we can discard the first order error E_1 and so see that the error (the difference between approximate solution and exact solution) becomes

$$u_\Delta(t, x) - u(t, x) = \Delta^2 E_2(t, x) + \Delta^3 E_3(t, x) + \mathcal{O}(\Delta^4). \tag{B.2}$$

Suppose now that we double the resolution of the simulation, that is, halving the value of Δ. Equation (B.2) becomes:

$$4\left(u_{\Delta/2}(t, x) - u(t, x)\right) = \Delta^2 E_2(t, x) + \frac{1}{2}\Delta^3 E_3(t, x) + \mathcal{O}(\Delta^4). \tag{B.3}$$

It transpires that if we keep increasing the resolution, the error terms of order Δ^3 and above vanish and we find the following limit

$$\lim_{k\to\infty} 2^{2k}\left(u_{\Delta/k}(t, x) - u(t, x)\right) = \Delta^2 E_2(t, x), \tag{B.4}$$

which is Equation (6.156) in Baumgarte and Shapiro, 2010. This means that for a second order scheme, as we increase the resolution of the simulation, the error converges to $\mathcal{O}(\Delta^2)$. For schemes of order n, the errors converge to $\mathcal{O}(\Delta^n)$.

With this knowledge of how the errors should converge, we can now and quantify a numerical test. We begin with the assumption that we know the exact solution

for a field ϕ. We now define the error function, or the difference in value between the exact field ϕ and the field as simulated on a grid of step-size Δ_n:

$$\varepsilon_n(t) = \phi(t) - \phi_{\Delta_n}(t) \tag{B.5}$$

The convergence factor is defined as the ratio between the error functions of two simulations with different resolutions.

$$c(t) = \frac{||\varepsilon_1(t)||}{||\varepsilon_2(t)||} \tag{B.6}$$

In the limit of the step sizes tending towards zero, and using the knowledge from the Richardson scheme in Equations (B.1) and (B.4), we see in the continuum limit that

$$\lim_{\Delta \to 0} c(t) = \left(\frac{\Delta_1}{\Delta_2}\right)^n \equiv r^n. \tag{B.7}$$

Here, $r = \Delta_1/\Delta_2$ is the ratio between the step sizes and n is the order of convergence. So, for a fourth order scheme, we would expect the convergence factor to go as $\sim r^4$. If a pair of simulations obey Equation (B.7), then the error is decreasing at the theoretically correct rate, and so the simulations we have run are considered to be physically correct and the amount of error is under control. As we cannot achieve the ideal case of $\Delta \to 0$, a satisfactory fulfilment of Equation (B.7) tells us that our choice of Δ_1 and Δ_2 are small enough such that we are approaching this ideal regime and so are sufficiently convergent.

However, in many cases, we do not possess the exact solution for a field ϕ. Instead, we must look at the constraint equations. Taking for example the Hamiltonian constraint in Equation (1.66), we can define an error scalar $\mathcal{E}$:

$$\mathcal{E}(t) = {}^{(3)}R + K^2 + K_{ij}K^{ij} - 16\pi\rho \tag{B.8}$$

In a perfect simulation, $\mathcal{E}(t) = 0$. Therefore, it is the constraint violation 'fields' $\mathcal{E}_n(t)$ that we substitute into Equation (B.6) to find and test the ideal convergence factor r^n.

There are some situations we come across where we do not know the solution to a constraint. In these cases, it is possible to instead compare three separate simulations to each other. In this case, we define the convergence factor as:

$$c(t) = \frac{|\phi_{\Delta_1} - \phi_{\Delta_2}|}{|\phi_{\Delta_2} - \phi_{\Delta_3}|} \tag{B.9}$$

Where $\Delta_1, \Delta_2, \Delta_3$ are the spatial step sizes at the coarsest grid level for each resolution, from lowest resolution to highest. Then, in the $\Delta \to 0$ limit we find:

$$\lim_{\Delta \to 0} c(t) = \frac{\Delta_1^n - \Delta_2^n}{\Delta_2^n - \Delta_3^n} \tag{B.10}$$

where n is the order of convergence.

Overall, in situation where the only source of error is due to inaccuracies arising from finite-differencing, then for an order n scheme, we expect convergence to order n. In many cases however, there are additional sources of error which can break this. For example, in simulations involving singularities, numerical errors are inevitably generated and despite measures to prevent it, can propagate into the simulation domain outside of the horizon. In these situations, we no longer expect the order of convergence determined above, and instead see a lower one.

Bibliography

Aalbers, J. et al. (2023). "First Dark Matter Search Results from the LUX-ZEPLIN (LZ) Experiment". *Phys. Rev. Lett.* 131.4, p. 041002.

Aasi, J. et al. (2015). "Advanced LIGO". *Class. Quant. Grav.* 32, p. 074001.

Abbott, B. P. et al. (2016). "Observation of Gravitational Waves from a Binary Black Hole Merger". *Phys. Rev. Lett.* 116.6, p. 061102.

Abe, K. et al. (2001). "Observation of large CP violation in the neutral B meson system". *Phys. Rev. Lett.* 87, p. 091802.

Abuter, R. et al. (2022). "Mass distribution in the Galactic Center based on interferometric astrometry of multiple stellar orbits". *Astron. Astrophys.* 657, p. L12.

Acernese, F. et al. (2015). "Advanced Virgo: a second-generation interferometric gravitational wave detector". *Class. Quant. Grav.* 32.2, p. 024001.

Afshordi, N. et al. (2023). "Waveform Modelling for the Laser Interferometer Space Antenna".

Aghanim, N. et al. (2020). "Planck 2018 results. VI. Cosmological parameters". *Astron. Astrophys.* 641. [Erratum: Astron.Astrophys. 652, C4 (2021)], A6.

Akerib, D. S. et al. (2017). "Results from a search for dark matter in the complete LUX exposure". *Phys. Rev. Lett.* 118.2, p. 021303.

Akutsu, T. et al. (2021). "Overview of KAGRA: Detector design and construction history". *PTEP* 2021.5, 05A101.

Alavi-Harati, A. et al. (1999). "Observation of Direct CP Violation in $K_{S,L} \to \pi\pi$ Decays". *Phys. Rev. Lett.* 83, pp. 22–27.

Alcubierre, M. (2008). *Introduction to 3+1 Numerical Relativity*. Oxford University Press.

Alcubierre, M. et al. (2003). "Gauge conditions for long term numerical black hole evolutions without excision". *Phys. Rev. D* 67, p. 084023.

Alic, D. et al. (2012). "Conformal and covariant formulation of the Z4 system with constraint-violation damping". *Phys. Rev. D* 85, p. 064040.

Alonso-Álvarez, G., Cline, J. M., and Dewar, C. (2024). "Self-Interacting Dark Matter Solves the Final Parsec Problem of Supermassive Black Hole Mergers". *Phys. Rev. Lett.* 133.2, p. 021401.

Alvarez, G. and Yu, H.-B. (2021). "Density spikes near black holes in self-interacting dark matter halos and indirect detection constraints". *Phys. Rev. D* 104.4, p. 043013.

Alves Batista, R. et al. (2021). "EuCAPT White Paper: Opportunities and Challenges for Theoretical Astroparticle Physics in the Next Decade".

Amaro-Seoane, P. (2018). "Relativistic dynamics and extreme mass ratio inspirals". *Living Rev. Rel.* 21.1, p. 4.

Andrade, T. et al. (2021). "GRChombo: An adaptable numerical relativity code for fundamental physics". *J. Open Source Softw.* 6.68, p. 3703.

Andrade, T., Figueras, P., and Sperhake, U. (2022). "Evidence for violations of Weak Cosmic Censorship in black hole collisions in higher dimensions". *JHEP* 03, p. 111.

Anninos, P. et al. (1995). "Three-dimensional numerical relativity: The Evolution of black holes". *Phys. Rev. D* 52, pp. 2059–2082.

Aoki, K. and Mukohyama, S. (2016). "Massive gravitons as dark matter and gravitational waves". *Phys. Rev. D* 94.2, p. 024001.

Aprile, E. et al. (2018). "Dark Matter Search Results from a One Ton-Year Exposure of XENON1T". *Phys. Rev. Lett.* 121.11, p. 111302.

Arakawa, J. et al. (2023). "Detection of Bosenovae with Quantum Sensors on Earth and in Space".

Arakawa, J. et al. (2024). "Bosenovae with Quadratically-Coupled Scalars in Quantum Sensing Experiments".

Arbey, A., Lesgourgues, J., and Salati, P. (2003). "Galactic halos of fluid dark matter". *Phys. Rev. D* 68, p. 023511.

Aristotle (350 BCE). *On The Heavens*. Self Published.

Arnold, P. B. (1990). "GRAVITY AND FALSE VACUUM DECAY RATES: O(3) SOLUTIONS". *Nucl. Phys. B* 346, pp. 160–192.

Arnowitt, R. L., Deser, S., and Misner, C. W. (1962). "The Dynamics of general relativity". *Gen. Rel. Grav.* 40, pp. 1997–2027.

Arvanitaki, A. and Dubovsky, S. (2011). "Exploring the String Axiverse with Precision Black Hole Physics". *Phys. Rev. D* 83, p. 044026.

Asano, Y. et al. (1981). "Search for a Rare Decay Mode K+ —> pi+ Neutrino anti-neutrino and Axion". *Phys. Lett. B* 107. Ed. by R. J. Cence, E. Ma, and A. Roberts, p. 159.

Aubert, B. et al. (2001). "Measurement of CP violating asymmetries in B^0 decays to CP eigenstates". *Phys. Rev. Lett.* 86, pp. 2515–2522.

Aurrekoetxea, J. C. et al. (2025). "GRTresna: An open-source code to solve the initial data constraints in numerical relativity".

Aurrekoetxea, J. C., Clough, K., and Lim, E. A. (2023). "CTTK: a new method to solve the initial data constraints in numerical relativity". *Class. Quant. Grav.* 40.7, p. 075003.

Aurrekoetxea, J. C. et al. (2020). "The Effects of Potential Shape on Inhomogeneous Inflation". *JCAP* 05, p. 030.

Aurrekoetxea, J. C. et al. (2024a). "Effect of Wave Dark Matter on Equal Mass Black Hole Mergers". *Phys. Rev. Lett.* 132.21, p. 211401.

Aurrekoetxea, J. C. et al. (2024b). "GRDzhadzha: A code for evolving relativistic matter on analytic metric backgrounds". *J. Open Source Softw.* 9.96, p. 5956.

Aurrekoetxea, J. C. et al. (2024c). "Self-interacting scalar dark matter around binary black holes". *Phys. Rev. D* 110.8, p. 083011.

Babak, S. et al. (2017). "Science with the space-based interferometer LISA. V: Extreme mass-ratio inspirals". *Phys. Rev. D* 95.10, p. 103012.

Babichev, E. et al. (2016). "Heavy spin-2 Dark Matter". *JCAP* 09, p. 016.

Baker, J. G., Campanelli, M., and Lousto, C. O. (2002). "The Lazarus project: A Pragmatic approach to binary black hole evolutions". *Phys. Rev. D* 65, p. 044001.

Baker, J. G. et al. (2006). "Gravitational wave extraction from an inspiraling configuration of merging black holes". *Phys. Rev. Lett.* 96, p. 111102.

Balkin, R. et al. (2023). "Heavy neutron stars from light scalars".

Bamber, J. et al. (2021). "Growth of accretion driven scalar hair around Kerr black holes". *Phys. Rev. D* 103.4, p. 044059.

Bamber, J. et al. (2023). "Black hole merger simulations in wave dark matter environments". *Phys. Rev. D* 107.2, p. 024035.

Barack, L. et al. (2019). "Black holes, gravitational waves and fundamental physics: a roadmap". *Class. Quant. Grav.* 36.14, p. 143001.

Barausse, E. et al. (2020). "Prospects for Fundamental Physics with LISA". *Gen. Rel. Grav.* 52.8, p. 81.

Barausse, E., Cardoso, V., and Pani, P. (2014). "Can environmental effects spoil precision gravitational-wave astrophysics?" *Phys. Rev. D* 89.10, p. 104059.

Barranco, J. et al. (2012). "Schwarzschild black holes can wear scalar wigs". *Phys. Rev. Lett.* 109, p. 081102.

Bartelmann, M. (2010). "Gravitational Lensing". *Class. Quant. Grav.* 27, p. 233001.

Bartolo, N. et al. (2016). "Science with the space-based interferometer LISA. IV: Probing inflation with gravitational waves". *JCAP* 12, p. 026.

Baryakhtar, M. et al. (2021). "Black hole superradiance of self-interacting scalar fields". *Phys. Rev. D* 103.9, p. 095019.

Baumgarte, T. W. and Shapiro, S. L. (1998). "On the numerical integration of Einstein's field equations". *Phys. Rev. D* 59, p. 024007.

Baumgarte, T. W. and Shapiro, S. L. (2010). *Numerical Relativity: Solving Einstein's Equations on the Computer*. 1st ed. Cambridge University Press.

Belotsky, K. M. et al. (2014). "Signatures of primordial black hole dark matter". *Mod. Phys. Lett. A* 29.37, p. 1440005.

Berezhiani, L., Elder, B., and Khoury, J. (2019). "Dynamical Friction in Superfluids". *JCAP* 10, p. 074.

Berezhiani, L. and Khoury, J. (2015). "Theory of dark matter superfluidity". *Phys. Rev. D* 92, p. 103510.

Berezhiani, L. et al. (2024). "Dynamical friction in dark matter superfluids: The evolution of black hole binaries". *JCAP* 06, p. 024.

Berezin, V. A., Kuzmin, V. A., and Tkachev, I. I. (1988). "O(3) Invariant Tunneling in General Relativity". *Phys. Lett. B* 207, pp. 397–403.

Berezin, V. A., Kuzmin, V. A., and Tkachev, I. I. (1991). "Black holes initiate false vacuum decay". *Phys. Rev. D* 43, pp. 3112–3116.

Berti, E., Cardoso, V., and Will, C. M. (2006). "On gravitational-wave spectroscopy of massive black holes with the space interferometer LISA". *Phys. Rev. D* 73, p. 064030.

Bertone, G., Hooper, D., and Silk, J. (2005). "Particle dark matter: Evidence, candidates and constraints". *Phys. Rept.* 405, pp. 279–390.

Bertone, G. and Merritt, D. (2005). "Time-dependent models for dark matter at the Galactic Center". *Phys. Rev. D* 72, p. 103502.

Bertone, G. and Tait M. P., T. (2018). "A new era in the search for dark matter". *Nature* 562.7725, pp. 51–56.

Bertone, G. et al. (2024). "Dark Matter Mounds: towards a realistic description of dark matter overdensities around black holes".

Blanco-Pillado, J. J., Deng, H., and Vilenkin, A. (2019). "Flyover vacuum decay". *JCAP* 12, p. 001.

Bona, C. et al. (2003). "General covariant evolution formalism for numerical relativity". *Phys. Rev. D* 67, p. 104005.

Bona, C., Palenzuela-Luque, C., and Bona-Casas, C. (2009). *Elements of Numerical Relativity and Relativistic Hydrodynamics: From Einstein' s Equations to Astrophysical Simulations*. Vol. 783. Lecture Notes in Physics. Berlin, Heidelberg: Springer Berlin Heidelberg.

Bona, C. et al. (1995). "A New formalism for numerical relativity". *Phys. Rev. Lett.* 75, pp. 600–603.

Boskovic, M. et al. (2019). "Axionic instabilities and new black hole solutions". *Phys. Rev. D* 99.3, p. 035006.

Bošković, M., Koschnitzke, M., and Porto, R. A. (2024). "Signatures of ultralight bosons in the orbital eccentricity of binary black holes".

Boudon, A. et al. (2024). "Gravitational waves from binary black holes in a self-interacting scalar dark matter cloud". *Phys. Rev. D* 109.4, p. 043504.

Bowen, J. M. and York Jr., J. W. (1980). "Time asymmetric initial data for black holes and black hole collisions". *Phys. Rev. D* 21, pp. 2047–2056.

Braden, J. et al. (2019). "New Semiclassical Picture of Vacuum Decay". *Phys. Rev. Lett.* 123.3. [Erratum: Phys.Rev.Lett. 129, 059901 (2022)], p. 031601.

Braden, J. et al. (2023). "Mass renormalization in lattice simulations of false vacuum decay". *Phys. Rev. D* 107.8, p. 083509.

Brito, R., Cardoso, V., and Pani, P. (2013). "Massive spin-2 fields on black hole spacetimes: Instability of the Schwarzschild and Kerr solutions and bounds on the graviton mass". *Phys. Rev. D* 88.2, p. 023514.

Brito, R., Cardoso, V., and Pani, P. (2015). "Superradiance: New Frontiers in Black Hole Physics". *Lect. Notes Phys.* 906, pp.1–237.

Brito, R. P. (2016). “Fundamental fields around compact objects: Massive spin-2 fields, Superradiant instabilities and Stars with dark matter cores”. PhD thesis. Lisbon U.

Brown, A. R. and Dahlen, A. (2011). “Populating the Whole Landscape”. *Phys. Rev. Lett.* 107, p. 171301.

Bucciotti, B. and Trincherini, E. (2023). “interplay between black holes and ultralight dark matter: analytic solutions”. *JHEP* 11, p. 193.

Buchbinder, I. L. et al. (2000). “Equations of motion for massive spin-2 field coupled to gravity”. *Nucl. Phys. B* 584, pp. 615–640.

Budker, D. et al. (2023). “A generic formation mechanism of ultralight dark matter solar halos”. *JCAP* 12, p. 021.

Burda, P., Gregory, R., and Moss, I. (2015a). “Gravity and the stability of the Higgs vacuum”. *Phys. Rev. Lett.* 115, p. 071303.

Burda, P., Gregory, R., and Moss, I. (2015b). “Vacuum metastability with black holes”. *JHEP* 08, p. 114.

Burda, P., Gregory, R., and Moss, I. (2016). “The fate of the Higgs vacuum”. *JHEP* 06, p. 025.

Cadez, A. (1971). “Colliding Black Holes”. PhD thesis. University of North Carolina at Chapel Hill.

Callan Jr., C. G. and Coleman, S. R. (1977). “The Fate of the False Vacuum. 2. First Quantum Corrections”. *Phys. Rev. D* 16, pp. 1762–1768.

Campanelli, M. et al. (2006). “Accurate evolutions of orbiting black-hole binaries without excision”. *Phys. Rev. Lett.* 96, p. 111101.

Caneva Santoro, G. et al. (2024). “First Constraints on Compact Binary Environments from LIGO-Virgo Data”. *Phys. Rev. Lett.* 132.25, p. 251401.

Cannizzaro, E. et al. (2022). “Dark photon superradiance quenched by dark matter”. *Phys. Rev. D* 106.8, p. 083019.

Capela, F., Pshirkov, M., and Tinyakov, P. (2013a). “Constraints on primordial black holes as dark matter candidates from capture by neutron stars”. *Phys. Rev. D* 87.12, p. 123524.

Capela, F., Pshirkov, M., and Tinyakov, P. (2013b). “Constraints on Primordial Black Holes as Dark Matter Candidates from Star Formation”. *Phys. Rev. D* 87.2, p. 023507.

Caprini, C. et al. (2020). "Detecting gravitational waves from cosmological phase transitions with LISA: an update". *JCAP* 03, p. 024.

Cardoso, V. and Duque, F. (2020). "Environmental effects in gravitational-wave physics: Tidal deformability of black holes immersed in matter". *Phys. Rev. D* 101.6, p. 064028.

Cardoso, V. and Macedo, C. F. B. (2020). "Drifting through the medium: kicks and self-propulsion of binaries within accretion discs and other environments". *Mon. Not. Roy. Astron. Soc.* 498.2, pp. 1963–1972.

Cardoso, V. and Maselli, A. (2020). "Constraints on the astrophysical environment of binaries with gravitational-wave observations". *Astron. Astrophys.* 644, A147.

Cardoso, V. et al. (2004). "The Black hole bomb and superradiant instabilities". *Phys. Rev. D* 70. [Erratum: Phys.Rev.D 70, 049903 (2004)], p. 044039.

Cardoso, V. et al. (2022). "Gravitational Waves from Extreme-Mass-Ratio Systems in Astrophysical Environments". *Phys. Rev. Lett.* 129.24, p. 241103.

Carlson, E. D., Machacek, M. E., and Hall, L. J. (1992). "Self-interacting dark matter". *Astrophys. J.* 398, pp. 43–52.

Carr, B. J. et al. (2010). "New cosmological constraints on primordial black holes". *Phys. Rev. D* 81, p. 104019.

Carroll, S. M. (2001). "The Cosmological constant". *Living Rev. Rel.* 4, p. 1.

Cespedes, S. et al. (2021). "Lorentzian vacuum transitions: Open or closed universes?" *Phys. Rev. D* 104.2, p. 026013.

Chadha-Day, F., Ellis, J., and Marsh, D. J. E. (2022). "Axion dark matter: What is it and why now?" *Sci. Adv.* 8.8, abj3618.

Chia, H. S. et al. (2023). "Self-interacting gravitational atoms in the strong-gravity regime". *JCAP* 04, p. 018.

Choi, K., Im, S. H., and Sub Shin, C. (2021). "Recent Progress in the Physics of Axions and Axion-Like Particles". *Ann. Rev. Nucl. Part. Sci.* 71, pp. 225–252.

Choquet-Bruhat, Y., Chrusciel, P. T., and Martin-Garcia, J. M. (2011). "The Cauchy problem on a characteristic cone for the Einstein equations in arbitrary dimensions". *Annales Henri Poincare* 12, pp. 419–482.

Choudhary, S. et al. (2021). "Gravitational waves from binary black hole mergers surrounded by scalar field clouds: Numerical simulations and observational implications". *Phys. Rev. D* 103.4, p. 044032.

Christenson, J. H. et al. (1964). "Evidence for the 2π Decay of the K_2^0 Meson". *Phys. Rev. Lett.* 13, pp. 138–140.

Chu, X. and Garcia-Cely, C. (2017). "Self-interacting Spin-2 Dark Matter". *Phys. Rev. D* 96.10, p. 103519.

Clough, K. (2021). "Continuity equations for general matter: applications in numerical relativity". *Class. Quant. Grav.* 38.16, p. 167001.

Clough, K., Ferreira, P. G., and Lagos, M. (2019). "Growth of massive scalar hair around a Schwarzschild black hole". *Phys. Rev. D* 100.6, p. 063014.

Clough, K. et al. (2015). "GRChombo : Numerical Relativity with Adaptive Mesh Refinement". *Class. Quant. Grav.* 32.24, p. 245011.

Clough, K. et al. (2022). "Ghost Instabilities in Self-Interacting Vector Fields: The Problem with Proca Fields". *Phys. Rev. Lett.* 129.15, p. 151102.

Clowe, D., Gonzalez, A., and Markevitch, M. (2004). "Weak lensing mass reconstruction of the interacting cluster 1E0657-558: Direct evidence for the existence of dark matter". *Astrophys. J.* 604, pp. 596–603.

Cole, P. S. et al. (2023a). "Distinguishing environmental effects on binary black hole gravitational waveforms". *Nature Astron.* 7.8, pp. 943–950.

Cole, P. S. et al. (2023b). "Measuring dark matter spikes around primordial black holes with Einstein Telescope and Cosmic Explorer". *Phys. Rev. D* 107.8, p. 083006.

Coleman, S. R. (1977). "The Fate of the False Vacuum. 1. Semiclassical Theory". *Phys. Rev. D* 15. [Erratum: Phys.Rev.D 16, 1248 (1977)], pp. 2929–2936.

Coleman, S. R. (1985). "Q-balls". *Nucl. Phys. B* 262.2. [Addendum: Nucl.Phys.B 269, 744 (1986)], p. 263.

Coleman, S. R. and De Luccia, F. (1980). "Gravitational Effects on and of Vacuum Decay". *Phys. Rev. D* 21, p. 3305.

Coleman, S. R. and Weinberg, E. J. (1973). "Radiative Corrections as the Origin of Spontaneous Symmetry Breaking". *Phys. Rev. D* 7, pp. 1888–1910.

Copeland, E. J., Liddle, A. R., and Wands, D. (1998). "Exponential potentials and cosmological scaling solutions". *Phys. Rev. D* 57, pp. 4686–4690.

Covi, L., Roulet, E., and Vissani, F. (1996). "CP violating decays in leptogenesis scenarios". *Phys. Lett. B* 384, pp. 169–174.

Croft, R. (2023). "Local continuity of angular momentum and noether charge for matter in general relativity". *Class. Quant. Grav.* 40.10, p. 105007.

De Cesare, M. and Oliveri, R. (2023). "Backreaction of scalar waves on black holes at low frequencies". *Phys. Rev. D* 108.4, p. 044050.

De Luca, V. and Khoury, J. (2023). "Superfluid dark matter around black holes". *JCAP* 04, p. 048.

Detweiler, S. L. (1980). "KLEIN-GORDON EQUATION AND ROTATING BLACK HOLES". *Phys. Rev. D* 22, pp. 2323–2326.

Diez-Tejedor, A., Gonzalez-Morales, A. X., and Profumo, S. (2014). "Dwarf spheroidal galaxies and Bose-Einstein condensate dark matter". *Phys. Rev. D* 90.4, p. 043517.

Dolan, L. and Jackiw, R. (1974). "Symmetry Behavior at Finite Temperature". *Phys. Rev. D* 9, pp. 3320–3341.

Doneva, D. D. et al. (2024). "Spontaneous scalarization". *Rev. Mod. Phys.* 96.1, p. 015004.

East, W. E. (2022). "Vortex String Formation in Black Hole Superradiance of a Dark Photon with the Higgs Mechanism". *Phys. Rev. Lett.* 129.14, p. 141103.

East, W. E. and Huang, J. (2022). "Dark photon vortex formation and dynamics". *JHEP* 12, p. 089.

East, W. E. and Pretorius, F. (2017). "Superradiant Instability and Backreaction of Massive Vector Fields around Kerr Black Holes". *Phys. Rev. Lett.* 119.4, p. 041101.

East, W. E. and Siemonsen, N. (2023). "Instability and backreaction of massive spin-2 fields around black holes". *Phys. Rev. D* 108.12, p. 124048.

Eby, J. and Takhistov, V. (2024). "Diffuse Axion Background".

Einstein, A. (1915). "Erklärung der Perihelbewegung des Merkur aus der allgemeinen Relativitätstheorie". *Sitzungsberichte der Königlich Preussischen Akademie der Wissenschaften*, pp. 831–839.

Einstein, A. (1916). "Die Grundlage der allgemeinen Relativitätstheorie". *Annalen der Physik* 354.7, pp. 769–822.

Einstein, A. (1918). "Über Gravitationswellen". *Sitzungsber. Preuss. Akad. Wiss. Berlin (Math. Phys.)* 1918, pp. 154–167.

Elbert, O. D. et al. (2015). "Core formation in dwarf haloes with self-interacting dark matter: no fine-tuning necessary". *Mon. Not. Roy. Astron. Soc.* 453.1, pp. 29–37.

Eppley, K. R. (1975). "The numerical evolution of the collision of two black holes". PhD thesis. Princeton University, New Jersey.

Evstafyeva, T. et al. (2023). "Unequal-mass boson-star binaries: initial data and merger dynamics". *Class. Quant. Grav.* 40.8, p. 085009.

Fanti, V. et al. (1999). "A New measurement of direct CP violation in two pion decays of the neutral kaon". *Phys. Lett. B* 465, pp. 335–348.

Farzan, Y. and Akbarieh, A. R. (2012). "VDM: A model for Vector Dark Matter". *JCAP* 10, p. 026.

Feng, J. L. (2010). "Dark Matter Candidates from Particle Physics and Methods of Detection". *Ann. Rev. Astron. Astrophys.* 48, pp. 495–545.

Feng, W.-X. et al. (2022). "Self-interacting dark scalar spikes around black holes via relativistic Bondi accretion". *JCAP* 08.08, p. 032.

Ferreira, E. G. M. (2021). "Ultra-light dark matter". *Astron. Astrophys. Rev.* 29.1, p. 7.

Ferreira, P. G. and Joyce, M. (1998). "Cosmology with a primordial scaling field". *Phys. Rev. D* 58, p. 023503.

Ficarra, G. (2021). "Scalar field dynamics around black holes: superradiant instabilities and binary evolution". In: *55th Rencontres de Moriond on Gravitation*.

Fischer, M. S. and Sagunski, L. (2024). "Dynamical friction from self-interacting dark matter".

Foschi, A. et al. (2023). "Using the motion of S2 to constrain scalar clouds around Sgr A*". *Mon. Not. Roy. Astron. Soc.* 524.1, pp. 1075–1086.

Friedberg, R., Lee, T. D., and Pang, Y. (1987). "Scalar Soliton Stars and Black Holes". *Phys. Rev. D* 35. Ed. by H.-C. Ren and Y. Pang, p. 3658.

Gnedin, O. Y. and Primack, J. R. (2004). "Dark Matter Profile in the Galactic Center". *Phys. Rev. Lett.* 93, p. 061302.

Gondolo, P. and Silk, J. (1999). "Dark matter annihilation at the galactic center". *Phys. Rev. Lett.* 83, pp. 1719–1722.

Graham, P. W., Mardon, J., and Rajendran, S. (2016). "Vector Dark Matter from Inflationary Fluctuations". *Phys. Rev. D* 93.10, p. 103520.

Gregory, R., Moss, I. G., and Withers, B. (2014). "Black holes as bubble nucleation sites". *JHEP* 03, p. 081.

Hahn, S. G. and Lindquist, R. W. (1964). "The two-body problem in geometrodynamics". *Annals of Physics* 29.2, pp. 304–331.

Hawking, S. W. (1981). "Interacting Quantum Fields Around a Black Hole". *Commun. Math. Phys.* 80, p. 421.

Hawking, S. W. and Moss, I. G. (1982). "Supercooled Phase Transitions in the Very Early Universe". *Phys. Lett. B* 110, pp. 35–38.

He, J.-h. and Wu, Z. (2022). "Simulating gravitational waves passing through the spacetime of a black hole". *Phys. Rev. D* 106.12, p. 124037.

Herdeiro, C. A. R., Radu, E., and Santos, N. M. (2022). "A bound on energy extraction (and hairiness) from superradiance". *Phys. Lett. B* 824, p. 136835.

Hertzberg, M. P., Rompineve, F., and Shah, N. (2020). "Quantitative Analysis of the Stochastic Approach to Quantum Tunneling". *Phys. Rev. D* 102.7, p. 076003.

Hertzberg, M. P. and Yamada, M. (2019). "Vacuum Decay in Real Time and Imaginary Time Formalisms". *Phys. Rev. D* 100.1, p. 016011.

Hiscock, W. A. (1987). "CAN BLACK HOLES NUCLEATE VACUUM PHASE TRANSITIONS?" *Phys. Rev. D* 35, pp. 1161–1170.

Hogan, C. J. and Dalcanton, J. J. (2000). "New dark matter physics: clues from halo structure". *Phys. Rev. D* 62, p. 063511.

Hook, A. and Huang, J. (2018). "Probing axions with neutron star inspirals and other stellar processes". *JHEP* 06, p. 036.

Hortacsu, M. (2012). "Heun Functions and Some of Their Applications in Physics". Ed. by U. Camci and I. Semiz, pp. 23–39.

Hu, W., Barkana, R., and Gruzinov, A. (2000). "Cold and fuzzy dark matter". *Phys. Rev. Lett.* 85, pp. 1158–1161.

Hui, L. (2021). "Wave Dark Matter". *Ann. Rev. Astron. Astrophys.* 59, pp. 247–289.

Hui, L. et al. (2019). "Black Hole Hair from Scalar Dark Matter". *JCAP* 06, p. 038.

Hui, L. et al. (2023). "Black hole superradiance with dark matter accretion". *Phys. Rev. D* 107.10, p. 104018.

Jacobs, D. M., Starkman, G. D., and Lynn, B. W. (2015). "Macro Dark Matter". *Mon. Not. Roy. Astron. Soc.* 450.4, pp. 3418–3430.

Jenkins, A. C. et al. (2023). "Generalized cold-atom simulators for vacuum decay".

Jenkins, A. C. et al. (2024). “Analog vacuum decay from vacuum initial conditions”. *Phys. Rev. D* 109.2, p. 023506.

Joana, C. and Clesse, S. (2021). “Inhomogeneous preinflation across Hubble scales in full general relativity”. *Phys. Rev. D* 103.8, p. 083501.

Jungman, G., Kamionkowski, M., and Griest, K. (1996). “Supersymmetric dark matter”. *Phys. Rept.* 267, pp. 195–373.

Kadota, K. et al. (2024). “Gravitational wave probes on self-interacting dark matter surrounding an intermediate mass black hole”. *Phys. Rev. D* 109.1, p. 015022.

Karydas, T. K., Kavanagh, B. J., and Bertone, G. (2024). “Sharpening the dark matter signature in gravitational waveforms I: Accretion and eccentricity evolution”.

Kauffmann, G., White, S. D. M., and Guiderdoni, B. (1993). “The formation and evolution of galaxies within merging dark matter haloes.” *Mon. Not. Roy. Astron. Soc.* 264, pp. 201–218.

Kavanagh, B. J., Gaggero, D., and Bertone, G. (2018). “Merger rate of a subdominant population of primordial black holes”. *Phys. Rev. D* 98.2, p. 023536.

Khlopov, M. Y. et al. (1985). “Gravitational instability of scalar fields and formation of primordial black holes”. *Mon. Not. Roy. Astron. Soc.* 215.4, pp. 575–589.

Klypin, A. A. et al. (1999). “Where are the missing Galactic satellites?” *Astrophys. J.* 522, pp. 82–92.

Kobayashi, M. and Maskawa, T. (1973). “CP Violation in the Renormalizable Theory of Weak Interaction”. *Prog. Theor. Phys.* 49, pp. 652–657.

Kocsis, B., Yunes, N., and Loeb, A. (2011). “Observable Signatures of EMRI Black Hole Binaries Embedded in Thin Accretion Disks”. *Phys. Rev. D* 84, p. 024032.

Kolb, E. W. and Long, A. J. (2021). “Completely dark photons from gravitational particle production during the inflationary era”. *JHEP* 03, p. 283.

Koo, H. et al. (2024). “Final parsec problem of black hole mergers and ultralight dark matter”. *Phys. Lett. B* 856, p. 138908.

Krolak, A. and Schutz, B. F. (1987). “Coalescing binaries — Probe of the universe”. *Gen. Rel. Grav.* 19, pp. 1163–1171.

Le Verrier, U. (1859). “Lettre de M. Le Verrier à M. Faye sur la théorie de Mercure et sur le mouvement du périhélie de cette planète”. *Comptes rendus hebdomadaires des séances de l’Académie des sciences* 49, pp. 379–383.

Li, B., Rindler-Daller, T., and Shapiro, P. R. (2014). "Cosmological Constraints on Bose-Einstein-Condensed Scalar Field Dark Matter". *Phys. Rev. D* 89.8, p. 083536.

Linde, A. D. (1992). "Hard art of the universe creation (stochastic approach to tunneling and baby universe formation)". *Nucl. Phys. B* 372, pp. 421–442.

Lovell, M. R. et al. (2012). "The Haloes of Bright Satellite Galaxies in a Warm Dark Matter Universe". *Mon. Not. Roy. Astron. Soc.* 420, pp. 2318–2324.

Macedo, C. F. B. et al. (2013). "Into the lair: gravitational-wave signatures of dark matter". *Astrophys. J.* 774, p. 48.

Manita, Y. et al. (2023). "Spin-2 dark matter from an anisotropic universe in bigravity". *Phys. Rev. D* 107.10, p. 104007.

Markevitch, M. et al. (2004). "Direct constraints on the dark matter self-interaction cross-section from the merging galaxy cluster 1E0657-56". *Astrophys. J.* 606, pp. 819–824.

Marsden, J. et al. (2024). "Symmetry restoration and vacuum decay from accretion around black holes".

Maselli, A. et al. (2022). "Detecting fundamental fields with LISA observations of gravitational waves from extreme mass-ratio inspirals". *Nature Astron.* 6.4, pp. 464–470.

Mateo, M. (1998). "DWARF GALAXIES OF THE LOCAL GROUP". *Annual Review of Astronomy and Astrophysics* 36.Volume 36, 1998, pp. 435–506.

Merritt, D. (2004). "Evolution of the dark matter distribution at the galactic center". *Phys. Rev. Lett.* 92, p. 201304.

Merritt, D., Harfst, S., and Bertone, G. (2007). "Collisionally Regenerated Dark Matter Structures in Galactic Nuclei". *Phys. Rev. D* 75, p. 043517.

Merritt, D. and Milosavljevic, M. (2002). "Dynamics of dark matter cusps". In: *4th International Heidelberg Conference on Dark Matter in Astro and Particle Physics*, pp. 79–89.

Milgrom, M. (1983). "A Modification of the Newtonian dynamics as a possible alternative to the hidden mass hypothesis". *Astrophys. J.* 270, pp. 365–370.

Moore, B. et al. (1999). "Dark matter substructure within galactic halos". *Astrophys. J. Lett.* 524, pp. L19–L22.

Moore, B. (1994). "Evidence against dissipationless dark matter from observations of galaxy haloes". *Nature* 370, p. 629.

Moss, I. G. (1985). “BLACK HOLE BUBBLES”. *Phys. Rev. D* 32, p. 1333.

Mukaida, K. and Yamada, M. (2017). “False Vacuum Decay Catalyzed by Black Holes”. *Phys. Rev. D* 96.10, p. 103514.

Navarro, J. F., Eke, V. R., and Frenk, C. S. (1996). “The cores of dwarf galaxy halos”. *Mon. Not. Roy. Astron. Soc.* 283, pp. L72–L78.

Niemeyer, J. C. (2019). “Small-scale structure of fuzzy and axion-like dark matter”.

Oh, S.-H. et al. (2015). “High-resolution mass models of dwarf galaxies from LITTLE THINGS”. *Astron. J.* 149, p. 180.

Omiya, H., Takahashi, T., and Tanaka, T. (2021). “Renormalization group analysis of superradiant growth of self-interacting axion cloud”. *PTEP* 2021.4, 043E02.

Omiya, H., Takahashi, T., and Tanaka, T. (2022). “Adiabatic evolution of the self-interacting axion field around rotating black holes”. *PTEP* 2022.4, 043E03.

Omiya, H. et al. (2023). “Impact of multiple modes on the evolution of self-interacting axion condensate around rotating black holes”. *JCAP* 06, p. 016.

Omiya, H. et al. (2024). “Deci-Hz gravitational waves from the self-interacting axion cloud around a rotating stellar mass black hole”. *Phys. Rev. D* 110.4, p. 044002.

Oshita, N., Ueda, K., and Yamaguchi, M. (2020). “Vacuum decays around spinning black holes”. *JHEP* 01. [Erratum: JHEP 10, 122 (2020)], p. 015.

Oshita, N., Yamada, M., and Yamaguchi, M. (2019). “Compact objects as the catalysts for vacuum decays”. *Phys. Lett. B* 791, pp. 149–155.

Paczynski, B. (1986). “Gravitational microlensing by the galactic halo”. *Astrophys. J.* 304, pp. 1–5.

Pani, P. et al. (2012a). “Black hole bombs and photon mass bounds”. *Phys. Rev. Lett.* 109, p. 131102.

Pani, P. et al. (2012b). “Perturbations of slowly rotating black holes: massive vector fields in the Kerr metric”. *Phys. Rev. D* 86, p. 104017.

Peccei, R. D. (2008). “The Strong CP problem and axions”. *Lect. Notes Phys.* 741. Ed. by M. Kuster, G. Raffelt, and B. Beltran, pp. 3–17.

Peccei, R. D. and Quinn, H. R. (1977a). “Constraints Imposed by CP Conservation in the Presence of Instantons”. *Phys. Rev. D* 16, pp. 1791–1797.

Peccei, R. D. and Quinn, H. R. (1977b). "CP Conservation in the Presence of Instantons". *Phys. Rev. Lett.* 38, pp. 1440–1443.

Peebles, P. J. E. and Ratra, B. (2003). "The Cosmological Constant and Dark Energy". *Rev. Mod. Phys.* 75. Ed. by J.-P. Hsu and D. Fine, pp. 559–606.

Peter, P. and Uzan, J.-P. (2013). *Primordial Cosmology*. Oxford Graduate Texts. Oxford University Press.

Pontzen, A. and Governato, F. (2012). "How supernova feedback turns dark matter cusps into cores". *Mon. Not. Roy. Astron. Soc.* 421, p. 3464.

Press, W. H. and Schechter, P. (1974). "Formation of Galaxies and Clusters of Galaxies by Self-Similar Gravitational Condensation". *Astrophys. J.* 187, pp. 425–438.

Press, W. H. and Teukolsky, S. A. (1972). "Floating Orbits, Superradiant Scattering and the Black-hole Bomb". *Nature* 238, pp. 211–212.

Pretorius, F. (2005). "Evolution of binary black hole spacetimes". *Phys. Rev. Lett.* 95, p. 121101.

Radia, M. et al. (2022). "Lessons for adaptive mesh refinement in numerical relativity". *Class. Quant. Grav.* 39.13, p. 135006.

Ratra, B. and Peebles, P. J. E. (1988). "Cosmological Consequences of a Rolling Homogeneous Scalar Field". *Phys. Rev. D* 37, p. 3406.

Richardson, L. F. (1911). "The Approximate Arithmetical Solution by Finite Differences of Physical Problems Involving Differential Equations, with an Application to the Stresses in a Masonry Dam". *Philosophical Transactions of the Royal Society of London Series A* 210, pp. 307–357.

Roberts, J. L. et al. (2001). "Controlled Collapse of a Bose-Einstein Condensate". *Phys. Rev. Lett.* 86 (19), pp. 4211–4214.

Rubin, V. C., Ford Jr., W. K., and Thonnard, N. (1980). "Rotational properties of 21 SC galaxies with a large range of luminosities and radii, from NGC 4605 (R=4kpc) to UGC 2885 (R=122kpc)." *Astrophys. J.* 238, pp. 471–487.

Sadeghian, L., Ferrer, F., and Will, C. M. (2013). "Dark matter distributions around massive black holes: A general relativistic analysis". *Phys. Rev. D* 88.6, p. 063522.

Sanchis-Gual, N. et al. (2016). "Quasistationary solutions of scalar fields around accreting black holes". *Phys. Rev. D* 94.4, p. 043004.

Schäfer, T. et al. (2001). "Kaon condensation and Goldstone's theorem". *Phys. Lett. B* 522, pp. 67–75.

Schive, H.-Y., Chiueh, T., and Broadhurst, T. (2014). "Cosmic Structure as the Quantum Interference of a Coherent Dark Wave". *Nature Phys.* 10, pp. 496–499.

Schmidt, M. (1957). "The distribution of mass in M 31". *Bulletin of the Astronomical Institutes of the Netherlands* 14, p. 17.

Seidel, E. and Suen, W.-M. (1994). "Formation of solitonic stars through gravitational cooling". *Phys. Rev. Lett.* 72, pp. 2516–2519.

Shapiro, S. L. and Heggie, D. C. (2022). "Effect of stars on the dark matter spike around a black hole: A tale of two treatments". *Phys. Rev. D* 106.4, p. 043018.

Shapiro, S. L. and Paschalidis, V. (2014). "Self-interacting dark matter cusps around massive black holes". *Phys. Rev. D* 89.2, p. 023506.

Shibata, M. and Nakamura, T. (1995). "Evolution of three-dimensional gravitational waves: Harmonic slicing case". *Phys. Rev. D* 52, pp. 5428–5444.

Shkerin, A. and Sibiryakov, S. (2021). "Black hole induced false vacuum decay from first principles". *JHEP* 11, p. 197.

Siemonsen, N. et al. (2023). "Dark photon superradiance: Electrodynamics and multimessenger signals". *Phys. Rev. D* 107.7, p. 075025.

Sikivie, P. and Yang, Q. (2009). "Bose-Einstein Condensation of Dark Matter Axions". *Phys. Rev. Lett.* 103, p. 111301.

Smarr, L. L. (1975). "The structure of general relativity with a numerical illustration: The collision of two black holes". PhD thesis. University of Texas, Austin.

Spieksma, T. F. M. et al. (2023). "Superradiance: Axionic couplings and plasma effects". *Phys. Rev. D* 108.6, p. 063013.

Taracchini, A. et al. (2014). "Effective-one-body model for black-hole binaries with generic mass ratios and spins". *Phys. Rev. D* 89.6, p. 061502.

Tisserand, P. et al. (2007). "Limits on the Macho Content of the Galactic Halo from the EROS-2 Survey of the Magellanic Clouds". *Astron. Astrophys.* 469, pp. 387–404.

Tomaselli, G. M., Spieksma, T. F. M., and Bertone, G. (2024a). "The legacy of boson clouds on black hole binaries".

Tomaselli, G. M., Spieksma, T. F. M., and Bertone, G. (2024b). "The resonant history of gravitational atoms in black hole binaries".

Traykova, D. et al. (2021). "Dynamical friction from scalar dark matter in the relativistic regime". *Phys. Rev. D* 104.10, p. 103014.

Traykova, D. et al. (2023). "Relativistic drag forces on black holes from scalar dark matter clouds of all sizes". *Phys. Rev. D* 108.12, p. L121502.

Tulin, S. and Yu, H.-B. (2018). "Dark Matter Self-interactions and Small Scale Structure". *Phys. Rept.* 730, pp. 1–57.

Ureña-López, L. A. (2019). "Brief Review on Scalar Field Dark Matter Models". *Front. Astron. Space Sci.* 6, p. 47.

van de Hulst, H. C., Raimond, E., and van Woerden, H. (1957). "Rotation and density distribution of the Andromeda nebula derived from observations of the 21-cm line". *Bulletin of the Astronomical Institutes of the Netherlands* 14, p. 1.

Van Meter, J. R. et al. (2006). "How to move a black hole without excision: Gauge conditions for the numerical evolution of a moving puncture". *Phys. Rev. D* 73, p. 124011.

Vieira, H. S., Bezerra, V. B., and Muniz, C. R. (2014). "Exact solutions of the Klein-Gordon equation in the Kerr-Newman background and Hawking radiation". *Annals Phys.* 350, pp. 14–28.

Visser, M. (2007). "The Kerr spacetime: A Brief introduction". In: *Kerr Fest: Black Holes in Astrophysics, General Relativity and Quantum Gravity*.

Wang, Z. et al. (2022). "Superradiance in massive vector fields with spatially varying mass". *Phys. Rev. D* 105.10, p. 104055.

Weinberg, S. (1978). "A New Light Boson?" *Phys. Rev. Lett.* 40, pp. 223–226.

Wetterich, C. (1988). "Cosmology and the Fate of Dilatation Symmetry". *Nucl. Phys. B* 302, pp. 668–696.

Wilczek, F. (1978). "Problem of Strong P and T Invariance in the Presence of Instantons". *Phys. Rev. Lett.* 40, pp. 279–282.

Witek, H. et al. (2013). "Superradiant instabilities in astrophysical systems". *Phys. Rev. D* 87.4, p. 043513.

Yang, Q. et al. (2018). "An axion-like scalar field environment effect on binary black hole merger". *Res. Astron. Astrophys.* 18.6, p. 065.

Yoshino, H. and Kodama, H. (2012). "Bosenova collapse of axion cloud around a rotating black hole". *Prog. Theor. Phys.* 128, pp. 153–190.

Yoshino, H. and Kodama, H. (2015). "The bosenova and axiverse". *Class. Quant. Grav.* 32.21, p. 214001.

Yunes, N. et al. (2011). "Imprint of Accretion Disk-Induced Migration on Gravitational Waves from Extreme Mass Ratio Inspirals". *Phys. Rev. Lett.* 107, p. 171103.

Zel'Dovich, Y. B. (1971a). "Generation of Waves by a Rotating Body". *Soviet Journal of Experimental and Theoretical Physics Letters* 14, p. 180.

Zel'Dovich, Y. B. (1971b). "Generation of Waves by a Rotating Body". *Soviet Journal of Experimental and Theoretical Physics Letters* 14, p. 180.

Zhang, Y.-P. et al. (2023). "Gravitational recoil from binary black hole mergers in scalar field clouds". *Phys. Rev. D* 107.4, p. 044039.

Zouros, T. J. M. and Eardley, D. M. (1979). "INSTABILITIES OF MASSIVE SCALAR PERTURBATIONS OF A ROTATING BLACK HOLE". *Annals Phys.* 118, pp. 139–155.

Zwick, L. et al. (2022). "Dirty waveforms: multiband harmonic content of gas-embedded gravitational wave sources". *Mon. Not. Roy. Astron. Soc.* 511.4, pp. 6143–6159.

Zwicky, F. (1933). "Die Rotverschiebung von extragalaktischen Nebeln". *Helvetica Physica Acta* 6, pp. 110–127.